Granular Impact Dynamics: Grain Scale to Macroscale

by

Abram H. Clark IV

Department of Physics
Duke University

Date: _____

Approved:

_____
Robert Behringer, Supervisor

_____
Ying Wu

_____
Roxanne Springer

_____
Lawrence Virgin

_____
David Schaeffer

Dissertation submitted in partial fulfillment of the requirements for the degree of
Doctor of Philosophy in the Department of Physics
in the Graduate School of Duke University
2014

Abstract

Granular Impact Dynamics: Grain Scale to Macroscale

by

Abram H. Clark IV

Department of Physics
Duke University

Date: _____

Approved:

_____
Robert Behringer, Supervisor

_____
Ying Wu

_____
Roxanne Springer

_____
Lawrence Virgin

_____
David Schaeffer

An abstract of a dissertation submitted in partial fulfillment of the requirements for the degree of Doctor of Philosophy in the Department of Physics in the Graduate School of Duke University
2014

Abstract

Granular impact, where a foreign object strikes a granular material like sand, is common in nature and industry. Due to experimental difficulties in obtaining sufficiently fast data at the scale of a single grain, a description of this process which connects to physics at the grain-scale is lacking. In this thesis, I will present data from a series of two-dimensional granular impact experiments. By cutting each grain out of a photoelastic material and using a very fast camera, we obtain data on the intruder trajectory, as well as the particle flow and force response of the granular material. Past experiments have shown that the decelerating force on an intruder moving through a granular medium is often well captured by a force law which is dominated by a velocity-squared drag force. Using the intruder trajectories, as well as the flow and force response of the granular material, I will demonstrate that, while these force laws describe the intruder trajectories on slow time scales, the instantaneous force on the intruder is highly fluctuating in space and time. I will particularly focus on the velocity-squared drag force, showing that it arises from random, locally normal collisions with chain-like clusters of particles which send energy and momentum away into the granular material. In this regime, the particles and intruder reach a kind of adiabatic steady state, where the particle motion scales linearly with the intruder speed. However, for impact velocities which are fast compared to the rate of momentum transfer within the granular material, the system response qualitatively changes, behaving like an elastic solid with a shock-like response at impact.

To the lovely and talented Kim

"I placed the sand as a boundary...a perpetual barrier that it cannot pass..."

—Jeremiah 5:22

Contents

List of Tables

List of Figures

List of Abbreviations and Symbols

Symbols

All symbols used are also defined in the text where they first appear.

F	The total force (including gravity) felt by the intruder as it moves through the granular medium.
F_g	The force exerted by the granular material on the intruder, not including gravity.
z	The depth of the intruder below the point where it initially contacts the unperturbed granular surface.
v	The intruder velocity, which is typically assumed to be purely vertical, $v = \dot{z}$, where the dot denotes a time derivative.
a	The intruder acceleration, also typically assumed to be purely vertical, $a = \ddot{z}$.
m	Mass of the intruder.
K	The kinetic energy of the intruder, $K = \frac{1}{2}m\dot{z}^2$.
v_0	Initial impact velocity of the intruder at $z = 0$.
K_0	Initial kinetic energy of the intruder, $K = \frac{1}{2}mv_0^2$.
z_{stop}	The final penetration depth of the intruder.
D	The diameter of a circular intruder
R	The radius of a circular intruder
a	The semi-major axis of the elliptical nose of an ogive intruder.
b	The semi-minor axis of the elliptical nose of an ogive intruder.

c	Typical speed at which force information travels in a particular granular material.
g	Gravitational acceleration, $g \approx 9.8$.
$f(z)$	The static (i.e., independent of the intruder speed) force term in a particular force law which approximates the intruder deceleration as it moves through the granular medium.
$h(z)$	The depth-dependent drag coefficient in the force-law model; it appears in the force law as $h(z)\dot{z}^2$.
G^2	The discrete gradient-squared of an photoelastic image, which is often used as a measure of the local pressure
η	Multiplicative term which captures the fluctuations in the granular force on the intruder.
h_0	The value of the drag coefficient $h(z)$ over a range of depths where it is constant, under conditions that such a range exists.
$C(x)$	Function characterizing the shape of the intruder nose.
m_c	Mass of a cluster of grains with which the intruder collides.
W	Total width of the intruder; $W = D = 2R$ for circular intruders, $W = 2b$ for ogive intruders.
d	Diameter of the disks which comprise the granular assembly.
$I[C(x)]$	The shape-factor derived from the collisional model which characterizes the dependence of the drag coefficient on the intruder shape.
s	The aspect ratio of the triangular nose on certain intruders, which also gives the slope everywhere except at the intruder tip.
τ	The torque on an intruder moving through a granular material.
$J[C(x,\theta)]$	The shape-factor derived from the collisional model which characterizes the dependence of the torque on the intruder shape.
λ_+	The growth rate of the off-axis rotation of an intruder, such that the angular orientation is given by $\theta \sim e^{\lambda_+ z}$.
$\mathbf{u}$	The coarse-grained velocity flow field of the granular material.

$\mathbf{A}$	The steady-state flow field which characterizes the flow of the granular material near the intruder during the bulk of the trajectory.

Abbreviations

All abbreviations are also defined as they first appear in the text.

ODE	Ordinary differential equation.
PIV	Particle image velocimetry.
1D, 2D, 3D	One-, two-, and three-dimensional.

Acknowledgements

I would like thank my adviser, Bob Behringer. Most graduate students are not lucky enough to have a boss who is extremely kind, an excellent scientist, and an effective intellectual mentor. Bob is all three of these, and he is even patient with me if he catches me in the morning before I've had coffee.

I would also like to thank the folks at Duke that have helped me in various ways with my research. Joshua Dijksman, who has talked science with me over coffee too many times to count, as well as answered hundreds of random questions about what part I should buy or where something is in the lab. Thanks to Alec Petersen for all his hard work in helping me record and process an unbelievable amount of data. Thanks to the other graduate students, postdocs, and visiting students in Bob's group for feedback and advice through the years: Jie Ren, Junyao Tang, Somayeh Farhadi, Jie Zhang, Dong Wang, Nicolas Brodu, Jonathan Bares, Hu Zheng, and Thomas van Dop.

Thanks to the other scientists who have studied granular impact with me: Lou Kondic at NJIT, Wolfgang Losert and Kerstin Nordstrom at Maryland, and Corey O'Hern at Yale. Also, I would like to thank Dan Goldman at Georgia Tech, Paul Umbanhowar at Northwestern, and Doug Durian at Penn for helpful insights and comments on the physics of granular impact. Thanks to the rest of my committee: Roxanne Springer, Ying Wu, Richard Palmer, Lawrie Virgin, and Dave Schaeffer. Thanks to the folks at DTRA for funding my research

Thanks to my daughter Charlotte for infectious happiness. Thanks to my parents for the freedom and encouragement they have given since I was very young.

Most importantly, I'd like to thank my wife, Kim, for making my life during graduate school possible by consistently preserving my sanity, by cushioning the rougher parts of my personality by baking for my friends, by generally being a voice of reason in my life, and by constantly amazing people we know by how well she takes care of me. As a friend of ours said, I have an "old-school wife," which I think means talented, hard-working, and selfless.

1

Introduction

Granular materials are everywhere. They are defined as collections of dry, macroscopic particles which are too large to be affected by thermal energy. Thus, they only interact through contact forces which are generally frictional and repulsive, but can also include a cohesive term in certain cases. They are processed and manipulated in all corners of industry, from coffee beans to pharmaceutical powders to grains in a silo. They are ubiquitous in nature, studied carefully in fields such as soil mechanics and earthquake science.

From a physicist's perspective, granular materials present a fascinating set of problems to study. For instance, granular materials can behave like each of the three classical phases of matter (Jaeger et al., 1996), a fact which is known by every child who has played on the beach. We walk on the beach, and sand supports our weight like a solid. We play in the sand, and it flows like a liquid, taking the shape of its container. A strong ocean breeze can excite sand into a gas-like state, which is dilute and energetic. What are the constitutive laws for each of these phases, and can they be understood in terms of a description at the scale of a single grain? What is the nature of the transitions between the different phases, and what are the relevant

order parameters? The answers to these questions are still subjects of debate, and fundamental physical descriptions for the simplest kinds of granular flows are still lacking in many cases.

1.1 Introduction to Granular Impact

One important example of such a flow, and the main subject of this thesis, is the process of granular impact, where an intruder strikes a granular material, generally at a high speed. The intruder loses its kinetic energy to the granular material and comes to a stop. This process is extremely common in nature, given the granular nature of the soil and sand which covers much of the Earth. The magnitude of a granular impact can be very gentle, such as acorns falling into loose soil, or extremely violent, such as a meteor impacting a planetary surface. Additionally, there are many industrial processes or ballistics applications where understanding granular impact would be useful. A description should ideally explain how the intruder's energy is transferred to the granular material and then dissipated, all in terms of physical interactions at the grain scale. This presents a significant challenge since, for example, the acorn and the meteor are clearly in separate regimes which are governed by different physical processes.

For classical materials, response to an impact is fundamental in characterization of solid, liquid, and gas. For example, solids deform and store energy elastically. The decelerating force on the intruder is captured well by elasticity theory, and can often simply be approximated by an ideal Hookean spring. Liquids splash and flow around an intruding object. The decelerating force in this case is captured by fluid mechanics, and is typically well represented as a combination of a buoyancy force, viscous drag, and inertial drag. Buoyancy force is depth-dependent, the viscous drag force typically depends linearly on the intruder velocity, while inertial drag depends quadratically on velocity, and the relative strength of each term depends on the

intruder speed as well as microscopic parameters of the system (e.g., viscosity). For solids and fluids, the mathematical form used to represent these forces can sometimes be derived from continuum mechanics using a constitutive law, which essentially relates stresses in the material to the local flow or deformation of the material. However, for a highly dynamic process, such as projectile impact into water (Truscott et al., 2014), such a derivation may be too difficult to accomplish in closed form and is only possible numerically. However, elasticity and fluid mechanics are well developed fields, so constitutive laws are well understood and are often successful in simple cases, such as an intruder moving through a fluid at a constant speed.

For granular materials, the existence of a constitutive-law description varies depending on the state of granular matter being considered. In the very dense limit, granular materials behave somewhat like classical elastic solids. In this state, the material is said to be strongly jammed, and all degrees of freedom are constrained by contact forces between particles. As the density at which grains are packed is decreased, the granular material becomes less stable, and under sufficient applied forces, the grains can rearrange and form a fluid-like flow. The transition between liquid-like and solid-like behavior is called the jamming transition, and it has been the topic of significant study in the granular physics community, often described in the context of a critical phase transition using frictionless particles (Liu and Nagel, 2010; van Hecke, 2010; O'Hern et al., 2003), or after adding friction (Bi et al., 2011), where the picture becomes more complex. As the density is decreased further, particles no longer have persistent interactions with neighbors, and binary collisions between particle pairs become dominant. In the dilute limit, we recover the classical ideal gas, but with the important distinction that energy is lost in each collision, which gives rise to a clustering instability (Goldhirsch and Zanetti, 1993). The granular liquid is perhaps the most challenging to characterize, particularly in the phase close to the jamming transition, where fluctuations become very large and can dominate

the behavior of the system.

For granular impact, the relevant phases are dense granular liquid phase and the solid phase, both in the initial state of the system and during the impact process. While the development of constitutive laws for this phase have seen great advances in the last decade (da Cruz et al., 2005; Jop et al., 2006; Kamrin and Koval, 2012), they are still in their infancy, and typically only tested for well developed granular flows which are static in time. In contrast, granular impact represents an extremely complex flow which is certainly not static in time. Even if an appropriate constitutive law were known, finding the force on the intruder by integrating a local flow rule for the entire granular system would be a considerable challenge, even with numerical methods.

Despite the lack of a comprehensive particle-scale description, dynamics of the intruder deceleration can often be described by a macroscopic force law which relates the force exerted on the intruder by the granular material directly to the depth and velocity of the intruder. This is similar in spirit to the descriptions discussed previously for classical solids and fluids, but without the microscopic derivation which is often possible in these cases. This approach dates back to the time of Euler and Poncelet, and it is mostly heuristic. That is, these models are used primarily because they yield differential equations which successfully describe the intruder trajectory, but they have minimal grounding in a grain-scale physical picture.

Connecting these force laws to a grain-scale description and understanding the conditions under which they are valid are the primary goals of the work presented in this thesis. I will use these macroscopic force laws as my starting point, as opposed to grain-scale constitutive laws. However, this approach will actually yield significant insight about the stresses on the intruder boundary, such as their spatial structure and dependence on intruder velocity, which is the essential spirit of a constitutive law.

The remainder of this chapter is structured as follows. First, I will discuss coarse graining, which provides the theoretical justification for using continuum mechanics, as well as corresponding constitutive laws, in treating granular materials. I will summarize the recent advances in the constitutive laws for dense granular flows and point out their limitations, particularly in application to granular impact. Next, I will give an overview of the scientific work on granular impact, particularly focusing on the macroscopic force law approach discussed previously. Finally, I will introduce the work which I will present in this thesis, focusing on how it fits into the existing body of work on granular impact.

1.2 Coarse Graining, Continuum Mechanics, and Constitutive Laws

While classical liquids are composed of discrete molecules, they are typically treated as *continua*. The discreteness is smoothed out, and the liquid is treated using the framework of continuum mechanics. This process is made possible by the large separation of scales (typically, many orders of magnitude) between the size of a particle and the typical scale of gradients in the system. For granular systems in all three phases, this same approach can be used in principle, although the necessary separation of spatial scales is not as obvious. Thus, a smoothing or *coarse-graining* approach must be chosen with some care.

The backbone of continuum mechanics lies in two differential equations, which represent conservation of mass and momentum.

$$\frac{\partial \rho}{\partial t} = -\nabla \cdot \mathbf{p} \tag{1.1}$$

$$\frac{d\mathbf{p}}{dt} = \nabla \cdot \boldsymbol{\sigma} \tag{1.2}$$

Here, ρ is the mass density, $\mathbf{p}$ is the momentum density, and $\boldsymbol{\sigma}$ is the stress tensor. The second equation is simply a local differential form of Newton's second law of

motion, $\mathbf{F} = \frac{d\mathbf{p}}{dt}$. If the stress tensor can be written in terms of the mass and momentum density fields, then the equations are closed, and can be solved in principle for arbitrary geometries, given some boundary conditions. An equation which relates the local stresses to mass and momentum density fields is called a *constitutive law*, and often comes in the form as a relation between stresses and strains or strain rates. There is no *a priori* reason that such a relation should exist, but very often, a suitable constitutive law can be found which allows solution of the equations, as well as significant insight into the microscopic processes which control the local flow. One well known example is the constitutive law for a Newtonian fluid with a viscosity μ. In this case, the elements of the stress tensor, σ_{ij} can be written:

$$\sigma_{ij} = -\left(p\delta_{ij} + \frac{2}{3}\mu\nabla\cdot\mathbf{v}\right) + \mu\left(\frac{\partial v_i}{\partial x_j} + \frac{\partial v_j}{\partial x_i}\right), \tag{1.3}$$

where p is the isotropic pressure, v_i are components of the velocity $\mathbf{v}$, and x_i are spatial coordinates. For solid or elastic-like behavior, the stress tensor is typically written as $\sigma_{ij} = C_{ijkl}\epsilon_{kl}$, where $\boldsymbol{\epsilon}$ is the microscopic strain tensor and $\mathbf{C}$ is the stiffness tensor, the form of which varies depending on the material.

One particularly elegant coarse-graining formalism was developed by Goldenberg and Goldhirsch (Goldhirsch and Goldenberg, 2002; Goldhirsch, 2010). In this framework, a coarse-grained field (e.g., density, momentum, etc.) is defined by replacing the Dirac delta functions at particle centers by a smooth, normalized function which is centered at the particle center. For example, if the microscopic density field is defined as

$$\rho^{\mathrm{mic}}(\mathbf{r}) \equiv \sum_i m_i\delta[\mathbf{r} - \mathbf{r}_i(t)], \tag{1.4}$$

where $\mathbf{r}$ are spatial coordinates, m_i and $\mathbf{r}_i$ represent the mass and position of the i^{th} particle, and δ is the Dirac delta function. The coarse-grained density field is defined

as

$$\rho(\mathbf{r}) = \sum_i m_i \phi[\mathbf{r} - \mathbf{r}_i(t)], \tag{1.5}$$

where δ has been replaced by ϕ, which is a unit-normalized coarse-graining function. Often, ϕ is chosen as a normalized Gaussian, which in two-dimensions would yield $\phi(\mathbf{r}) = \frac{1}{\pi w^2} e^{-(|\mathbf{r}|/w)^2}$. Similarly, the coarse-grained momentum field is defined as

$$\mathbf{p}(\mathbf{r}) \equiv \sum_i m_i \mathbf{v}_i \phi[\mathbf{r} - \mathbf{r}_i(t)]. \tag{1.6}$$

This framework has two important features. First, if mass and momentum conservation are assumed, Eqs. (1.1) and (1.2) can be derived directly from these definitions, including a definition of the coarse-grained stress tensor explicitly in terms of instantaneous particle positions, particle velocities, and interparticle forces. Second, the coarse-graining function can be tuned by changing the characteristic width, w, in order to find an appropriate separation of scales. This can be done in most granular systems, even those with moderate spatial variation. These two points provide theoretical justification for treating dense granular flows as continua using an appropriate coarse-graining procedure. However, the extent to which finite particle size affects the applicability of a continuum description must be evaluated for each system.

Any continuous stress tensor for a granular material necessarily represents a coarse-grained representation of actual contact forces (Cauchy stress) and particle velocity fluctuations (Reynolds stress). If this stress tensor is, at least on average, well described by some function of the local mass and momentum density fields, then a constitutive relation is obtained, and the equations of motion can be solved. The most successful attempt at this to date for dense granular flows is so-called $\mu(I)$ rheologies developed for shear flows (da Cruz et al., 2005; Jop et al., 2006; Kamrin and Koval, 2012), which heuristically relate the local shear stress to the local confining pressure and the local shear rate through a dimensionless number, I, also called an

inertial number. The inertial number can be thought of as a ratio of two time scales: a particle rearrangement time, $t_r = \sqrt{m/P}$, and a strain-rate time, $t_s = 1/\dot{\gamma}$ (here, P is pressure, m is the particle mass, and $\dot{\gamma}$ is the strain rate). It can be shown that the friction coefficient μ, which is the ratio of tangential stresses to normal stresses, is only a function of $I = t_r/t_s$. This constitutive law was developed for simple shear flows in two dimensions, but has been successfully extended to other geometries and three dimensions as well by generalizing the strain rate, $\dot{\gamma}$, to a local strain-rate tensor. These constitutive laws have been quite successful in describing well developed (i.e., after initial transients have died out), dense granular flows.

There is also a particular case in which the inertial number description fails. In continuously sheared systems, when the shear rate begins to approach *the elastic time scale* of the granular material, the shear stress required to maintain the shear flow jumps drastically (Campbell, 2002). In this study, Campbell performed simulations on simple shear flows, using particles which interacted via linear springs. As the shear rate increased, the shear stress required to maintain a constant velocity climbed dramatically. Again, this effect is for *steady* flows, which are held at a constant shear rate.

1.3 Granular Impact: A Dynamic Granular Flow

The $\mu(I)$ constitutive law, as well as the elastic limit failure just described, have only been tested on well developed shear flows. On the other hand, granular impact is an entirely transient process. When the intruder strikes, the intruder momentum and energy are typically transferred to the granular material and dissipated. The intruder has some initial velocity, v_0, and at the end of the process, the intruder has come to rest at some final depth, z_{stop}. Thus, there is, in general, no well developed regime, where the process is stationary. The exception is in the case of a heavy intruder traveling downward through a super-light granular medium in a long

channel, where there exists a terminal velocity (Pacheco-Vázquez et al., 2011) and thus a steady state. However, the fundamentally transient nature of granular impact makes application of any continuum rheology difficult, even in principle, and it is unclear if and how granular impact might relate.

Historically (Walsh et al., 2003; Newhall and Durian, 2003; de Bruyn and Walsh, 2004), the simplest approach to characterizing granular impact consists of a kind of zeroth-order scaling approach, where the final penetration depth or size of the resulting crater is recorded as a function of impact parameters, such as initial intruder speed, particle or intruder properties, and other system parameters (such as interstitial fluid, strength of gravity, etc.). The entire process of impact is essentially averaged over, since only the initial and final states of the system are measured. Thus, this approach is inherently limited, although a suitable collapse for this data can provide insights into the microscopic physics which controls the process.

The macroscopic force law approach (Allen et al., 1957; Tsimring and Volfson, 2005; Katsuragi and Durian, 2007; Goldman and Umbanhowar, 2008; Umbanhowar and Goldman, 2010), as discussed previously, provides significantly more opportunity for microscopic insight into the dynamics of granular impact, assuming a force law can be found which captures the dynamics. For an intruder of mass m which strikes a flat granular material normally from above, assuming no horizontal motion throughout the impact process, the dynamics are given by

$$m\ddot{z} = mg - F_d, \tag{1.7}$$

where z is the depth below initial contact with the surface, mg is the gravitational force, and F_d is the upward force exerted on the intruder by the granular material. If F_d can be written in terms of the intruder depth and velocity, z and $\dot{z}$, this differential equation can be integrated to obtain a solution for the trajectory, $z(t)$. Thus, the final depth is predicted as the depth at which the velocity goes to zero. In this way,

the force-law approach, if successful, should explain whatever scaling is found for the final penetration depth. Additionally, if a suitable form for the granular force can be found in terms of z and $\dot{z}$, then this provides additional insight into the grain-scale interactions which govern this process.

The functional form for $F_d(z, \dot{z})$ is typically chosen as the simplest form which fits the trajectories observed for a particular set of experiments. While various forms have been used for different experiments, they almost always contain a velocity-squared ($\dot{z}^2$) drag term, which dominates the stopping process for moderate to fast impacts. Additionally, one would expect that as the intruder penetrates deeper into the granular bed, there would be some effect from increased pressure at larger depths, suggesting a z-dependence of some type. Many studies have successfully used a form for the granular force on the intruder with two terms, which can be generally written as $F_d = f(z) + h(z)\dot{z}^2$. Inserting this into equation (1.7) yields:

$$m\ddot{z} = mg - f(z) - h(z)\dot{z}^2. \tag{1.8}$$

Here, $f(z)$ is a static-like term which depends only on depth, and $h(z)\dot{z}^2$ is an inertial or collisional drag force. The functional form for $f(z)$ varies, but is often approximated as either a constant, $f(z) = f_0$ (Allen et al., 1957; Tsimring and Volfson, 2005), or linearly increasing in depth, $f(z) = kz$ (Katsuragi and Durian, 2007) or $f(z) = f_0 + kz$ (Goldman and Umbanhowar, 2008). It is often assumed to be the same force as in the slow-drag regime (Albert et al., 2001; Geng and Behringer, 2005; Goldsmith et al., 2013). The inertial drag term, $h(z)\dot{z}^2$, is used in virtually every study on granular impact which uses a force law in the class of equation (1.7). Often, the drag coefficient, $h(z)$, is taken to be a constant, $h(z) = b$. The simplest form of equation (1.8), where $f(z)$ and $h(z)$ are both assumed to be constant, is called the Poncelet equation. Under these assumptions, the final penetration depth,

z_{stop}, can be simply calculated (Allen et al., 1957; Tsimring and Volfson, 2005).

$$z_{stop} = \frac{b}{2m} \log\left(1 + \frac{bv_0^2}{f_0 - mg}\right) \tag{1.9}$$

The assumption that $f(z)$ and $h(z)$ are constant is particularly useful in horizontal impacts (Allen et al., 1957), where there is no depth dependence (in this case, the gravitational force should also be removed).

While it is generally agreed upon that a velocity-squared drag force is fundamentally inertial (that is, it comes from colliding with or accelerating some mass of fluid or particles in front of it), the grain-scale nature of this force is poorly understood. Since we know that the granular material during an impact process is primarily in the dense liquid phase, where the material is near jamming and fluctuations can become very large, one might expect to find a rich grain-scale picture with the right experiment. Two recent experiments in particular have suggested that there are important grain scale effects which must be understood for a full description. Takehara *et al.* performed an experiment with horizontal, constant-velocity drag through a granular medium, which allowed isolation of the velocity-squared drag force (Takehara et al., 2010). Through momentum-transfer considerations and observation of the motion of grains, they concluded that the intruder was colliding with clusters larger than a single particle and that "the formation of the dynamical force chains plays a crucial role." Umbanhowar and Goldman performed a study of granular impact into beds of sand with varying packing fraction (Umbanhowar and Goldman, 2010). They observed that the magnitude and functional form of the functions $f(z)$ and $h(z)$ in equation (1.8) showed a nontrivial dependence on the initial packing fraction.

In addition to the underlying grain-scale physics, it is also useful to understand under what conditions these models work and when they break down. For example, most prior experimental work on granular impact are in the subsonic regime, where

the speed of the intruder is very small compared to the typical speed at which stress propagates through the granular material. A typical acoustic speed for ordinary sand or glass beads is between 100 and 300 m/s, which is difficult to reach in a laboratory setting. However, some studies which have probed this regime (Allen et al., 1957) have found that the granular force increases substantially when the intruder speed approaches a typical acoustic speed in the granular medium.

1.4 This Work

The conclusion of these studies and others is that grain-scale phenomena exist that are an essential piece to understanding the forces during granular impact. However, primarily due to experimental and technological limitations, they lack data for the granular material at sufficiently small space and time scales. The primary focus of this work is to try to improve the understanding of the grain-scale origins of the forces and dynamics during granular impact, particularly focusing on the microscopic origins of macroscopic force laws, as in Eq. (1.8). We have constructed an apparatus which combines recent advances in camera technology with a well understood technique called photoelasticity. This experimental setup allows us to perform two-dimensional impact experiments, where we observe and quantify particle positions, velocities, and forces, in addition to the dynamics of the intruder. A high-speed camera allows us to capture images which yield this data at the spatial scale of a single grain, and at the time scale of particle-particle momentum transfer. In the remainder of this thesis, I will present the results from these experiments, which give substantial insight into the microscopic nature of granular impact.

2

Experimental Methods

For a complete description of granular impact, it is desirable to have data on the intruder trajectory as well as the particle flow fields and stresses. However, for obvious reasons, it is difficult to obtain such data experimentally. Accelerometers and force sensors can be placed on the intruder, but these often have a maximum time resolution of about 1 kHz (Goldman and Umbanhowar, 2008; Umbanhowar and Goldman, 2010), and can be difficult to configure. Some authors have obtained the intruder trajectory by attaching a long tail to the intruder and tracking it as it is dropped into a bed of sand. However, the particle movements and force response of the granular material have essentially never been captured at speeds comparable to the acoustic speeds in the system, except in simulations.

In light of this issue, we designed and built a two-dimensional impact experiment, with a granular assembly made up of small photoelastic disks. The two-dimensional nature of the impacts allow us to visualize and quantify the entire system—the intruder as well as all the grains—using high-speed video. We can obtain the trajectory of the intruder directly from video by measuring its position at each frame. The use of photoelastic disks allows two configurations for measurement: using crossed po-

larizers, which allows us to see the forces on each grain at each frame, and using unpolarized light, where the motion of the grains can be tracked. In this way, we have access to the intruder trajectory, as well as the particle motion and stresses in the granular material. This experiment is similar to a previous study from our lab (Daniels et al., 2004), but with a much faster camera. As in any two-dimensional experiment, the simplification is useful in data collection and processing, but it is unclear if there are relevant differences from three-dimensional systems which we are attempting to model. We return to this point in later chapters.

The material discussed in this chapter is primarily the basics of the techniques used to gather and process the data from the high-speed videos. Most of the techniques used in this work are not novel, and citations are provided in lieu of detailed descriptions of well established techniques. Additionally, many details of how the data is processed, especially those connected to the underlying physics, are presented and discussed as they are used throughout the text.

2.1 Experimental Setup

2.1.1 Experimental Apparatus

The primary experimental apparatus consists of two thick, clear acrylic sheets (0.91 m $\times$ 1.22 m $\times$ 1.25 cm) which are separated by a thin gap (about 3.3 mm) and oriented vertically. The gap can then be filled with disks which are approximately 3 mm thick, with diameters greater than 4.3 mm (further details are discussed later in the chapter). This ensures that all disks remain in a single layer, edge to edge with their neighbors, forming a two-dimensional granular assembly. The gap between the acrylic sheets is closed at the bottom and the sides to support the grains, but the top is left open so intruders can be dropped in from above. Intruders are machined from bronze sheet (bulk density of 8.91 g/cm^3, thickness of 2.3 mm) into various shapes and sizes. They are dropped into the granular assembly through a long shaft

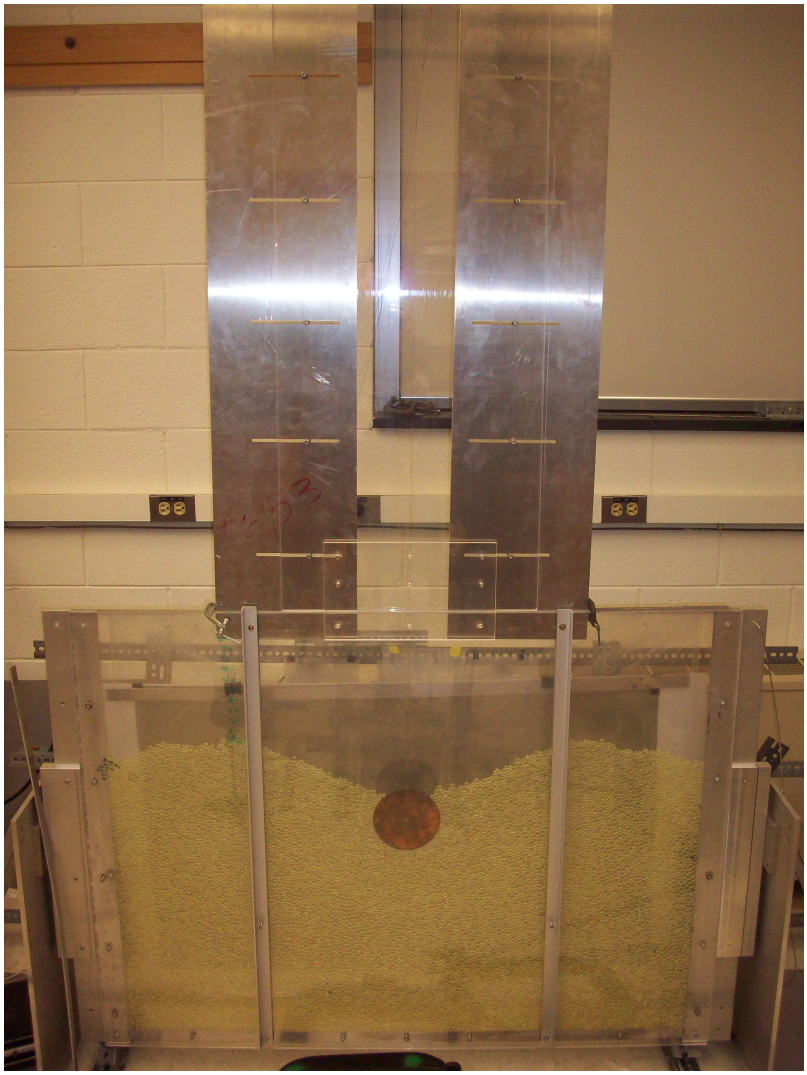

FIGURE 2.1: Picture of the experimental apparatus used for experiments discussed in this thesis.

which connects to the thin gap containing the particles, from initial heights H above the unperturbed granular bed, with $H \leq 2.2m$, producing initial impact speeds $v_0 \simeq (2gH)^{1/2} \leq 6.6$ m/s.

The results of each impact are recorded with a Photron FASTCAM SA5, which has a maximum throughput of 7000 megapixels per second. That is, at the full frame resolution of 1024×1024 pixels (or one megapixel), the maximum frame rate is 7000 frames per second (fps), and higher frame rates (up to 775,000 fps) can be

achieved but only with reduced pixel resolution. For unpolarized videos, the camera is typically set to 1024×1024 pixels at 7000 fps. For polarized videos, where the photoelastic force response is captured, the camera is typically set between 10,000 and 50,000 fps with a pixel resolution of approximately 400×300 pixels. The pixel resolution and the aspect ratio of the videos varies for each experiment depending on the frame rate chosen and the desired field of view. These extremely fast frame rates with relatively large pixel resolution are what makes the bulk of the analysis presented in this thesis possible.

2.1.2 Photoelasticity

Photoelasticity is stress-induced birefringence which is exhibited by many transparent materials. Essentially the refractive indices at any point in a photoelastic material depend on the local stress tensor, specifically on the local eigenvalues of the stress tensor. This means that stresses change the speed of light along the principle directions of the stress tensor, and any anisotropy in the stress tensor will yield a different index of refraction for light which is polarized along the different principle stress directions.

Circularly polarized light can be decomposed into two orthogonal, linearly polarized waves with a spatial phase shift of one quarter wavelength. If circularly polarized light passes through a photoelastic material with some local stress anisotropy, the components of the light wave which are polarized along the principle directions will travel at different speeds, thus generally turning circular into elliptical polarization. After passing through the photoelastic material, if this light passes through another circular polarizer with polarity opposite to the original polarization, then any light which is unperturbed by the photoelastic effect will not pass through. Only light which has been subjected to the phase shift in the photoelastic material will pass.

If we cut our particles out of photoelastic material, this allows us to directly see

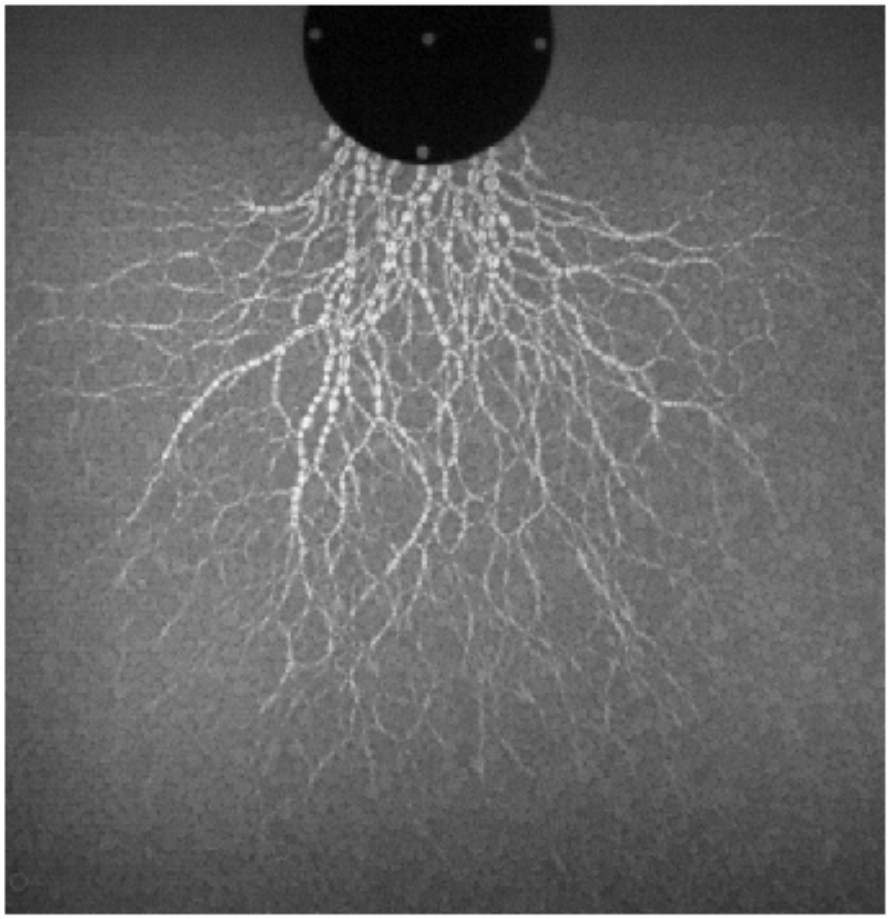

FIGURE 2.2: A typical photoelastic image from an impact using intermediate stiffness particles (Shore 80A). Bright particles are experiencing force.

the particles which are under stress, as they will appear bright. The experiment is illuminated from behind by tungsten halogen bulbs, and a large circular polarizer, consisting of a linear polarizer and a quarter-wave plate, is placed between the light source and the granular assembly. A crossed circular polarizer is placed in front of the high speed camera, which only allows light to pass which has be perturbed by the photoelastic effect.

To make quantitative measures for the local granular force, some kind of calibration scheme must be used, where the photoelastic response is measured in response to a known pressure. Typically, as pressure is increased, there is a minimum pressure before the particles appear bright enough to see, followed by a quasi-linear response region where the brightness increases proportionately with the pressure, followed by saturation. The brightness saturation is fundamentally tied to the photoelastic effect. Recall that the particles appear bright because the two orthogonal components of the circularly polarized wave were separated by some phase, $\Delta\phi$, which depends on the local stress at a particular point inside the particle, $\Delta\phi \sim (\sigma_2 - \sigma_1)$, where σ_1 and σ_2 are the principle eigenvalues of the local stress. If this phase difference is equal to half of a wavelength, then the original polarization (e.g., right-handed circular) is converted to that of the crossed polarizer in front of the camera (e.g., left-handed circular), which corresponds to the maximum brightness. If this phase difference is equal to a full wavelength, then the polarization returns to its original state, which corresponds to a minimum brightness. So, the photoelastic response, I, is periodic in the local applied stress, $I \sim \sin^2 \frac{\Delta\phi}{2}$.

The experiments presented here use three different photoelastic materials with varying stiffness. The stiffest material is PSM-1, manufactured by Vishay Precision Group. This material has an elastic modulus of about 2.5 GPa, which is similar to glass or sand. This material was cut into approximately 25,000 disks with diameter 6 mm and 4.3 mm, with similar numbers of each size. Additionally, two other materials were used, both sheets of polyurethane manufactured by Precision Urethane. Their stiffness is measured on the Shore Durometer scale, type A, with a hardness rating of 60 and 80, which approximately corresponds to an elastic modulus of 1 MPa and 10 MPa, respectively (Qi et al., 2003). Each of these materials was cut into approximately 12,000 disks with diameter 9 mm and 6 mm, with similar numbers of each size. For the softer particles, the 4.3-mm particles were replaced by

Table 2.1: Table showing the properties of the particles used to build the 2D granular assembly. Force law parameters are for the larger size particle for each type of material.

Material	Diameters	k	α
Shore 60A	6 and 9 mm	1×10^5	1.45
Shore 80A	6 and 9 mm	8×10^6	1.7
Shore 60A	4.3 and 6 mm	2×10^9	1.85

9-mm particles due to trouble with particles flipping sideways during experiments, which would have been exacerbated by decreasing the particle stiffness. For particles made of each material, force-compression curves were obtained using a micro-strain analyzer. The curves for the larger particles for each material are shown in Fig. 2.3.

2.2 Data Processing

2.2.1 Obtaining Intruder Trajectories

In practice, the circular polarization is not perfect, and even "dark" regions in the granular material (either unstressed, or in a void between particles) allow a small amount of light to pass. The intruder itself, however, is opaque and allows no light to pass. This allows clear separation of three distinct light levels in each image: bright particles, dark particles or voids, and the intruder. By using distinguishing features of the intruder, the intruder position can be found at each frame. For circular intruders, a circular Hough transform (Ballard, 1981) is most effective. For intruders of other shapes, there are typically holes machined in the intruder which appear brighter and can easily be tracked, which yields the position of the center of mass and angular orientation of the intruder at each frame. The typical error for the center of mass location of the intruder varies somewhat depending on the routine used, but it is always smaller than a single pixel (for reference, a typical image has about 10 pixels per particle). All this is done using simple image processing in MATLAB.

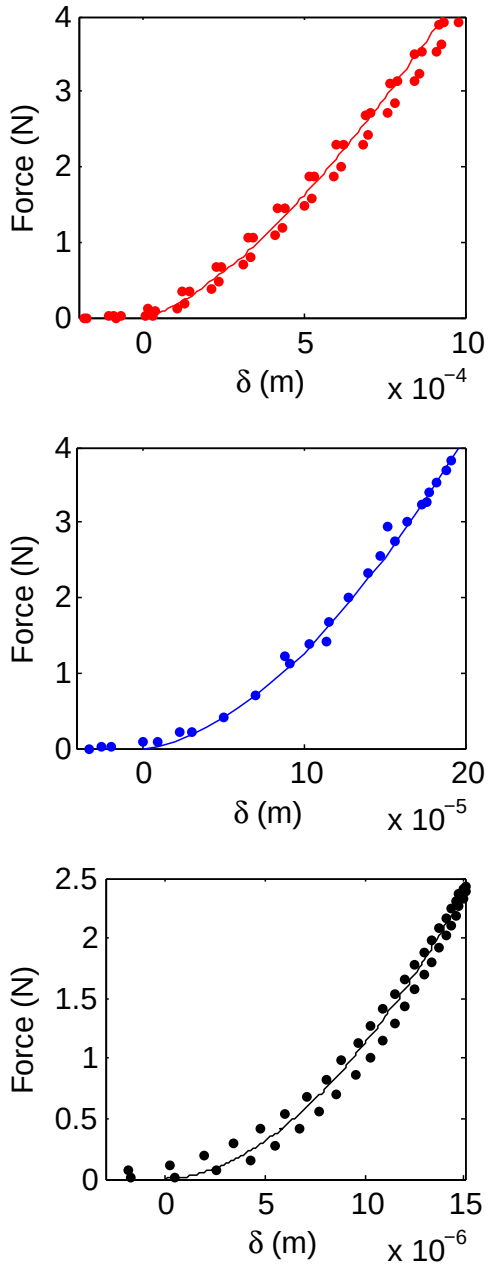

FIGURE 2.3: Panels show force, $\mathcal{F}$, versus compression, δ, measured experimentally in a micro-strain analyzer by compressing the particle between two plates, with a curve fit of the form $\mathcal{F} = k\delta^{\alpha}$. The top panel is a Shore 60A 9-mm disk ($k = 1 \times 10^5$, $\alpha = 1.45$), the middle panel is a Shore 80A 9-mm disk ($k = 8 \times 10^6$, $\alpha = 1.7$), and the bottom panel is a PSM-1 6-mm disk ($k = 2 \times 10^9$, $\alpha = 1.85$). The force-compression curves show slight hysteresis as the particles are compressed and uncompressed.

Once the intruder position is known for each frame, numerical differentiation is used to find the intruder's velocity and acceleration. The simplest way to do this is simple differencing, where the velocity at each frame is the difference in position between the current frame and the previous, divided by the sampling time. However, this method amplifies the experimental noise in the intruder's position, so a low-pass filter of some type must be used in combination with numerical differentiation.

To accomplish this, derivatives are found by linear fits using N frames, which corresponds to a time interval, Δt, equal to N divided by the frame rate. Thus, velocity at a certain frame is the slope of the best linear fit of N data points of intruder position versus time, centered at the frame of interest. Velocity data is processed similarly to obtain acceleration data, reducing the time resolution of the velocity and acceleration by factors of N and $2N$, respectively. The value of N should be chosen at the minimum value which sufficiently reduces the experimental error. A value of N which is unnecessarily large may eliminate fluctuations in the velocity or acceleration which are physical. Choice of N and its relationship to physical fluctuations will be discussed in later chapters.

2.2.2 Obtaining Granular Force Measurements

As previously discussed, the brightness patterns in a photoelastic image are directly related to the stress state of the photoelastic material. With sufficient image resolution, it is even possible to deduce vector contact forces between particles (Majmudar, 2005). However, due to the resolution limitations of high-speed video, the images in these experiments are too coarse for this technique, and the image brightness or intensity must be used in some way as a coarser measure of the local pressure.

A reasonable numerical measure of the local granular force can only be obtained if the photoelastic response is in the linear response regime (i.e., the force is strong enough such that the particles appear bright, but not so strong as to saturate the

photoelastic response, as discussed previously). For the stiffest particles (PSM-1), the vast majority of the data is either in the linear response regime or below the minimum pressure required to observe a photoelastic response. The data for softer particles (Shore 60A and 80A) tend to have a pressure in the linear response or saturation regime, depending on the speed and size of the intruder.

Processing of photoelastic images is done by first removing the background intensity, which is the pixel brightness measured for unstressed grains and voids between particles. The background intensity is obtained by taking a reference image before the intruder enters into the field of view. The PSM-1 particles are sufficiently stiff that gravitational loading produces no measurable photoelastic response, so this reference image can simply be blurred to give a background intensity map. The softer particles (60A and 80A) have significant photoelastic response due to gravitational loading, so a small amount of image processing must be done to remove the photoelastic response and obtain a suitable background intensity image.

Once a background intensity image is obtained, each photoelastic image is normalized by either subtracting off or dividing by the background image. A normalized photoelastic image can be used to measure pressure in two ways: intensity, where the actual pixel values are used to approximate local pressure, or gradient squared (G^2), which is the square of the local derivative of the image intensity. These two measures give similar results, but they may be better or worse at handling various kinds of noise, depending on the video settings and particles used. The key is to find a protocol which gives well calibrated data, and the best algorithm differs for each experiment.

2.2.3 Obtaining Particle Flow Fields

The trajectories of particles cannot easily be obtained from photoelastic images due to the vast intensity difference between bright and dark particles (Fig. 2.4). To track

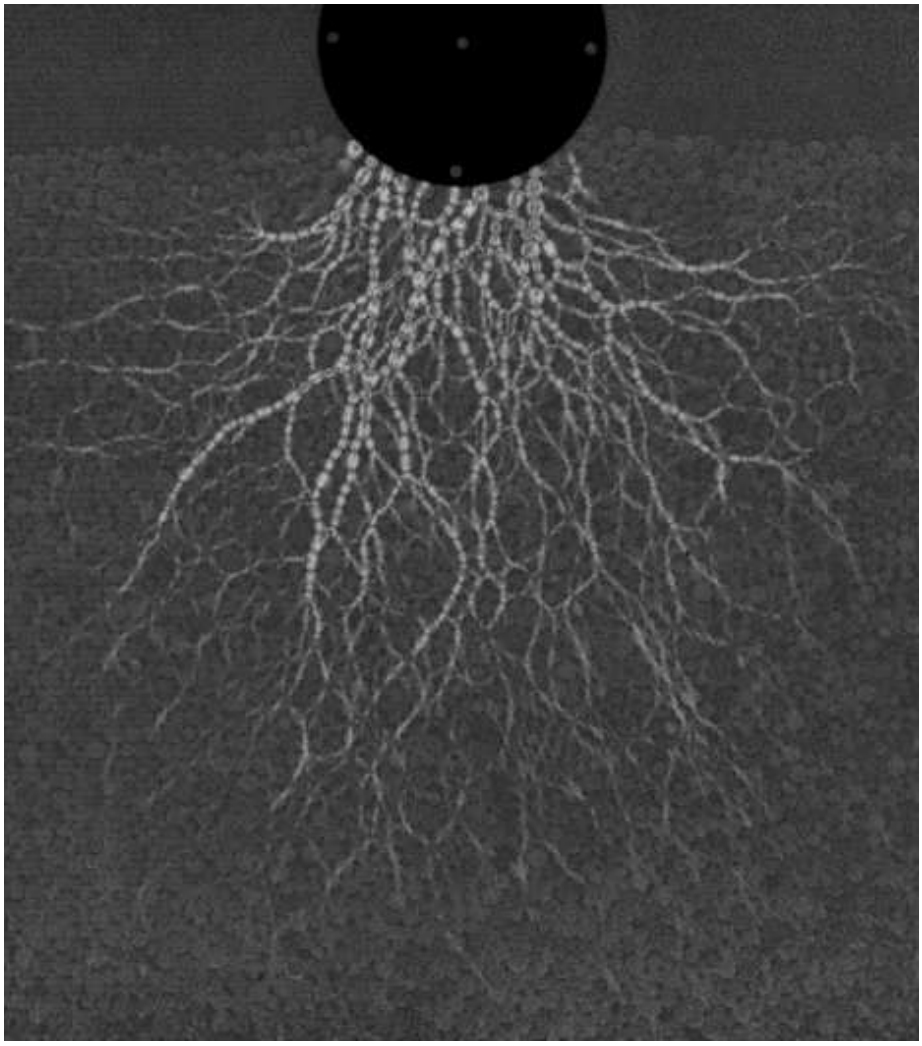

FIGURE 2.4: The same image from Fig. 2.2 after the background light inhomogeneities have been removed with image processing.

particle motion, one must remove at least one of the polarizers from the optical setup. In this case, light scatters off the edges of particles, making the outlines of particles appear slightly darker, and the interior of particles also appears slightly darker as well, depending on the degree of transparency of the bulk material from which the particles are cut.

In the case of moderately translucent particles with sufficiently large pixel resolution per particle, the trajectories of the particles can be tracked by locating them at each frame, using a Hough transformation algorithm (Ballard, 1981; Majmudar, 2005; Ren et al., 2013). The softer, polyurethane particles (60A and 80A) meet these criteria, so particle tracking can be used. This allows measurement density and momentum fields as well, since particle masses, positions, and velocities are all known. Another method called particle image velocimetry (PIV) can measure particle flow fields by correlating successive frames and deducing how much and in which direction sections of that image moved to form the next image (Grant, 1997). This is a standard image processing technique, which is available in several open-source software packages, such as ImageJ and OpenPIV. This method is much faster and easier than particle tracking, and it can be used to closely approximate the coarse-grained velocity or momentum field without tracking each particle from frame to frame. The stiffest particles (PSM-1) are extremely transparent and cannot be easily tracked, so PIV must be used instead.

3

Granular Impact: Dominated by Fluctuations

In this chapter, as well as the three that follow, I will focus on granular impact into the stiffest photoelastic disks (PSM-1). These impacts have initial intruder velocities, $v_0 \leq 6.6$ m/s, which are just fast enough that inertial effects become important but still slow enough to be solidly in the subsonic regime (i.e., the intruder speed is typically two orders of magnitude slower than the speed of force transmission through the material). In the PSM-1 particles, a typical acoustic speed is approximately $c = 300$ m/s, which means that the ratio of intruder speed to granular force propagation speed is always less than ~ 0.02. Since this acoustic speed is similar to granular systems of sand or glass beads, this regime, where $v_0 \ll c$, is the same one investigated in many previous studies, particularly those using macroscopic force laws dominated by velocity-squared drag forces, as in equation (1.8).

A force law such as (1.8) suggests trajectories $z(t)$ which are smooth, particularly with the simple forms for $f(z)$ and $h(z)$ that are typically used (i.e., constant or linear in z). Photoelastic videos of impacts into hard particles, however, reveal a process which appears anything but smooth, as shown in Fig. 3.1, which shows video frames as well as quantitative plots of the photoelastic response in a region beneath

the leading edge of the intruder. The photoelastic response is strongly fluctuating in both space and time and characterized by complex propagating force networks generated intermittently near the leading edge of the intruder. These dynamic force chains propagate away from the intruder into the bulk of the granular material and dissipate. In this chapter, I will demonstrate that the strongly fluctuating photoelastic response observed in videos represents the dominant mechanism of energy loss in this process. Additionally, the intruder trajectories are still consistent with force laws in the class of equation (1.8). So, while these smooth, macroscopic force laws describe the intruder trajectories on average, the deceleration is not smooth but is dominated by large fluctuations connected to intermittent force pulses which carry energy and momentum away into the granular material.

3.1 Force on Intruder from Photoelastic Calibration

As discussed in Chapter 2, the velocity and acceleration are computed using filtered derivatives of $z(t)$, the trajectory obtained from photoelastic videos. Each derivative is computed by performing linear fits using N points, centered at the point of interest. For $N > 50$, the fluctuations in the velocity, $v(t)$, appear very small, less than 0.1 m/s. However, fluctuations in the acceleration data, $a(t)$, persist, even for $N \gg 100$. We refer to the acceleration measured at an intermediate time scale as a_{int}, where the time scale, $t_{int} \simeq N\Delta t$ depends on the value of N used (where Δt is the time between frames). Sample trajectories of circular intruders with three different diameters are shown in Fig. 3.2, including large fluctuations in the acceleration data. The persistence of these fluctuations in filtered acceleration suggests that the fluctuations in the acceleration are *physical* and not simply an artifact of experimental error in tracking the intruder.

To test this, we compare the acceleration to the photoelastic response, as discussed in the previous chapter, for the bronze circular intruder with diameter $D =$

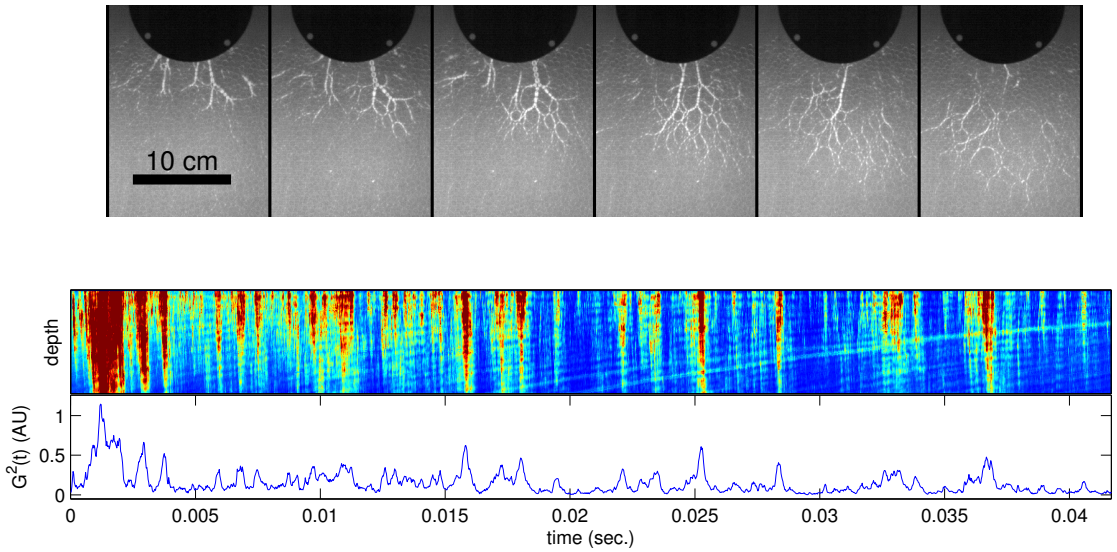

FIGURE 3.1: Top panel shows six selected frames, starting at 2.75 ms after impact and spanning 475 μs, showing a typical compressional event which generates an acoustic pulse, which disconnects from the intruder. The middle panel shows a space-time plot of G^2 in an angular region under the bottom half of the intruder (half-annulus) over time, with a radial thickness equal to the intruder radius. The horizontal axis is time, and the vertical axis is radial distance from the bottom of the intruder. So, each pixel in the space-time plot represents the total photoelastic response in a particular frame for all pixels which are a certain distance away from the center of the intruder. The top row of the plot corresponds to the bottom edge of the intruder, and subsequent rows are increasing distance away from the intruder center. The slope of the disturbances gives an acoustic speed of $\sim$ 325 m/s. The bottom panel shows the sum of the response in the space-time plot above, after subtracting background inhomogeneities. Calibrating this yields a measurement of instantaneous force, as shown later, where the range shown above [0 to 1.1 arbitrary units (AU)] maps to an intruder acceleration range of 0 to 27 g.

12.7 cm. We use G^2 of the photoelastic response in an angular region extending radially outward from the bottom half of the intruder over a length of about 10 particle diameters, forming a half-annulus. Since the majority of photoelastic activity occurs directly beneath the center of the intruder, the results are fairly insensitive to the changes in the exact dimensions of this region, as long it covers most of the region directly beneath the intruder center. A space-time plot of the pixel brightness in

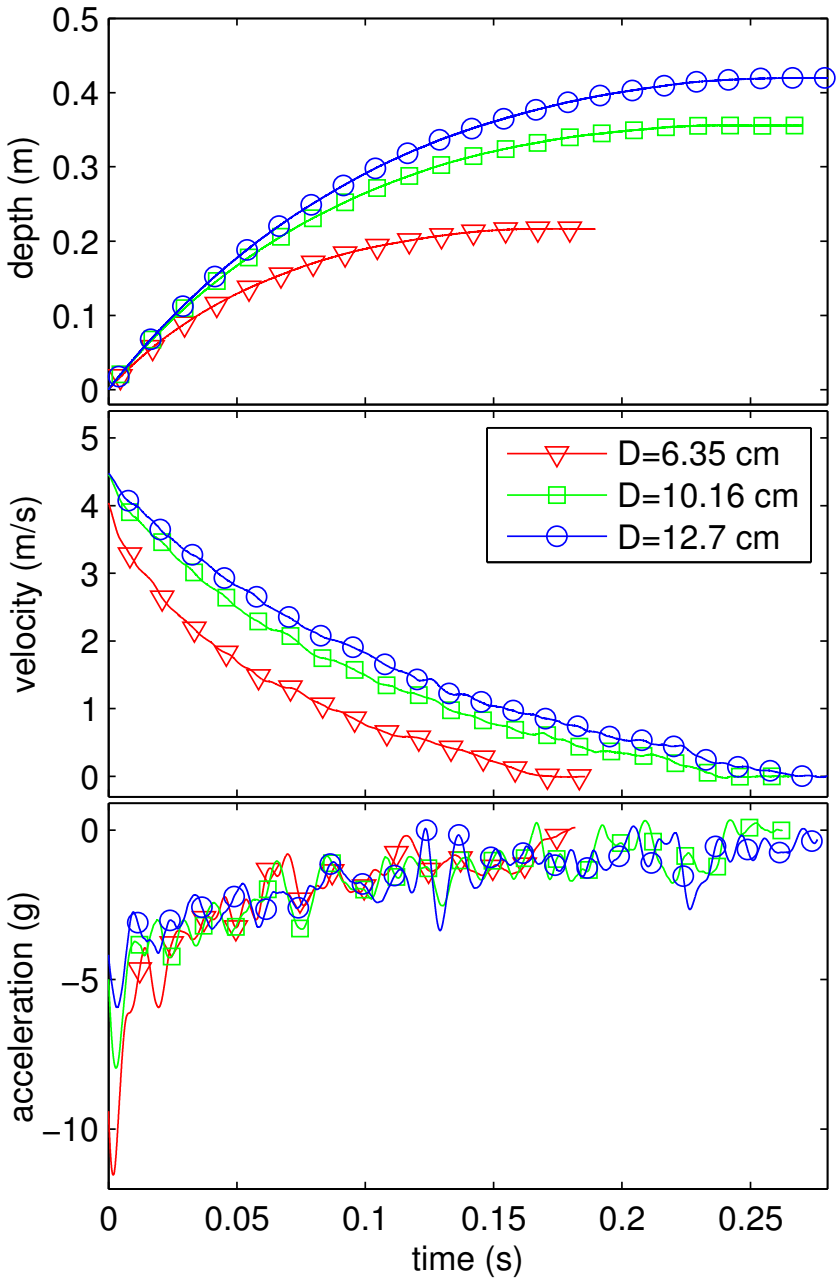

FIGURE 3.2: Single trajectories (depth, velocity, and acceleration) for the three smallest circular intruders with similar initial impact velocities, where $t = 0$ is the first contact with the granular surface, measured from photoelastic response.

this region, as well as the total G^2 versus time, are shown in Fig. 3.1. We compare G^2 in this region to $a(t)$ calculated with $N = 300$ (Fig. 3.3). Photoelastic data are obtained at 40 kHz, which is about 500 times faster than time resolution for a_{int}. Comparing a_{int} to the photoelastic response G^2 requires time-filtering the photoelastic data such that the time scale matches that of a_{int}. This gives a comparison at the intermediate time scale; a plot (Fig. 3.3) of a_{int} and filtered G^2 data gives the same curve, showing that the two are virtually identical. For this comparison, we first calibrated G^2 to a linear function which gives optimum agreement between filtered G^2 and a_{int}, but this normalization matches well with the static calibration of G^2 (shown in the inset of Fig. 3.3). We conclude that the large photoelastic events are the main force mechanism acting on the intruder. By inference, the energy loss for the intruder is tied to these acoustic events. The excellent agreement between the photoelastic force measurements and the observed trajectories gives good reason to use the calibrated photoelastic data as a measurement of instantaneous force at the full frame rate of the camera, 40,000 fps.

While increasing N reduces fluctuations in the measured trajectory caused by tracking noise, it also smooths out physical fluctuations. The value $N = 300$ was chosen primarily because of the good agreement between photoelastic data and acceleration data, as shown in Fig. 3.3. However, the crossover from noise-dominated fluctuations to physical fluctuations can be investigated systematically by examining the root-mean-square (RMS) of the fluctuations in the acceleration signal, $a(t, N)$, versus filter size, N. For reference, we compare this to the RMS value of the fluctuations in two other quantities: a_{noise} and $G^2(t)$. The noise signal is calculated purely from error in locating the intruder's position (i.e. a_{noise} is the acceleration computed on an intruder which is not moving). Additionally, we examine the fluctuations in $G^2(t)$. Fluctuations for all three are obtained by dividing the measured signal by an average signal which is obtained by fitting a low-order polynomial to the measured

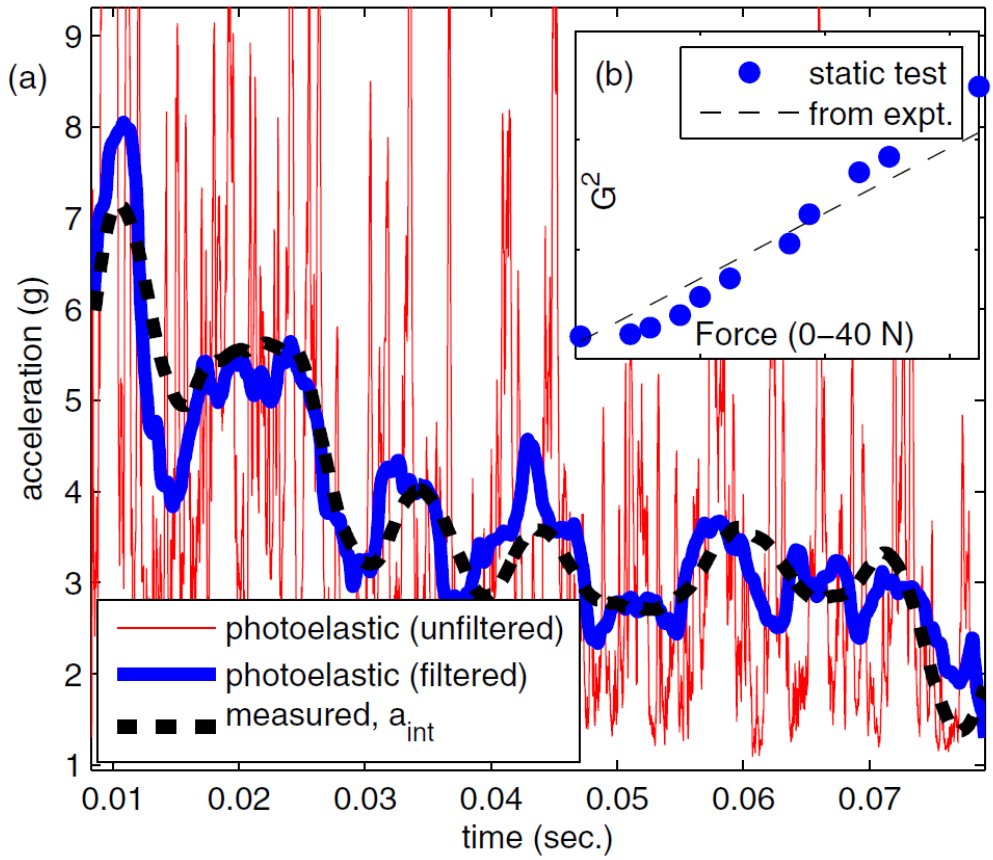

FIGURE 3.3: Comparing the intruder trajectory to the photoelastic response from the bottom panel of Fig. 3.1 shows that the intruder acceleration is very well correlated to the photoelastic or acoustic fluctuations in high-speed videos. We time-average the photoelastic response (thick, blue line) to match the time scale of the acceleration measurement a_{int} (black, dashed line), which has limited time resolution. Rescaling the photoelastic measurement gives extremely close agreement with the measured deceleration (both the mean and fluctuations). The calibrated photoelastic force measurement without time filtering (thin, red line) shows much larger fluctuations at a much shorter time scale. The inset shows the calibration of photoelastic response versus 2D pressure (force per width of intruder or piston) from experiment (black dashed line) and from a static test (blue circles), with good agreement.

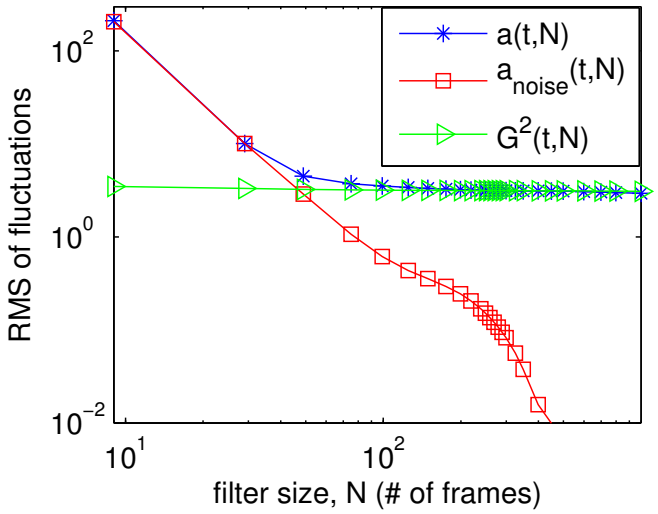

FIGURE 3.4: Plot of $\eta_{rms}(N)$, the RMS of the fluctuations as a function of N, which is the filter size used to compute the acceleration. We plot the RMS of $a_{noise}(t, N)$, as well as the relative fluctuations from $a(t, N)$ and $G^2(t, N)$ (see text). The bump in the a_{noise} curve corresponds to flickering of the lighting in the system at 120 Hz. The acceleration fluctuations clearly show a transition from a noise-dominated regime to one which matches the photoelastic time series, $G^2(t)$, which we calibrate as an estimate of instantaneous force at 40 kHz.

signal. By plotting all three of these quantities together as a function of filter size N or Δt, as shown in Fig. 3.4, we observe that the fluctuations in $a(t, N)$ undergo a transition from a regime dominated by noise ($N < 50$) to one which matches the photoelastic signal ($N > 100$). At $N \approx 300$, the signal-to-noise ratio is approximately 10:1.

3.2 Dissipation of Acoustic Pulses

Once the acoustic pulses have moved ahead of the intruder, there must be a dissipation mechanism of these disturbances within the material. Hence, it is important to examine how fast and how far the acoustic pulses propagate. This is accomplished

by observing the photoelastic response in a long, thin angular slice, centered directly beneath the intruder with a width of $\pi/8$, which extends $25d$ beneath the intruder. Space-time plots of the response in this region indicate a wave speed of about 325 m/s ($\sim$1/10 of the sound speed in the bulk material from which the particles are cut). To determine the attenuation of the acoustic pulses, we plot normalized intensity versus depth. The normalization for each pulse is the cumulative photoelastic response G^2 over its full duration. The normalized photoelastic response averaged over multiple events shows an exponential decay (Fig. 3.5), with a decay length of $\sim$10 particle diameters, which is short enough that reflections from the bottom or sides of the container are not important. It is unclear which grain-scale interactions are responsible for this decay, but it could be explained by force-chain splitting, grain-grain friction, restitutional losses for each "collision," or other dissipative mechanisms.

3.3 Consistency with Force Laws

Now that a grain-scale physical picture is in place, an important question is whether these trajectories are even consistent with force laws such as equation (1.8). One way to determine this is to take many trajectories with different initial velocities and examine each of them at a particular depth, $z = \zeta$. In this case, equation (1.8) becomes:

$$m\ddot{z} = mg - f(\zeta) - h(\zeta)\dot{z}^2. \tag{3.1}$$

If this model is valid, plotting $\ddot{z}$ versus $\dot{z}^2$ for each trajectory, calculated at $z = \zeta$, yields an approximately straight line of slope $h(\zeta)$ and intercept $g - f(\zeta)/m$. An example of this is shown in Fig. 3.6. Each data point represents a trajectory, measured at $z = \zeta$. The scatter is the result of physical fluctuations which persist in the acceleration due to fluctuations discussed previously. By repeating this process at many different values of ζ, $f(z)$ and $h(z)$ can be measured and used to plot the

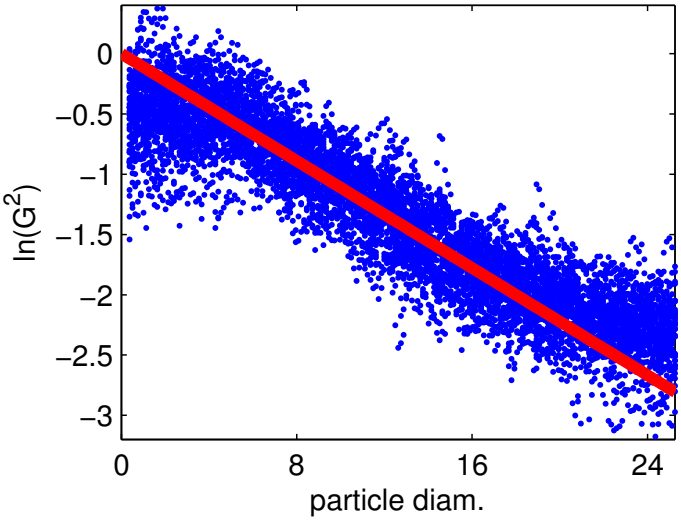

FIGURE 3.5: Photoelastic pulses decay as they propagate away from the intruder. We observe a thin angular slice of opening angle of $\pi/8$ rad, extending $25d$ below (d is the particle diameter, taken to be 6 mm), and centered directly beneath the intruder. We use 40 different pulses from different impacts of a single intruder ($D = 12.7$ cm), where the intruder velocity at the pulse emission varies between 2 and 6 m/s. We then plot the natural logarithm of G^2 per area as a function of depth for each pulse, normalized by the total intensity in the pulse (wave intensity will decrease as $1/r$ moving away from a point source in 2D, and this effect has already been accounted for in this plot). The imposed fit (thick, red line) is $\exp(-r/L)$, where L is the decay length, roughly 10 particle diameters.

predicted instantaneous acceleration according to the force law, given the depth and velocity curves. This prediction is shown in Fig. 3.6, along with several acceleration curves calculated with varying values of N. As N is increased, the acceleration curve approaches the prediction of the force law. Often, $h(z)$ is approximately constant and $f(z)$ is monotonically increasing with depth. We return to the issue of calculating $f(z)$ and $h(z)$ in Chapter 5.

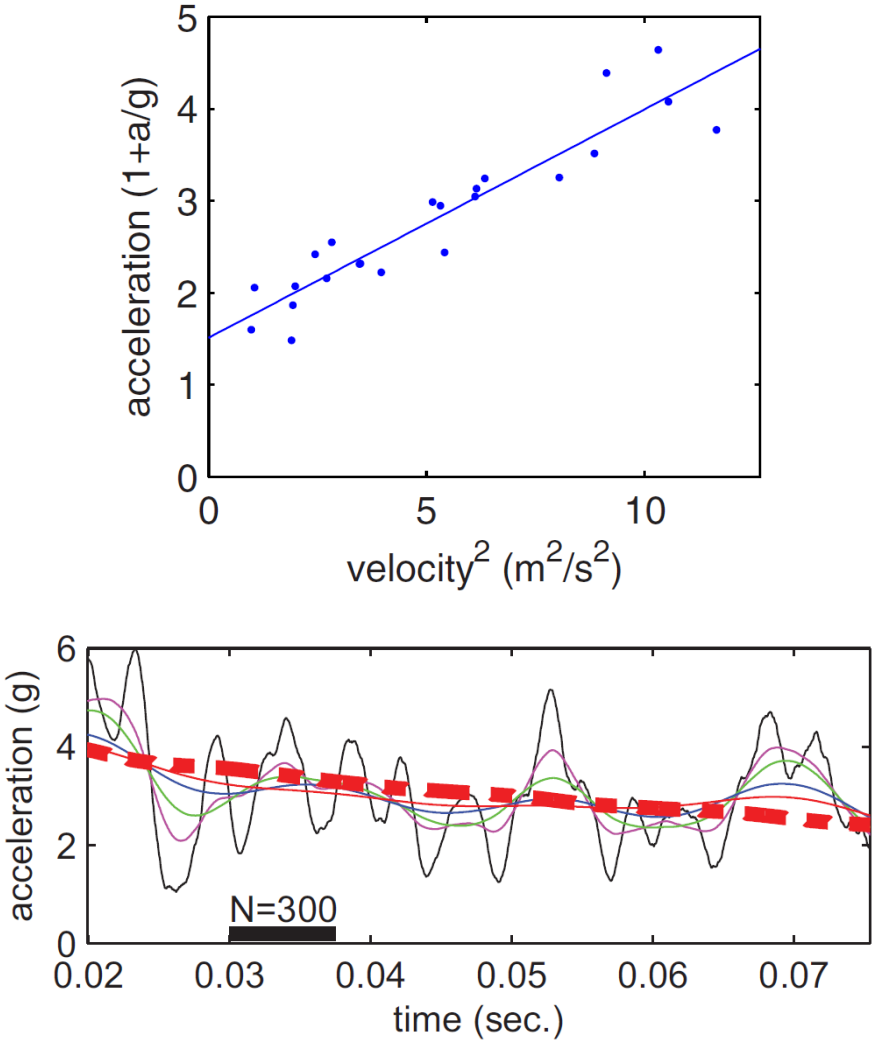

FIGURE 3.6: Top panel shows a plot of acceleration versus velocity squared for a circular intruder at a fixed depth, $z = \zeta$, where each of the 23 data points shown represents one trajectory from experiments described later in the text. The linear fit shown, $1 + a/g = C_0 + C_1 v^2$, has $C_0 = 1.5$ and $C_1 = 0.25$, which correspond to $f(\zeta)$ and $h(\zeta)$. Bottom panel shows plots of acceleration computed with different filter sizes, with $N = 100, 200, 300, 500, 700$ (smaller filter sizes correspond to larger fluctuations). The red dashed line represents a_{mean}, the prediction of the model from (1.8), where $f(z)$ and $h(z)$ are computed from the aggregate of all trajectories, as discussed in the text.

3.4 Summary

The chapter has focused on three important results. First, the intruder deceleration is dominated by intermittent acoustic activity generated at the leading edge of the intruder. This means that the deceleration is not smooth or steady, but it is dominated by intermittent collisions with force-chain-like structures which send energy and momentum away in almost discrete bursts. The acoustic pulses generated in this process decay exponentially as they travel through the granular medium. Second, the excellent agreement of the photoelastic measurement with the measured deceleration of the intruder gives strong evidence that it can be used as a measure of the instantaneous force, measured at 40 kHz. This allows investigation of the statistics of force fluctuations around the mean behavior, which we return to in the next chapter. Third, despite the extremely large fluctuations which dominate this process, the macroscopic force laws, equation (1.8), still appear to capture the dynamics on average (i.e., time scales significantly longer than the fluctuation time scales). We discuss fitting to these force laws in more detail in Chapter 5.

4

Properties and Statistics of Force Fluctuations

One important result from the previous chapter is that the instantaneous force on the intruder is strongly fluctuating on short time scales, yet can be well captured by a macroscopic force law, Eq. (1.8), on longer time scales. As a way to capture both of these properties, one might modify Eq. (1.8) to be:

$$F(z, \dot{z}, t) = mg - [f(z) + h(z)\dot{z}^2]\eta(t). \tag{4.1}$$

Here, $\eta(t)$ is a *multiplicative* stochastic term, as opposed to additive, which should have a mean of unity. This means that the characteristic size of force fluctuations scales with the mean, which is set by the dynamics. Additionally, it is dependent only on time, and otherwise decoupled from the dynamics (that is, it is independent of depth or velocity). Thus, in this form, any time scales associated with the fluctuations are independent of the intruder dynamics, and the fluctuations do not "stretch out" in time as the intruder slows down. The remainder of this chapter will demonstrate experimental evidence for these choices and discuss their physical implications.

We also note that in Eq. (4.1), both granular forces, $f(z)$ and $h(z)\dot{z}^2$, are fluctu-

ating as described by $\eta(t)$; alternatively, one might guess that the fluctuating term relates only to the collisional stress, $h(z)\dot{z}^2$. In fact, experimental noise in our system makes this distinction difficult.

Given that the instantaneous force is well captured by a calibrated G^2 measurement, and that the average force approaches a macroscopic force law for long times, we approximate the force fluctuations as $\eta(t) \sim G^2(t)/G^2_{avg}(t)$ (Figs. 4.1 and 4.2), where $G^2(t)$ is the photoelastic time series used to measure force (e.g., bottom of Fig. 3.1) and $G^2_{avg}(t)$ is the mean behavior, obtained by fitting a low-order polynomial to $G^2(t)$.

4.1 Fluctuations are Multiplicative

Equation (4.1) has a fluctuating term which is multiplied by the slow behavior, since the size of the fluctuations appears to decrease with the average behavior, as shown in Fig. 4.1. The plot of $\eta(t) \sim G^2(t)/G^2_{avg}(t)$ in Fig. 4.2 supports this choice, since dividing by the mean appears to yield a fluctuating signal with a characteristic size which is constant.

Additionally, the inset Fig. 4.1 shows a quantitative comparison of the size of the fluctuations in the force as a function of the mean force: the size of the RMS of $G^2(t) - G^2_{avg}(t)$ for a small time window (i.e. the standard deviation) is plotted on the $y-$axis, and the local value of $G^2(t)$ is plotted on the $x-$axis. This shows a quasi-linear relationship with approximate slope of 0.71 (the solid red line shows a slope of 1). Thus, the fluctuations are multiplicative, since the size of the fluctuations scales with the mean (i.e. $G^2(t) \sim G^2_{mean}\eta(t)$).

The form of a stochastic differential equation, particularly how the fluctuations or noise term appears, is directly tied to the microscopic processes which it describes. Physically, multiplicative fluctuations correspond to fluctuations which have their microscopic origins in the dynamics. That is, the force fluctuations are created by

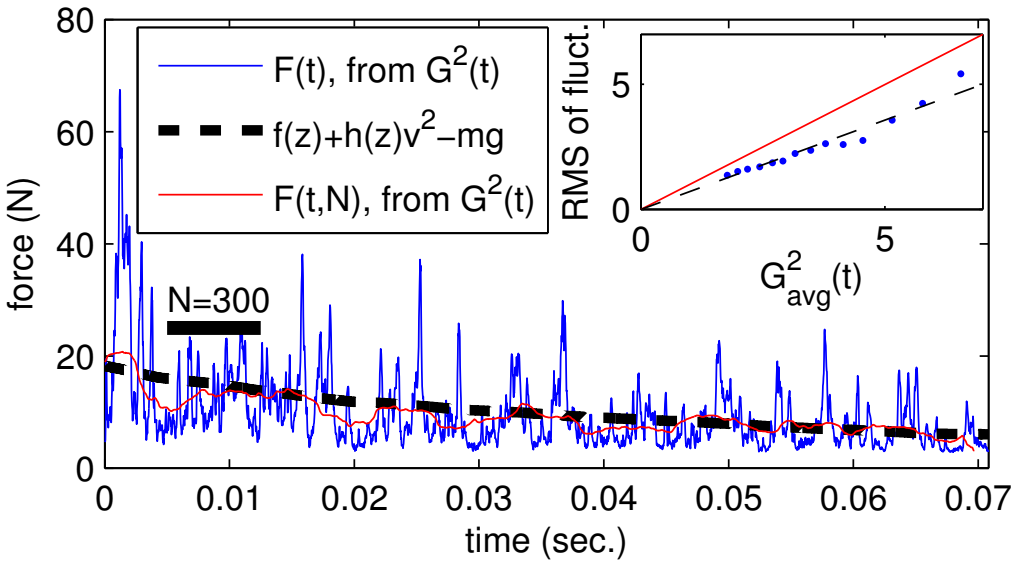

FIGURE 4.1: A plot of instantaneous upward force, calibrated from $G^2(t)$, on a circular intruder (diameter of 12.7 cm) as it moves through the granular material). The black dashed line shows $F_{mean} = mg - f(z) - h(z)^2$. The thin red line shows a time-filtered version of the instantaneous force to show that it follows F_{mean} closely. The inset shows a plot of the RMS of the fluctuations in the photoelastic signal as a function of the mean. The RMS of the fluctuations linearly increases with the mean, with approximate slope of 0.71 (black dashed line); fluctuations distributed purely exponentially (i.e. with no cutoff near zero) would yield a slope of unity (red line).

the dynamics, not by external driving of some kind, and they stop when then intruder stops moving. This is in contrast to additive fluctuations, which are very common in stochastic differential equations (such as the Fokker-Planck equation for Brownian motion) and arise from external driving or thermal noise of some kind.

4.2 Time Dependence of Fluctuations is Decoupled from Dynamics

While the mean and characteristic size depend on the intruder dynamics, the fluctuations in Fig. 4.2, which have been normalized, appear to be statistically stationary

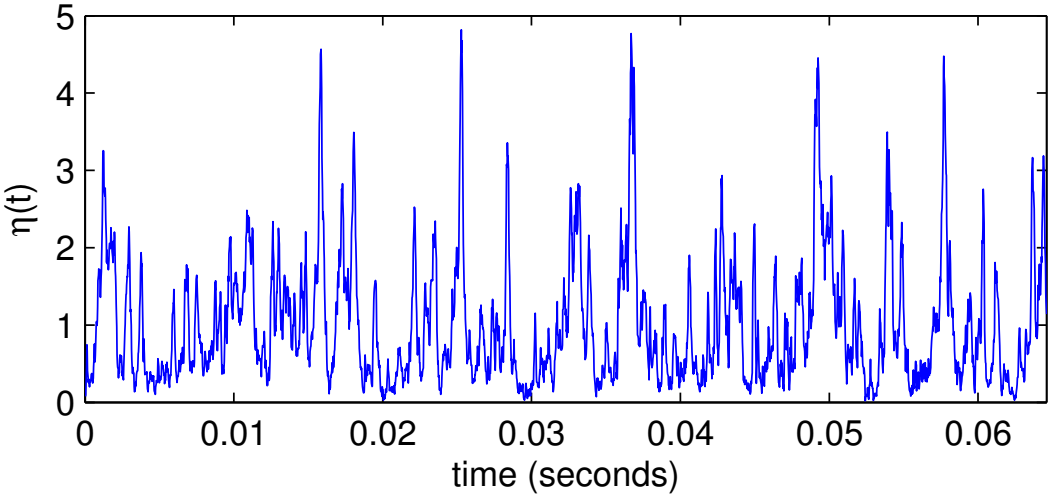

FIGURE 4.2: The fluctuating term $\eta(t)$ for a single impact (typical for all impacts), where $\eta(t) \sim G^2(t)/G^2_{avg}(t)$, as discussed in the text.

in time. That is, the characteristic time scale does not change as the intruder slows down. To test this, we compare the statistics for the normalized fluctuations, η, with different velocities from 15 different impacts with a single intruder (circular intruder, diameter 12.7 cm). We discard the first 5 ms, which typically contains a large force event, as seen in Fig. 4.1. After this initial transient, we sort all data into velocity ranges: 1 to 2 m/s, 2 to 3 m/s, and greater than 3 m/s. Figure 4.3 shows that the fluctuations in these three sections obey almost identical statistics, suggesting that the fluctuations are decoupled from the dynamics. The distribution of the fluctuations has an exponential tail, $P(\eta) \sim e^{-\eta}$, with a cutoff near zero, and an autocorrelation time of about 1 ms.

To test further, we examine the statistics of the time between fluctuation peaks for these same trajectories, as shown in Fig. 4.4. Peaks are taken as local maxima in $\eta(t)$, with $\eta > 1.5$ (i.e. 50% larger than the mean value at that time). For moderate velocities, $1.5 < v < 4.5$ m/s, which constitute the bulk of the dynamics, the average

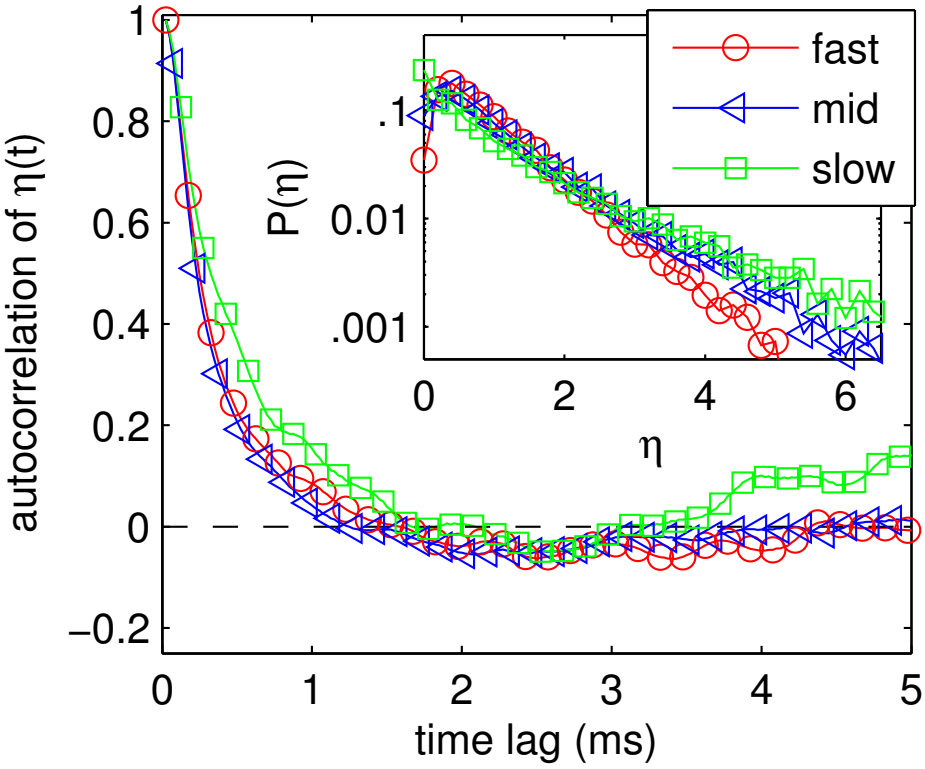

FIGURE 4.3: Comparison of fluctuation statistics from 15 different impacts, with all data sorted as a function of velocity range: 1 to 2 m/s (slow), 2 to 3 m/s (mid), and greater than 3 m/s (fast). The inset shows the probability distribution function, and the main figure shows the autocorrelation function of the signal. As shown, the statistics are very similar, suggesting that the mean force is set by the dynamics, but the fluctuations are virtually independent of the dynamics.

time between peaks, $\langle \Delta t_p \rangle$, is virtually independent of the intruder velocity, as is the standard deviation, $\langle \Delta t_p^2 \rangle - \langle \Delta t_p \rangle^2$ (Fig. 4.4). For slow velocities, $v < 1.5$ m/s, we observe an increase in average peak spacing, which says that the fluctuations slow down or weaken as the intruder comes to a stop. For fast velocities, $v > 4.5$ m/s, we observe a sharp decline in peak spacing, which arises from a high density of large photoelastic events for fast initial velocities immediately after initial impact.

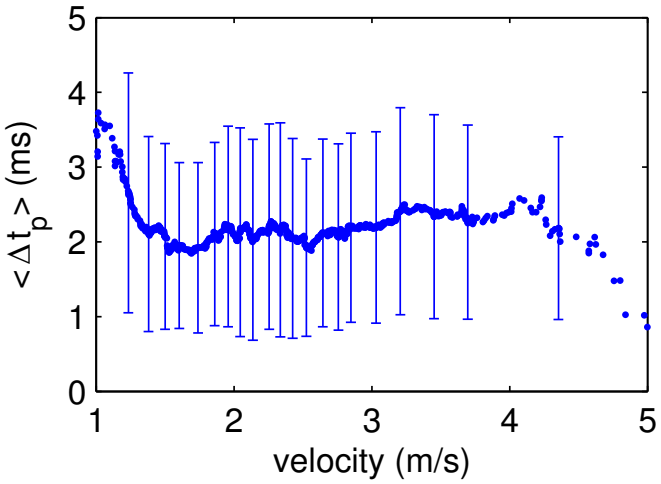

FIGURE 4.4: Plot examining the average time between peaks in $G^2(t)$. A peak is defined as a local maximum 50% greater than the local mean behavior. The plot shows the average time between peaks, $\langle \Delta t_p \rangle$. Each point represents an average of 200 pairs of peaks, taken from 20 different trajectories with varying initial velocities. Error bars have width equal to the standard deviation, $\langle \Delta t_p^2 \rangle - \langle \Delta t_p \rangle^2$. The average and standard deviation of time between peaks are virtually independent of the intruder velocity, except for very large and very small velocities, as discussed in the text.

These two measures are strong confirmation that the fluctuations, η, are stochastic in time and otherwise independent of the intruder dynamics. This says that the time scale in the fluctuations is set by acoustic properties of the granular material. Alternatively, one might imagine that the fluctuations are fundamentally geometrical, and the time scale is set by the characteristic distance which the intruder must travel to rearrange particles and break force chains. This time would change as the intruder slowed, and thus the fluctuation time scale would be dependent on how fast the intruder was moving, which does not occur here.

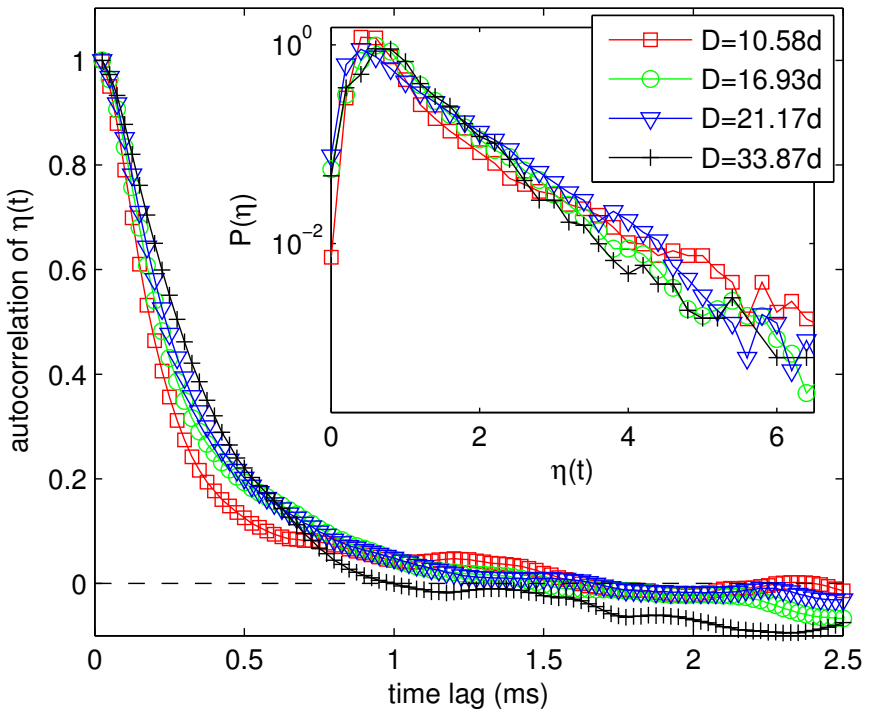

FIGURE 4.5: The autocorrelation (main figure) and the PDF (inset) of the combined fluctuating signals for all impacts for each intruder (∼20 runs per intruder). The semilog PDF plot shows $P(\eta) \sim \exp(-\eta)$. We see an autocorrelation time of ~ 1 ms, which gives a typical event time, which agrees with video frames in Fig. 3.1. The lack of dependence on intruder size suggests a collective mechanism and not a simple combination of uncorrelated, random force chains.

4.3 Fluctuations are Spatially Correlated

If we examine the fluctuations, η, for different sized circular intruders, as shown in Fig. 4.5, we observe a surprising result: the statistical properties of the force fluctuations are almost independent of intruder size for the sizes tested ($D = 6.35, 10.16, 12.7,$ and 20.32 cm). This suggests that the fluctuations are somehow correlated spatially, which can be proved by contradiction in the following way.

Consider the case where fluctuations are spatially uncorrelated. In this case, force chains would be excited quasi-randomly at some location at the intruder edge, and this contact force would be uncorrelated with the contact force some finite distance away. If this picture were correct, then increasing the intruder size should include more of these uncorrelated regions. By the central limit theorem, this would make the fluctuations narrower and more Gaussian, regardless of the statistics of any one region. However, this does not occur, suggesting some kind of subtle collective mechanism, such as persistence of a spatial force network that is repeatedly excited by the intruder.

4.4 Summary

This chapter has discussed three important statistical properties of the force fluctuations observed in these granular impact experiments. First, the characteristic size of the fluctuations (mean and standard deviation) are set by the instantaneous intruder dynamics. Second, the normalized fluctuations are otherwise decoupled from the intruder dynamics, and the time scale of the fluctuations does not change as the intruder slows down. Third, the fluctuation statistics are independent of intruder size for the range used here, which is inconsistent with a simple, spatially uncorrelated picture. These statistical properties should be a direct result of grain-scale physics, but further investigation is required to make this connection.

5

Fitting to a Force Law: A Kinetic Energy Approach

Thus far, we have examined granular impact in the context of a macroscopic model, Eq. (1.8). However, theoretical and experimental application of this equation reveals several problems. First, equation (1.8) cannot easily be integrated and solved to obtain the closed-form solutions for the trajectory, $z(t)$ and $v(t)$, for general $f(z)$ and $h(z)$. To do this, or even to obtain the final stopping time and depth, one must assume specific forms for $f(z)$ and $h(z)$, typically that they are constants (Allen et al., 1957; Forrestal and Luk, 1992; Goldman and Umbanhowar, 2008; Tsimring and Volfson, 2005). But, this is a very narrow assumption which is inconsistent with several experimental studies (Katsuragi and Durian, 2007; Goldman and Umbanhowar, 2008; Umbanhowar and Goldman, 2010), including the experiments presented in this thesis, as this chapter will show. Additionally, as discussed in Chapter 3, experimental comparison to these models requires depth, velocity, and acceleration data for the intruder for a large number of trajectories with many different initial velocities. However, obtaining accurate acceleration data at short time scales can be difficult, since accelerometers have limited time-resolution, and discrete differentiation from position data greatly amplifies measurement noise. Finally, as the last two chapters have

shown, acceleration measurements can contain large *physical* fluctuations at short time scales, which makes precise determination of $f(z)$ and $h(z)$ difficult, as shown in Fig. 3.6. In contrast, the fluctuations in velocity data are considerably smaller, which is a crucial point in the analysis presented in this chapter.

This chapter focuses on a new approach to this force-law model, where equation (1.8), a nonlinear differential equation for depth versus time, is reformulated into a *linear* differential equation in kinetic energy. We show that this approach addresses all of the aforementioned issues. Mathematically, it allows formal closed-form trajectory solutions without specific assumptions on $f(z)$ and $h(z)$. These solutions then provide a natural way to experimentally measure $f(z)$ and $h(z)$ using only velocity and depth data, with no assumptions about the functional form of these terms.

In this chapter, I will present the mathematical framework and use it to calculate the force law terms, $f(z)$ and $h(z)$. The observed $f(z)$ is monotonically increasing with depth, and is fairly well approximated by a linear function, $f(z) = f_0 + kz$. Additionally, the observed $h(z)$ term is approximately constant, denoted by h_0, for the majority of the trajectory, except for an initial transient at impact, near $z = 0$. The value of h_0 shows strong dependence on the intruder size and shape, which is the focus of the next chapter.

5.1 Kinetic Energy Formulation

5.1.1 Writing Closed-Form Trajectories

By using a relation that is familiar from the work-energy theorem of mechanics—$m\ddot{z} = dK/dz$—equation (1.8) can be recast from second order in time for z to first order in depth for kinetic energy of the intruder, $K = \frac{1}{2}m\dot{z}^2$.

$$\frac{dK}{dz} = mg - f(z) - \frac{2h(z)}{m}K. \tag{5.1}$$

This yields an inhomogeneous *linear* ordinary differential equation (ODE) with generally nonconstant coefficients. So, while equation (1.8) is nonlinear, equation (5.1) is a linear ODE, and standard ODE methods immediately yield formal solutions for $K(z)$:

$$K(z) = K_p(z)(K_0 + \phi(z)). \tag{5.2}$$

where K_0 is the kinetic energy at impact,

$$K_p(z) = \exp\left(-\int_0^z (2/m)h(z')dz'\right), \tag{5.3}$$

and

$$\phi = \int_0^z dz'[mg - f(z')]/K_p(z'). \tag{5.4}$$

At this point, the kinetic energy is known as a function of depth, and the trajectory is solved in principle. The velocity can be written as:

$$\dot{z}(z) = \frac{dz}{dt} = \left[\frac{2}{m}K_p(z)(K_0 + \phi(z))\right]^{1/2}, \tag{5.5}$$

and $z(t)$ follows by integrating and inverting:

$$t(z) = \int_0^z dz' \left[\frac{2}{m}K_p(z')(K_0 + \phi(z'))\right]^{-1/2}. \tag{5.6}$$

If the forms of $f(z)$ and $h(z)$ are simple, much of the calculation of these integrals can by done explicitly. For example, using the commonly assumed forms $f(z) = f_0 + kz$ and $h(z) = b$, we obtain $K(z)$ as

$$K(z) = (K_0 - c_1)\exp(-c_2 z) + c_1 - c_3 z. \tag{5.7}$$

Here, the constants are $c_1 = [(mg - f_0)c_2 + k]/{c_2}^2$, $c_2 = 2b/m$, and $c_3 = k/c_2 = km/(2b)$.

Since many experimental studies have focused primarily on the final stopping depth versus the initial kinetic energy at impact, it is important to note that equation (5.2) immediately yields a relation for the stopping depth, even without integrating equation (5.6). This can be done by setting $K(z_{stop}) = 0$, or $\phi(z_{stop}) = -K_0$, yielding the stopping depth as a function of impact energy, K_0. Specifically, for the common case described by equation (5.7), the stopping depth, z_{stop} satisfies

$$z_{stop} = \frac{m}{2b} \log \left[\frac{\frac{2b}{m} K_0 + \left(f_0 + \frac{km}{2b}\right) - mg}{\left(f_0 + k z_{stop} + \frac{km}{2b}\right) - mg} \right] \tag{5.8}$$

Note that if we take $f(z)$ as roughly constant, $f(z) = f_0$ and $k = 0$, then z_{stop} increases logarithmically with K_0, as in Eq. (1.9) (Tsimring and Volfson, 2005; Goldman and Umbanhowar, 2008; Forrestal and Luk, 1992).

$$z_{stop} = \frac{m}{2b} \log \left[1 + \frac{2b}{m} \left(\frac{K_0}{f_0 - mg} \right) \right] \tag{5.9}$$

This approximation is relevant in the limit of high impact energy, where $b\dot{z}^2$ dominates. In the low energy limit, it predicts $z_{stop}(K_0 = 0) = 0$. However, we know from experience that a massive intruder must be at least partially submerged to be supported by frictional grains. This occurs at a depth which increases with intruder size. So, when $K_0 \to 0$, one might guess that $z_{stop}(K_0 = 0) \sim D$. Note that equations (5.7) and (5.8) may yield a nonzero upward force, $F = \frac{dK}{dz}$, as the intruder comes to a stop. This means that the force law model must be modified as the intruder comes to a stop; we return later to this issue.

5.1.2 Measuring $f(z)$ and $h(z)$

In addition to its mathematical advantages, this formulation also provides a natural way to *measure* $f(z)$ and $h(z)$ in terms of experimental data for only $z(t)$ and $\dot{z}(t)$,

without specific assumptions for $f(z)$ and $h(z)$. Subtracting any two different trajectories, with different K_0's which are not necessarily close, $K_i(z) = K_p(K_{i0} + \phi)$ and $K_j(z) = K_p(K_{j0} + \phi)$, yields:

$$\frac{K_i(z) - K_j(z)}{K_{i0} - K_{j0}} \equiv K_p(z) = e^{-\int_0^z \frac{2h(z')dz'}{m}}, \tag{5.10}$$

which gives,

$$h(z) = -\frac{d}{dz}\left[\frac{m}{2}\log K_p(z)\right]. \tag{5.11}$$

To avoid numerical differentiation, we also use $\int h(z)dz$ in our discussion below.

Since the kinetic energy goes to zero when the intruder stops, we can set equation (5.2) equal to zero at $z = z_{stop}$, i.e., $K_0 = -\phi(z_{stop})$. The expression for $f(z)$ follows by then differentiating with respect to z_{stop}, which yields:

$$f(z_{stop}) = K_p(z_{stop})\left(\frac{dK_0}{dz_{stop}}\right) + mg. \tag{5.12}$$

This analysis requires a determination of K_p (i.e. $h(z)$ is determined), and $z_{stop}(K_0)$. Obtaining the relation for $z_{stop}(K_0)$ is generally straightforward, particularly since it requires no dynamical data (only the initial energy and final resting depth). However, note that $z_{stop}(K_0)$ is undefined for stopping depths smaller than z_{stop} for $K_0 = 0$. For this reason, it may be useful to combine this approach with the approach described in Chapter 3, especially to measure $f(z)$ for small z.

5.2 Application to Experimental Data

To demonstrate this approach, we use experimental data from our low Mach number photoelastic impact experiments discussed in the previous two chapters, using bronze intruders which strike a collection of approximately 25,000 PSM-1 photoelastic disks. This section includes the circular intruders discussed in the last two chapters, but

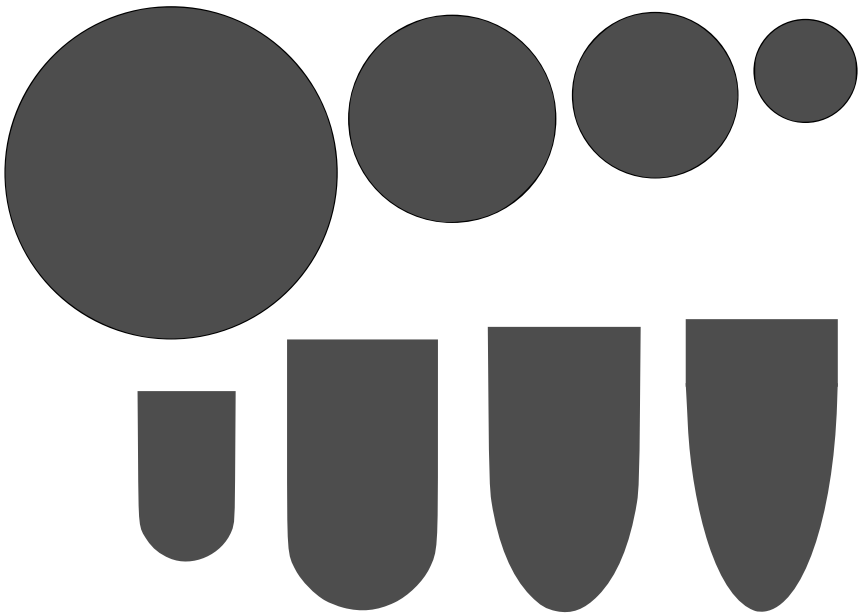

FIGURE 5.1: Shapes of all intruders, drawn to scale, as described in the text.

also includes ogive intruders with an elliptical nose and a rectangular tail (shown in Fig. 5.1). In this chapter, we focus on the intruder dynamics only, neglecting the photoelastic response.

Data is shown for eight different intruders, with width D and varying nose shape, as shown in Fig. 5.1. Data for four circular intruders are used, with diameters, D, of 6.35, 10.16, 12.70, and 20.32 cm, along with four ogive intruders. This allows measurement of $f(z)$ and $h(z)$ for various sizes and shapes; the next chapter presents a more focused treatment of size and shape effects. The ogives consist of a continuous piece of material, where the leading part is a half-ellipse truncated along the minor axis, with semi-major axis a and semi-minor axis $b = D/2$, terminated by a rectangular tail of length L. Three different ellipses were used, with $a/b = 1$ (half-circle), $a/b = 2$, and $a/b = 3$. The width of the ogives was held constant, $D = 9.3$ cm, and L was varied to keep the intruder mass constant ($L = b = 4.15$ cm for $a/b = 3$ case, longer for other ogives). By keeping the width and mass constant, shape effects

are isolated. Additionally, we used one smaller ogive with $a/b = 1$, $b = 3$ cm, and $L = 7.7$ cm.

Trajectories are calculated as described previously, by locating the intruder at each frame, then using discrete differentiation with filtering to calculate the velocity. Using equation (5.10), and averaging over all pairs of trajectories (omitting trajectory pairs with very similar initial velocities), we obtain a clear average value for $K_p(z)$, and thus for $h(z)$, as shown in Fig. 5.2.

Data for $-\frac{m}{2}\log K_p = \int h(z)dz$ are approximately linear in z, which is consistent with a constant drag coefficient, $h(z) = b$. Taking a derivative with respect to z gives the collisional term $h(z)$ (shown in Fig. 5.2), which scales approximately with the intruder size. Here, calculating $h(z)$ requires taking a spatial derivative, which amplifies the fluctuations in $K_p(z)$. Essentially, we avoided taking a discrete time derivative at the front end of the analysis by using only position and velocity, not acceleration. Instead, we take a spatial derivative at the end of the analysis. However, especially when comparing data from multiple intruders, this allows better separation of the fluctuations from systematic variation in the functional form of $h(z)$.

The collisional term, $h(z)$, consists of an initial transient regime, after which $h(z)$ approaches a nearly constant value, which we denote as h_0. For blunt intruders, like circles, the collisional term is stronger right at impact. This may be surprising, since the area of impact is smallest then. This effect probably stems from the difference in the motion of the particles near the intruder nose immediately after impact compared to later on in the trajectory. During initial impact, the particles in front of the intruder are stationary, and the bulk of the material must be accelerated from rest. This is more difficult than maintaining the flow during the bulk of the trajectory. For intruders with more elongated noses, this effect is greatly weakened, and even reversed in the $a/b = 3$ case shown in Fig. 5.2. We also note that the nature of

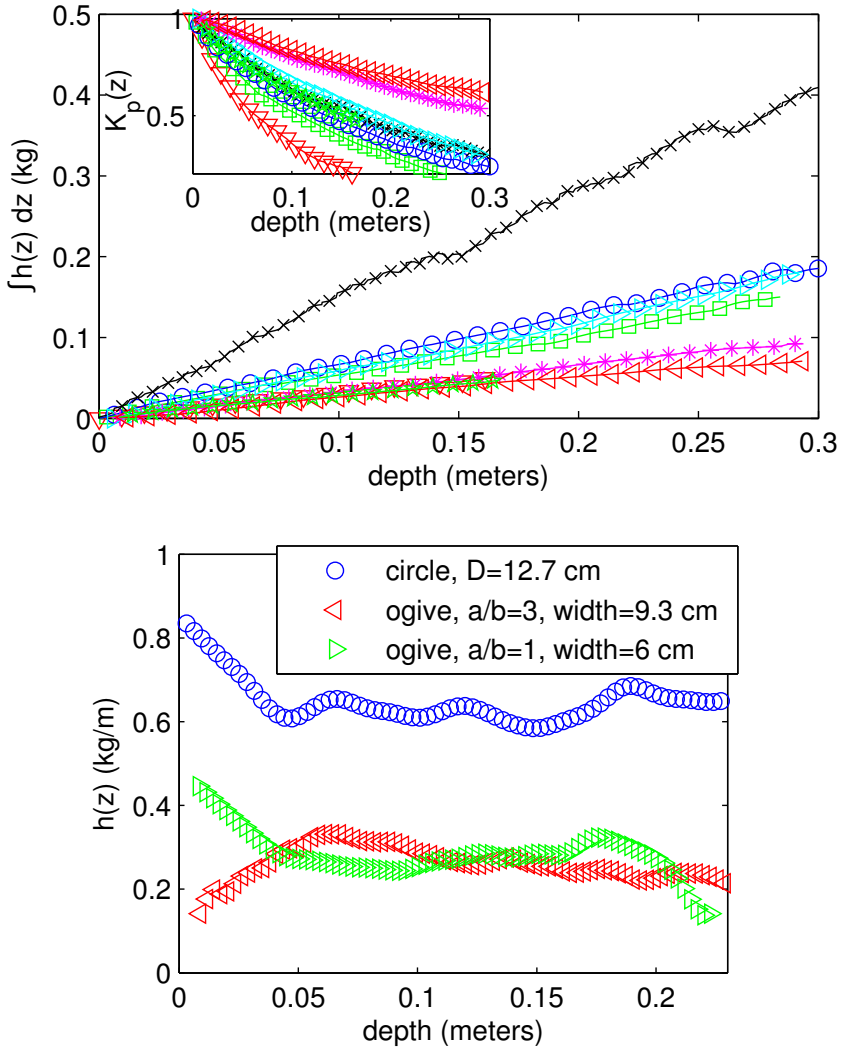

FIGURE 5.2: Top panel shows a plot of $\int h(z)dz = -(m/2)\log K_p$ for all eight intruders. All are approximately linear, and the local slope gives the value of $h(z)$. Inset shows $K_p(z) = \Delta K(z)/\Delta K_0$, computed for all pairs of trajectories, i and j, with a minimum $\Delta K_0 = K_{i0} - K_{j0}$. Bottom panel shows $h(z)$ taking the local derivative. This shows transient behavior, which depends on the shape of the intruder. All circular-nosed intruders show stronger $h(z)$ near the surface, reminiscent of similar effects in fluid impacts (Greenhow and Yanbao, 1987; Miloh, 1991; Mouchacca et al., 1996). For the ogive with $a/b = 3$, this effect is reversed: $h(z)$ starts lower and increases sharply to a local maximum, then weakly decreases.

$h(z)$—constant, after an initial transient—supports the form of the force law used here (equations (1.8) and (5.1), particularly the omission of a force law term which is linear in the velocity (i.e., proportional to $K^{1/2}$), at least for the experiments discussed here.

Once $h(z)$ is specified, equation (5.12) provides a solution for $f(z)$ with adequate data for $z_{stop}(K_0)$. First, we plot the final depth, z_{stop}, versus K_0, as shown in Fig. 5.3. Note that the data for the higher energies are consistent with the logarithmic behavior in equation (5.9), and that the data for low energies deviate from this curve with a non-zero intercept which scales with intruder diameter ($z_{stop}(K_0 = 0) \approx D$). Only circular intruders are used in this calculation, since ogive intruders penetrate much deeper and interact with the lower boundary of the experiment, so a curve for $z_{stop}(K_0)$ is difficult to obtain.

Finally, by fitting a smooth function to the curve for each circular intruder and differentiating, we solve for $f(z)$, wherever $z_{stop}(K_0)$ is defined. This yields a linear function for all circular intruders with a non-zero intercept, f_0, which scales linearly with the intruder mass (Fig. 5.3), i.e., $f_0 \simeq 1.35\,mg$. We note that impact experiments performed by Goldman and Umbanhowar (2008) show a similar result for f_0, but with f_0 which increases from 0 to $2mg$ during $0 < z < D$, then saturates at $f_0 \simeq 2mg$. Due to the limitations on using this method for finding $f(z)$, a combination of the two approaches—using kinetic energy for $h(z)$ and using acceleration versus velocity squared for $f(z)$—will be used for the data presented in future chapters.

As discussed previously, the net force must go to zero as the intruder stops. With this in mind, we examine trajectories for $v < 0.3$ m/s (shown in Fig. 5.4), where $h(z)v^2 \ll mg$. This shows approximately constant deceleration as the intruder comes to a stop (consistent with the expected value of $f(z)$ from Fig. 5.3), and the acceleration jumps to zero at $v = 0$, as in (Goldman and Umbanhowar, 2008;

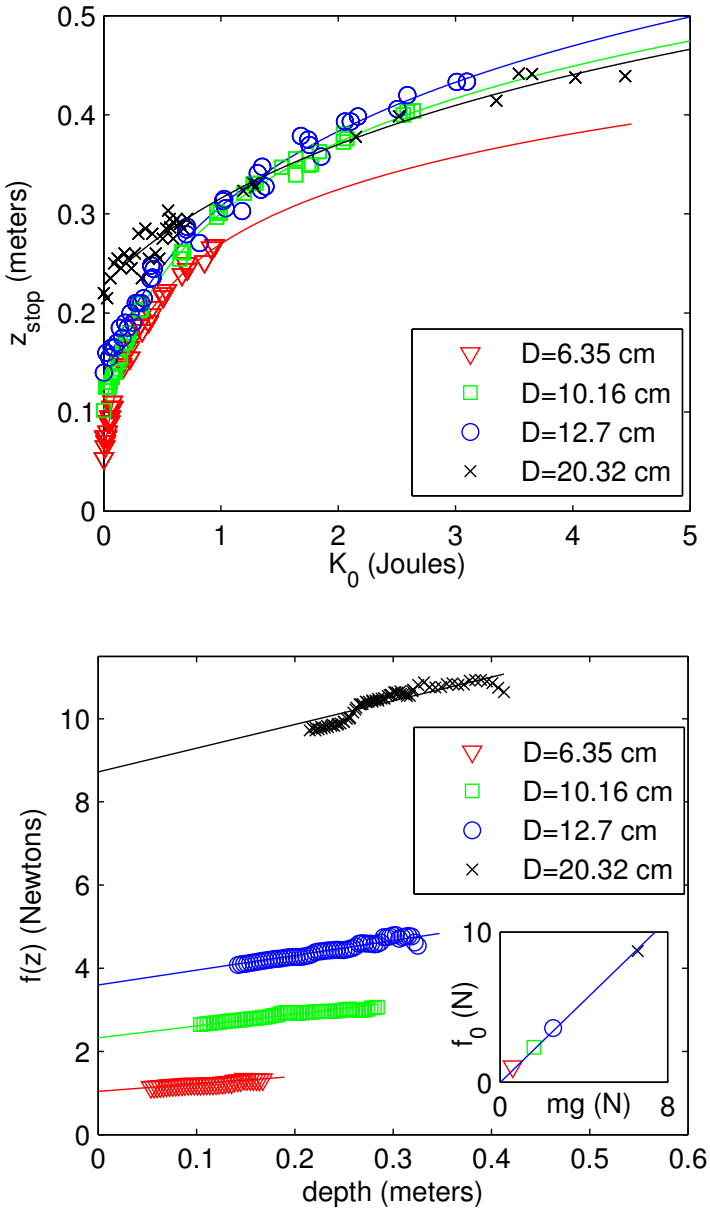

FIGURE 5.3: The top panel shows a plot of z_{stop} vs. K_0, with fits of the form $a\log(bK_0+1)+c$. The bottom panel shows a plot of $f(z)$ for circular intruders. Linear fits are f_0+kz, where the slope, k, corresponds to hydrostatic pressure. Note that $f(z)$ is dominated by the offset, f_0, for our data. Inset shows plot of f_0 vs. mg, with a linear fit through the origin, with slope 1.35.

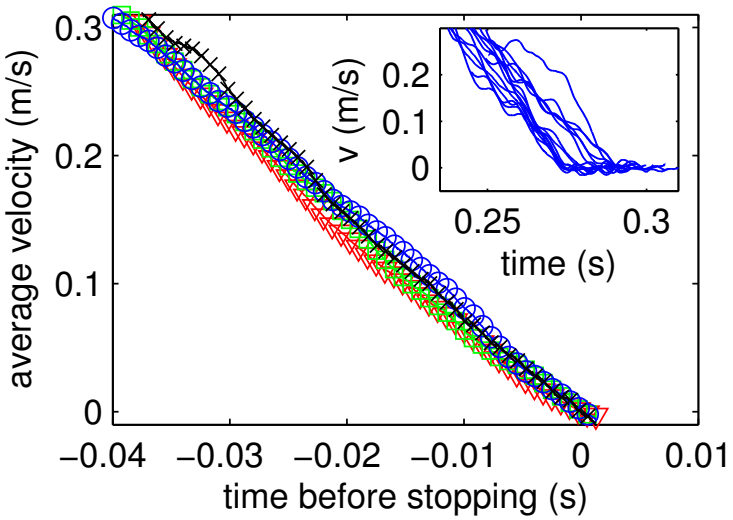

FIGURE 5.4: Main plot shows the average velocity of all four circular intruders (same colors and symbols as Fig. 5.3) as they come to a stop. All intruders decelerate at the same rate, $a \approx 0.75g$. The upward force required would be approximately $1.75mg$, which is consistent with $f(z_{stop}) = 1.35mg + kz_{stop}$, from Fig. 5.3. Inset shows the end of all trajectories, with initial velocities between 1 and 6 m/s, for the $D = 12.7$ cm circular intruder. Note that the stopping time is very weakly dependent on initial velocity, since these trajectories all end at approximately the same time.

Umbanhowar and Goldman, 2010).

As stated previously, the fact that $h(z)$ is relatively constant (h_0) after a small transient near the initial surface supports the form chosen for the force-law model. The steady-state drag coefficient h_0 is different for various shapes, as shown in Fig. 5.5. The top plot shows that h_0 is directly proportional to the intruder diameter for circular-nosed intruders. The bottom plot shows h_0 versus the aspect ratio of the elliptical nose, which falls off substantially as aspect ratio is increased. Thus, for equal intruder widths, a more elongated nose has a substantial effect in decreasing the collisional force. Understanding the shape dependence of the h_0 is the focus of the next chapter.

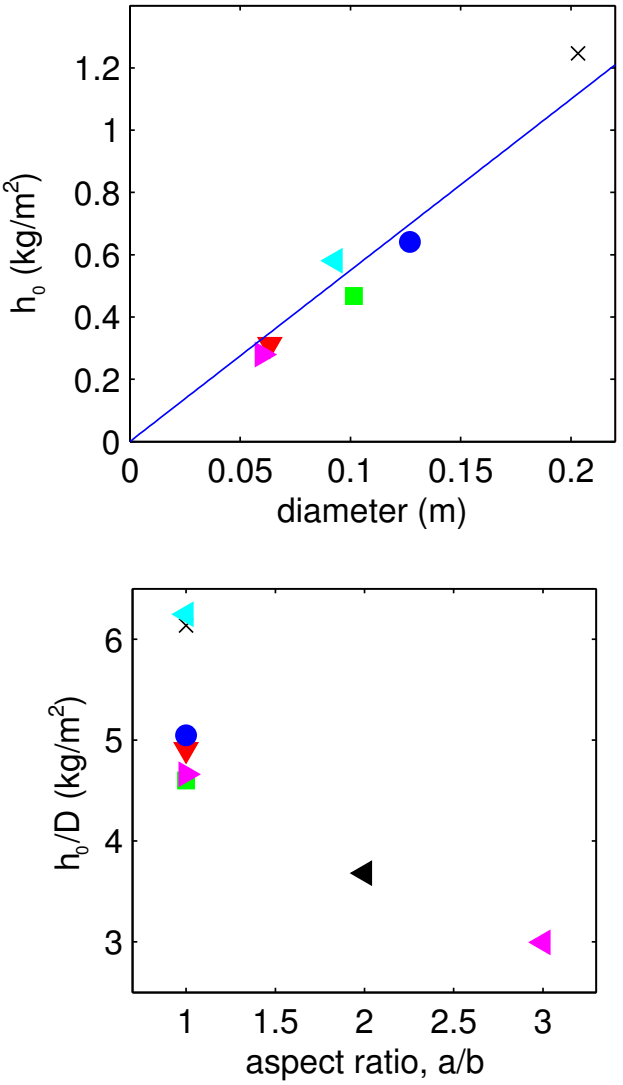

FIGURE 5.5: Top panel contains a plot of h_0 for circular-nosed intruders versus the diameter of the nose, D, which shows that the two are directly proportional, with $h_0 \sim 5.5D$. Bottom panel contains a plot of h_0/D versus the intruder aspect ratio, a/b, which shows a substantial decrease in the collisional force as the intruder nose is elongated.

5.3 Summary

This chapter has focused on a new approach to a commonly used model for describing the dynamics of an intruder impacting on a granular material. By reformulating the model into a linear ODE, we obtain formal solutions of the trajectory in terms of the initial kinetic energy, as well as a systematic way of calculating the different terms in the model—namely $f(z)$ and $h(z)$—using only position and velocity data, which are more easily obtained experimentally than data for acceleration.

Additionally, we have shown how this approach can be used to measure $f(z)$ and $h(z)$ for experimental data. The high level of agreement between the experimental data and the model in equation (1.8), as well as the sensible behavior of the $f(z)$ and $h(z)$ terms, validate the use of the model. Particularly, our data shows no need to implement terms linear in velocity which have been proposed (Goldman and Umbanhowar, 2008). We also observe that the usual assumption that $h(z)$ is constant applies only after an initial transient at impact, which appears to vary with intruder size and shape (Fig. 5.2). Understanding this dependence, with the goal of understanding microscopic origins of this term, is the focus of the next chapter.

6

Shape Dependence: A Collisional Model

The results discussed thus far can be summarized in two main ideas. First, we have constructed a new physical picture for granular impact at the scale of individual grains, where the force on the intruder is dominated by intermittent collisions with force-chain-like structures within the material, and this energy is carried away acoustically and dissipated. Second, we have observed that the impact dynamics are also well captured by a macroscopic force law, Eq. (1.8). Thus, while previous studies have successfully used macroscopic force laws, they lacked the grain-scale picture which is needed to understand the origins of the force law terms. However, based on the results from previous chapters, we now have such a picture to aid in connecting the force law terms to microscopic physics.

The velocity-squared term, $h(z)\dot{z}^2$, is typically understood as an inertial term, which models dynamic momentum (and energy) transfer from the intruder to the particles. Previous chapters have shown that, although the slow or average dynamics are well captured by Eq. (1.8), the force is not smooth on faster time scales. Rather, the force is spatio-temporally highly fluctuating due to intermittent emission of acoustic energy along relatively long-lived granular networks which are excited

locally along the intruder-granular interface. In the previous chapter, we also saw that changes in intruder shape had a strong effect on $h(z)$. It is this effect that will be pursued here by constructing a collisional model which gives a velocity-squared drag force which explicitly involves the intruder shape.

Specifically, in this chapter, I will present a comprehensive study of the dynamics of intruders with triangular noses of varying shape but constant mass and width, including the deceleration and rotation of the intruder. These data augment earlier results from previous chapters for circular and ogive intruders. We fit the dynamics of deceleration to the force law in Eq. (1.8), and thereby measure $f(z)$ and $h(z)$ for varying intruder shape. To understand the shape dependence of $h(z)$ and the dynamics of the rotations, we propose a mesoscopic collisional model, where the intruder is decelerated through random, repeated collisions with "clusters" of grains. These clusters are force-chain-like networks which are acoustically excited as in Fig. 6.1. This collisional model contains a velocity-squared drag force, $h(z)\dot{z}^2$, which depends on the intruder size and shape in a way that incorporates the interactions of the intruder with these structures. The drag force includes one fit parameter for the material properties and an extra term to account for sharp tips, which are common to the $h(z)$ coefficient for all intruders. Once these are determined, the model can easily be tested by using a variety of intruder shapes. Using this approach, we find good agreement between the experimental data and the model for the velocity-dependent drag force. Additionally, we show that the collisional model captures the rotational dynamics of the triangular-nosed intruders, which become more striking as the length of the intruder nose increases. The rotational dynamics are captured with no additional parameters: the parameters from the drag coefficient are used as inputs to the rotational dynamics.

The key feature for the inertial term of the model is momentum transfer to clusters of grains, based on collisions between clusters and the intruder. These collisions are

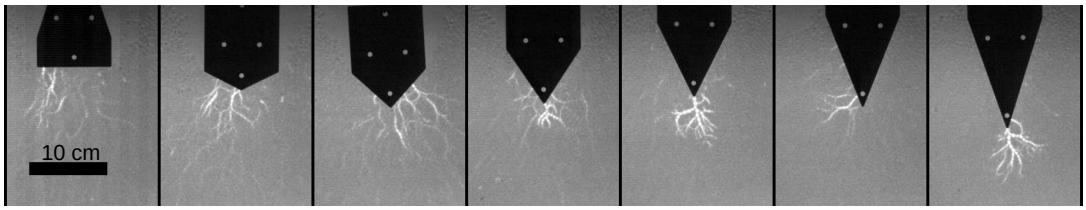

FIGURE 6.1: Still frames showing each of the seven triangular-nosed intruders (described in the text) with leading edge slopes of $s = 0$ to $s = 3$ in increments of 0.5, from left to right. These images are chosen during times when the intruders have collided with and excited networks. It is the networks that form the clusters of particles discussed in the model. Here, grains that are carrying an instantaneously large force appear bright. Note that the force networks or force chains are oriented roughly normally to the intruder surface at the intruder-granular interface. Additionally, the collisions shown for the s =1.5, 2, and 3 intruders occur at the intruder tip, which illustrates the large forces that occur there when s is large.

affected by the local shape and speed of the intruder at the collision point. Analysis shows that the tip of each triangular intruder (which is slightly rounded to avoid breaking particles) yields a disproportionately large collisional effect, compared to other parts of the intruder. By adding the tip contribution to the rest of the shape-dependent contribution, we will see that the collisional model captures the velocity-squared drag for all intruders.

Although the focus of this chapter is on understanding the collisional term, which dominates the stopping process, the static term, $f(z)$, in Eq. (1.8) is also of interest. The cross sectional area and mass of the intruder are fixed for the triangular-nosed intruders, both of which affect $f(z)$ as shown in the previous chapter. We then observe that even large variation in shape, at fixed width and mass, does not substantially affect $f(z)$, which fully characterizes (heuristically) the static term for the present experiment. Concerning the grain-scale origins of $f(z)$, a recent study (Brzinski

et al., 2013) suggested this term was due to static, depth-dependent friction, and had a strong dependence on intruder shape, especially while the intruder nose was only partially submerged. Understanding how $f(z)$ depends on intruder shape should also give insight into the grain-scale processes which control it. Brzinski, et al. (Brzinski et al., 2013) placed intruders of various shapes (spheres, cylinders, and cones) at various depths in a granular bed. They then measured for each depth the maximum force which the granular material could support before failing. Additionally, they imposed a controlled airflow through the grains to alter the the strength of hydrostatic pressure via gravitational loading. They focused on the regime *before* the intruder nose was fully submerged. In this regime, they found shape dependence which is consistent with a static, depth-dependent pressure which points normally inward at each grain-intruder contact, where the static pressure is a direct result of hydrostatic loading from the grains above. Once the intruder nose was fully submerged, they found the same static force for all intruders with the same cross-sectional area ($f(z) = kz$, where $k \sim \pi R^2$), with a small correction for the nose shape. They then inferred that this force is indeed the static term in dynamic experiments, $f(z)$, by measuring the final penetration depth versus drop height for spheres and cylinders. They found that these results were consistent with their previous measurements of the static force. In our experiments, which focus on the regime after the nose is submerged, we observe that even large variation in shape (at fixed intruder width) does not substantially affect the static force term, $f(z)$, a result which is consistent with the findings of Brzinski, et al. as well as other slow-drag studies (Albert et al., 2001; Goldsmith et al., 2013). Also, our measurements, as well as measurements by Goldman and Umbanhowar (Goldman and Umbanhowar, 2008), show a substantial offset term once the nose is fully submerged, $f(z) = f_0 + kz$, where f_0 scales with the intruder mass.

The outline of the remainder of this chapter is as follows. I will first present the

details of the collisional model, including predictions for the drag force and torque, which will be referenced throughout the remainder of the chapter. Next, I will discuss some data processing techniques which are specific to these experiments and present the data for the intruder trajectories (including depth, velocity, deceleration, and rotations, as well as $f(z)$ and $h(z)$ for each intruder). I will then compare the experimental results to the predictions of the collisional model for the velocity-squared drag force and rotational dynamics. Figs. 6.8 and 6.11 are the culmination of this analysis.

6.1 Collisional Model

6.1.1 Assumptions

The basis of the collisional model proposed here is that the intruder transfers momentum to the granular material through a sequence of random collisions that excite the force network, as in Fig. 6.1. As we have seen over the past several chapters, the intruder deceleration is dominated by interactions with filamentary networks of grains (force chains) that carried relatively large forces. As the intruder pushed through the granular bed, acoustic pulses generated near the intruder-granular interface, propagated along these strong force networks, carrying momentum and energy away from the intruder. I will refer to the grains in one of the networks as a cluster. But, these clusters have a filamentary quasi-1D structure and are not usually collections of grains in a simple (e.g. roughly circular) 2D region.

Typically, these force networks are oriented roughly perpendicular to the local intruder boundary. Thus, collisions transfer momentum into the intruder at a set of point-like contacts, such that the momentum carried along the network is normal to the local surface (at least initially). Figure 6.1 shows typical photoelastic images for each intruder, which demonstrate this feature. Each frame is chosen during a collision with a grain cluster. Since we cannot resolve particles, a definitive estimate

cannot be made of the number of particles involved in each one of these clusters. As a way to estimate the cluster size, we divide the total number of bright pixels beneath the intruder (1.5 intruder radii from the bottom edge of a circular intruder) by the total number of bright pixels within one particle diameter from the bottom edge of the intruder, using only image frames where at least one particle (about 50 pixels) is bright at the intruder edge. A pixel is denoted "bright" if it is a fixed amount brighter than the background intensity. The threshold is chosen as 10% greater than the background intensity, which conforms well with what one identifies as "bright" by eye. Figure 6.2 shows a histogram of this measurement from a single trajectory using a circular intruder, which shows an average cluster size of about ten particles.

Thus, the following features will be used as inputs to the model: random collisions with quasi-particles of a constant average mass, where the subsequent momentum transfer is locally normal at each point along the granular-intruder interface (i.e., grain-intruder friction is unimportant). A simplified version of this process can then be constructed in order to calculate the force acting on the intruder. As in Fig. 6.3, I will consider an object with mass m, profile specified by $C(x)$, and width W, moving at a velocity v, undergoing repeated inelastic collisions with small, stationary objects. Here, these small objects are grain "clusters", in the above sense, which we take to have mass m_c. We expect that m_c is greater than the mass of a single grain, since a collision involves force-chain-like structures that remain in contact over a finite time. In Fig. 6.3, the clusters are now represented as mesoscopic "particles". A related collisional picture was proposed by Takehara, et al. (Takehara et al., 2010). In their study, an intruder was subjected to constant-velocity drag through a granular medium, and the drag force was measured with a high-speed force sensor. The drag force was measured to be quadratic in velocity, and, based on momentum-transfer considerations as well as images of the motion of the grains, Takehara and colleagues argued that it is the result of repeated collisions with particle clusters which are larger

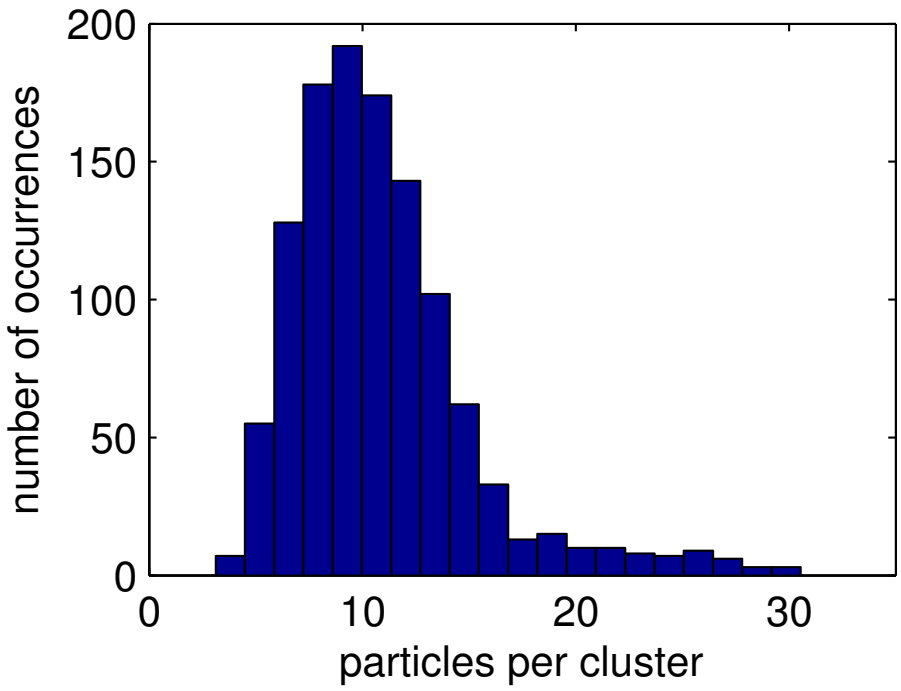

FIGURE 6.2: Histogram showing the average cluster size, which we estimate by dividing the total number of bright pixels within 1.5 intruder radii of the bottom edge of a circular intruder (although the measurement is insensitive to the size of the region used) by the number of bright pixels within one particle diameter of the intruder nose. The above plot was obtained from a single trajectory using a circular intruder, and the plot only includes frames where at least 50 pixels are bright at the intruder edge, to make sure that the intruder is in contact with a particle cluster. This result is typical for all trajectories.

than the mass of a single grain. Although they could not visualize grain scale forces, they nevertheless concluded that "the formation of the dynamical force chains plays a crucial role." Our approach is similar, but, photoelasticity allows us to directly verify the role of the granular network and relate it to the collisional properties of our intruders. It is also interesting that the speeds used by Takehara et al. were

roughly an order of magnitude smaller than the fastest impact speeds shown here. This means that the collisional forces are important over a surprisingly large range of intruder speeds.

We next assume that the clusters behave as quasi-particles which collide inelastically with the surface of the intruder. We assume collisions in the direction of the surface normal, $\hat{n}$, that are inelastic and captured (in that direction) by a restitution coefficient, e. Momentum in the direction parallel to the intruder interface is unaffected by the collision. A collision imparts momentum $\Delta\vec{p} = \hat{n}(1+e)\frac{m_c m}{m_c+m} v\cos\phi$, where ϕ is the angle between the velocity and $\hat{n}$. We take the typical collision time to be $\Delta t = \gamma d/(v\cos\phi)$, where d is the particle diameter and γ is an $O(1)$ constant. Thus, the average force at a particular location along the intruder surface is in the $\hat{n}$-direction, given by:

$$\vec{f} = \frac{\Delta\vec{p}}{\Delta t} = \frac{(1+e)v^2\cos^2\phi}{\gamma d}\left(\frac{m_c m}{m_c+m}\right)\hat{n}. \tag{6.1}$$

Note that, since the bronze intruders we use are much more dense than the photoelastic material used for particles, the reduced mass in our case is approximately equal to the mass of a cluster, $\frac{m_c m}{m_c+m} \approx m_c$. We assume that collisions are equally likely per unit normal area. Thus, the relative number of collisions in a length of intruder surface dl is $dn = \beta dl/d$ (where β is another $O(1)$ parameter), so $d\vec{F} = \hat{n} f\, dn = (\hat{n} f\beta/d)dl$. If the shape of the intruder is given by $z = C(x)$, as in Fig. 6.3, then $dl = (1+C'^2)^{1/2}dx$, and $\cos\phi = (1+C'^2)^{-1/2}$.

This force is quadratic in the velocity and depends on the local shape of the intruder surface, varying as $\cos^2\phi$. By integrating this force over the intruder surface, we can obtain a specific prediction about the effect of intruder shape on the v^2 term, effectively giving $h(z)$, in terms of a shape factor, multiplied by an $O(1)$ multiplicative term that is the same for all intruders, regardless of shape, for a given bed material.

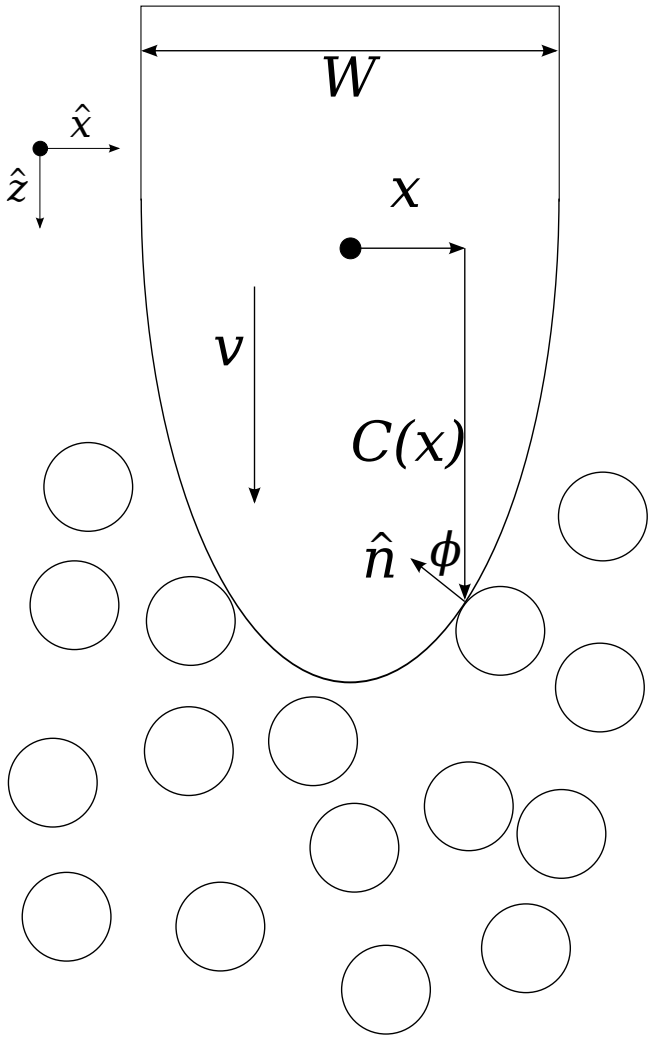

FIGURE 6.3: Sketch of the collisional model, where an intruder of width W randomly collides with grain clusters (represented by the open circles) as it moves at velocity v. The collisions occur along the "nose", i.e. the leading edge of the intruder, at positions $\vec{r} = x\hat{x} + C(x)\hat{z}$ measured from the center of mass. These collisions involve momentum transfer normally into the intruder, along normal vector $\hat{n}$.

Note too, that, although the real grain clusters near the surface of the intruder are also moving, their velocity relative to the intruder should scale with the intruder

velocity, so this analysis should still hold up to a constant scale factor of order unity. This point will be discussed in the next chapter on particle flow fields.

6.1.2 Upward Force

We first consider only vertically upward (z-component) of $d\vec{F}$ by integrating over the leading edge of the intruder and keeping only the z-component:

$$\begin{aligned} F_z &= \int d\vec{F} \cdot \hat{z} \\ &= \frac{(1+e)\beta m_c m}{\gamma d^2 (m_c + m)} \left[\int_{-W/2}^{W/2} dx (1 + C'^2)^{-1} \right] v^2 \\ &= B_0 \cdot I[C(x)] \cdot v^2. \end{aligned} \tag{6.2}$$

The constant $B_0 = \frac{(1+e)\beta m_c m}{\gamma d^2 (m_c+m)}$ contains various system parameters which are nominally the same for all intruders. The size and shape effects are contained in $I[C(x)]$, defined as:

$$I[C(x)] \equiv \int_{-W/2}^{W/2} dx (1 + C'^2)^{-1}. \tag{6.3}$$

For example, $I = W$, the width of the intruder, if $C' = 0$, corresponding to an intruder with a flat interface. This model considers only the collisional part of the drag force, and gives no prediction about the shape effects for the $f(z)$ term. However, the $f(z)$ term tends to be important only as the intruder is coming to rest. Later, in our discussion of rotations, we return to this issue, showing that $> 80\%$ of the trajectory (in terms of distance) is dominated by the velocity-squared drag force.

In this chapter, we will particularly focus on intruders with triangular noses, intended as two-dimensional "cones" as in (Newhall and Durian, 2003), which have a constant slope, $|C'(x)| = s$, everywhere except at the tip. This yields a very simple form for $I[C(x)]$, which allows a straightforward method to separate shape from

other effects:

$$I(s) = \frac{W}{1+s^2}. \tag{6.4}$$

The constant slope for conical intruders allows us to unambiguously focus on the directional effects assumed in the collisional model. Additionally, moderate variation in s—here, we use seven triangular-nosed intruders, with slope s varying between 0 and 3, in increments of 0.5—gives an order of magnitude change in $I(s)$ (i.e., $I(s=0) = W$ and $I(s=3) = W/10$). This provides a sensitive test of the collisional model.

We also include data for the collisional drag coefficient measured for circular- and elliptical-nosed intruders, as discussed in the previous chapter. For circular or elliptical noses, $I[C(x)]$ has the following form:

$$I(a,b) = \frac{2b}{\left(\frac{a}{b}\right)^2 - 1}\left(\frac{\left(\frac{a}{b}\right)^2 \arctan\sqrt{\left(\frac{a}{b}\right)^2 - 1}}{\sqrt{\left(\frac{a}{b}\right)^2 - 1}} - 1\right), \tag{6.5}$$

where a and b are the semi-major and semi-minor axes, respectively (The limit for a circular nose, $a = b = R$, is well defined, specifically $I(R) = 4R/3$.)

6.1.3 Rotation and Torques

Experiments show that intruders can rotate as they move through the granular medium, a phenomenon which has not been studied previously. If a symmetric intruder is tilted at an angle θ from vertical, the forces on either side are generally different from what they would be if the intruder were vertically oriented. Most importantly, the forces are not the same on either side of the intruder, which is particularly evident for triangular noses, where the intruder-cluster collision angles clearly differ from side to side. Such a tilt has several consequences. First, the vertical force may differ from the corresponding value when the intruder is vertical;

second, there can be a horizontal component of the force; and third, there may be a non-zero torque on the intruder. It is possible to correct for the effect of rotations on the vertical force by recalculating I based on a $C(x)$ that includes the instantaneous θ for the intruder (i.e. calculate $C(x,\theta)$), and use this in the computation of I. Note that the vertical force, which is determined by I, must have an extremum at $\theta = 0$, since the force must be invariant to whether θ is positive or negative. The horizontal force and the torque are not subject to the same symmetry principle, so a small tilt will lead to values of these quantities that are $O(\theta)$. In the present experiments, the corrections to the vertical force and the relative magnitude of the horizontal force are small compared to the unperturbed part of the vertical force.

However, the same is not generally true for the torque. Particularly in the late stages of the dynamics, we observe substantial rotations for some intruders. Thus, the torque on an intruder at an angle θ must be calculated in a method similar to Eq. (6.2). This yields quantitative predictions for the dynamics of rotation, including the prediction of rotational instability. The total torque, $\vec{\tau}$, about the center of mass of the intruder is given by integrating $\vec{r} \times \vec{f}$ over all collisions over the intruder surface, similar to Eq. (6.2):

$$\begin{aligned} \vec{\tau} &= \int \vec{r} \times \vec{f}\, \frac{\beta}{d} dl \\ &= B_0 v^2 \int \vec{r} \times \hat{n} \cos^2\phi \, dl \end{aligned} \tag{6.6}$$

Here, $\vec{r} = x\hat{x} + C(x,\theta)\hat{z}$, $\hat{n} = -\sin\phi\hat{x} - \cos\phi\hat{z}$, and $\sin\phi = -C'(1+C'^2)^{-1/2}$, with $dl = (1+C'^2)^{1/2}dx$ and $\cos\phi = (1+C'^2)^{-1/2}$, as before (see the sketch in Fig. 6.3). This yields:

$$\begin{aligned} \vec{\tau} &= B_0 v^2 \int dx \left(\frac{CC'}{1+C'^2} + \frac{x}{1+C'^2} \right) \hat{y} \\ &= B_0 J[C(x,\theta)] v^2 \hat{y}. \end{aligned} \tag{6.7}$$

6.1.4 Tip Effects

A last issue concerns the concentration of stress at the tip of the triangular intruders, particularly the more pointed ones. By examining the photoelastic response near the intruder, we can separate the relative contributions from collisions with the tip and collisions elsewhere on the smooth intruder surface. The tip is quite small, with a radius of curvature that is a fraction of a particle radius. It is still possible to calculate a shape factor for the tip, $I[C_{tip}(x)]$, where $C_{tip}(x)$ is the shape of the rounded tip. However, this analysis is misleading, because the probability of a collision at the tip is far greater than elsewhere on the smooth surface of the intruder. By analyzing the photoelastic response near the tip, and in other regions, as shown in the top of Fig. 6.4, we find that the tip contribution to the velocity-squared force is approximately the same for intruders with prominent tips (i.e., large s), but it is considerably larger per unit area, by about an order of magnitude, than contributions from collisions away from the tip. The term due to collisions with the tip must be included separately in the force and torque calculations for accurate prediction of the velocity-squared drag and off-axis rotations.

Since the collisional model is based on spatially averaged random collisions, we expect it to break down as the spatial scale of the intruder (i.e., the size of the tip) approaches the system's microscopic length scale (i.e., the size of a particle). A flat (or gently curved) section of the intruder undergoes collisions with excited force networks with probability which grows proportionately to its area. However, a small tip is able to contact individual particles and excite a force network with some finite number of particles, despite its small size. Thus, we expect a sharp tip to be more efficient per unit area than a gently curved section.

6.2 Experimental Techniques

6.2.1 Experimental Apparatus

The experimental apparatus is the same as in previous chapters, again using the hardest particles (PSM-1). The triangular-nosed intruders discussed in this chapter are comprised of a downward-pointing isosceles triangle, symmetric about the vertical axis, with opening angle 2α, attached to a rectangular tail of the same width as the base of the triangle, $W = 9.65$ cm. The noses of these intruders are clearly evident in Fig. 6.1. The length of the tail is varied to keep the total area, $A = 0.0107$ m^2, and hence, mass, $m = 0.219$ kg, constant for different opening angles of the nose (for reference, the $s = 3$ intruder has a tail which is 3.81 cm long). Thus, the intruder nose has a constant magnitude slope $s = \tan^{-1}\alpha$, except at the tip, which is rounded with a radius of about 1.5 mm. Note that this is smaller than the particle radii, which are 2.1 mm and 3 mm. The $s = 3$ intruder is turned upside-down and used as the $s = 0$ intruder.

6.2.2 Data Processing

As before, we use distinguishing features of the intruder to locate its center of mass at each frame relative to the initial point of impact. Discrete differentiation yields data for position, velocity, and acceleration. Using these data for many different trajectories with varying initial velocities, we fit to a force-law model such as Eq. (1.8). We use the kinetic-energy approach for $h(z)$, as in Chapter 5, and we use fits with velocity and acceleration data to measure $f(z)$, as in Chapter 3 (specifically, figure 3.6).

Additionally, we make use of the photoelastic response on the particles near the intruder, as discussed in Chapters 3 and 4. By calibrating G^2 as a measure of the force along a particular section of the intruder, we can separate the force on different

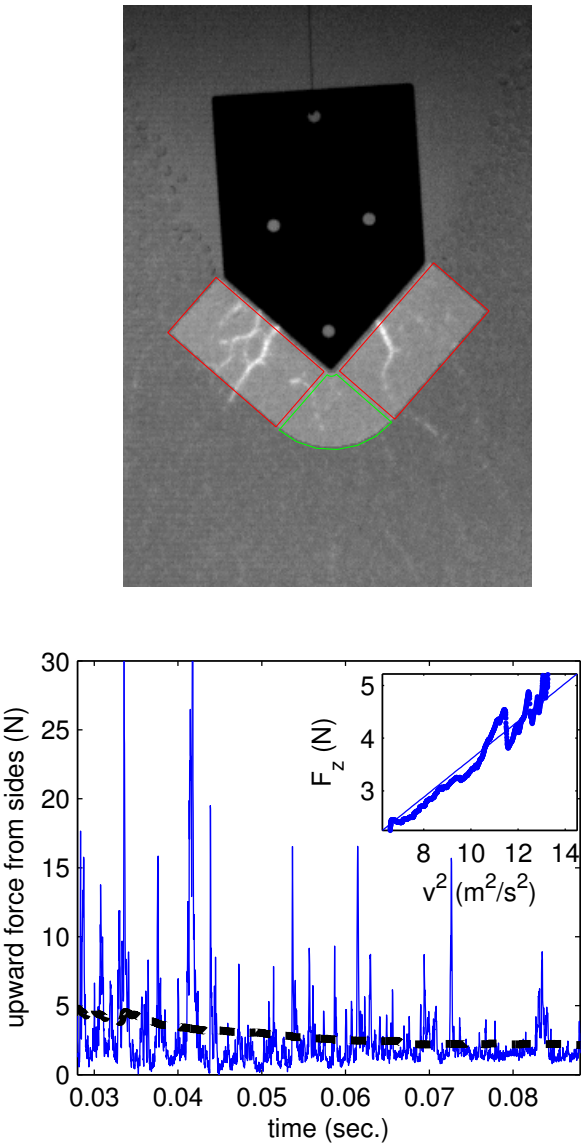

FIGURE 6.4: Top panel contains a photoelastic image showing the different regions used to measure the force contributions from the sides (outlined in red) and from the tip (outlined in green) of the triangular-nosed intruders. Bottom panel shows a plot of the calibrated photoelastic force on the sides of the $s = 1$ intruder, for a single trajectory with $v_0 \approx 3.8$, both at each frame (thin, blue line) and after a low-pass filter (thick, black, dashed line). Inset shows the low-pass filtered force signal (determined photoelastically) versus v^2, where the imposed fit passes through the origin with a slope of 0.36, which is the effective drag coefficient contribution from the sides of the triangular intruder in this case.

sections of the intruder, specifically the sides and beneath the tip, as shown in the top panel of Fig. 6.4. By calibrating G^2 per pixel to the measured local pressure, we can evaluate the force on a given section of the intruder nose, which we assume points normally inward. This is supported by the direction of the force chains, which point roughly normally out of the edge of the intruder nose. The various components of this force determine the stopping force, the torque, etc. We also assume that the collisional drag from the tip of triangular-nosed intruders points straight upward. Finally, by applying a low-pass filter to the strongly fluctuating time series for F_z, and correlating with v^2 for large velocities ($v > 2.5$ m/s) where collisional drag dominates, we measure the collisional drag for that section of the intruder nose. (We will show that this measurement agrees well with the measurement of the drag coefficient from tracking the intruder, which is measured using all velocities, so we believe that using only fast velocities, with $v > 2.5$ m/s, has no effect on determination of the drag coefficient using the photoelastic response.) This process is shown in Fig. 6.4, and it is repeated for approximately ten trajectories per intruder. The results are then averaged to determine the mean collisional drag from each region (sides and tip) of each intruder.

6.3 Comparison of Model to Experimental Data

Figs. 6.5 and 6.6 show typical impact trajectories for intruders with triangular noses. Figure 6.5 shows three trajectories for intruders with $s = 0.5, 1.5, 2.5$, impacting with similar initial velocities, $v_0 \approx 3.55$ m/s. We show several different quantities: the depth below the point of initial contact, the downward velocity, the horizontal velocity, the acceleration, and the angular orientation of the intruder, with $t = 0$ corresponding to initial impact. Increasing s leads to deeper penetration for the same initial impact velocity, but the stopping time remains about the same (Figure 6.6). Additionally, increasing s corresponds to a weakening of the initial deceleration at

impact, which is manifest in the form of $h(z)$ for different shapes, as discussed later. The fluctuations in the acceleration correspond to fluctuations observed in the photoelastic response, as shown in Chapter 3; the particular range of fluctuation frequencies is set by the cutoff frequency of the low-pass filter used to reduce noise that is introduced by numerical differentiation of data for the intruder's location.

Note that the angular rotations for large s can be substantial, such as in the trajectory from the $s = 1.5$ intruder shown in Fig. 6.5, and that there is no preferred direction of rotation. This suggests an instability to small perturbations for the angular orientation of the intruder. The typical intruder horizontal velocity is quite small compared to the vertical velocity, so the assumption that the velocity is purely vertical is reasonable.

We now seek to understand shape-dependence of all intruder trajectories, particularly in terms of the collisional model, as discussed above. We do this in two parts. First, we consider the depth, velocity, and acceleration, and fit these data to the force-law model from Eq. (1.8). By combining this analysis with the photoelastic analysis, we show that, modulo an overall normalization factor, the collisional model gives an accurate prediction of the velocity-squared drag force felt by the intruder. In particular, by choosing a reasonable value for the normalization, we find that the shape effect on $h(z)$ is accounted for. Second, we examine the rotational dynamics, and show that the collisional model also gives an accurate prediction of these dynamics as well.

6.3.1 Force Law Analysis

We first measure $f(z)$ and $h(z)$ for each intruder by using the depth, velocity, and acceleration data for all trajectories. We then ask how these functions, shown in Fig. 6.7, are affected by the intruder shape, focusing particularly on the triangular intruders. The static force term, $f(z)$, shown in the top panel of Fig. 6.7, is essentially

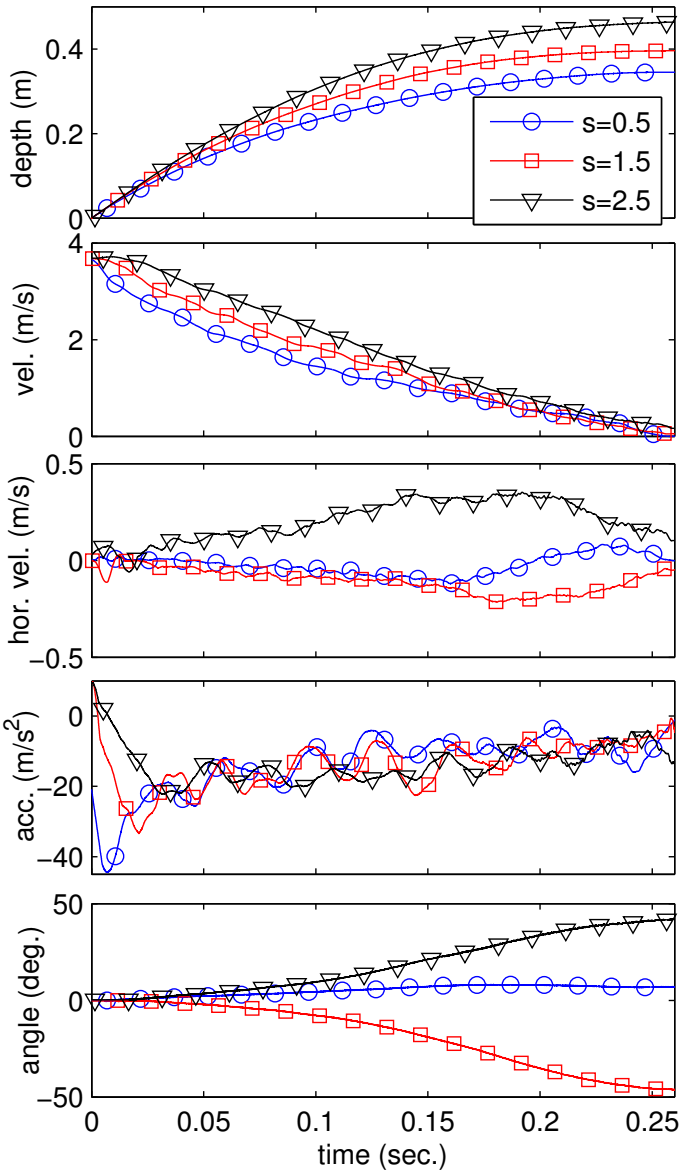

FIGURE 6.5: Plots versus time of three individual intruder trajectories and related information ($s = 0.5, 1.5, 2.5$) with $v_0 \approx 3.55$ m/s, including depth, downward velocity, horizontal velocity, acceleration, and angular orientation of the intruder, with initial impact at $t = 0$. Many such trajectories are used to fit to the force law in Eq. (1.8).

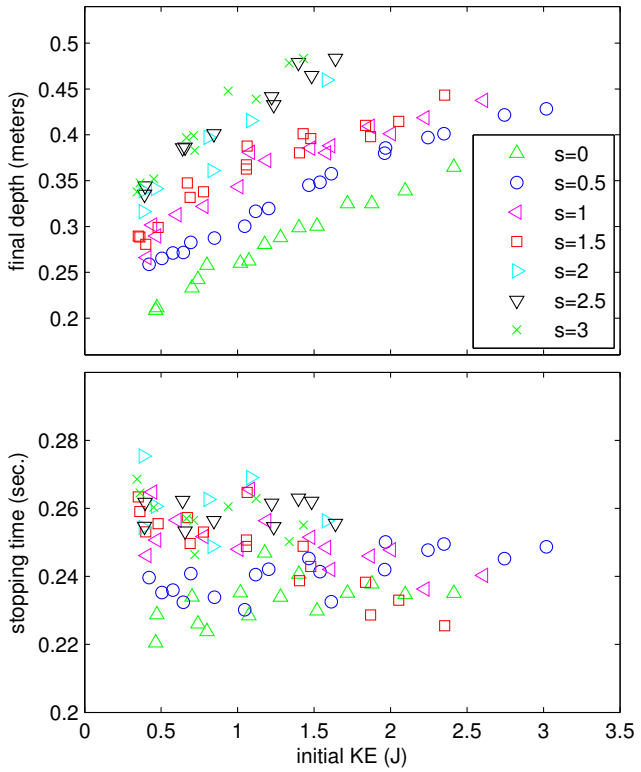

FIGURE 6.6: Plots of final depths (top panel) and stopping times (bottom panel) for all intruders as a function of the kinetic energy at impact. Note that increasing s leads to deeper penetration, but virtually no change in stopping time.

insensitive to intruder shape, within the scatter of the data. In this figure, different colors distinguish the various intruders. Note that the width of these intruders is constant, while effects on $f(z)$ from increasing intruder size were treated in the previous chapter. By contrast, the collisional term, $h(z)$, shows significant dependence on shape (bottom panel). This term exhibits an initial transient, followed by roughly steady-state behavior. We define h_0 to be this steady-state value of $h(z)$ after the initial transient. More elongated intruder noses (i.e., larger s) are associated with decreasing h_0. The transition from the initial transient to $h(z)$ approximately equal to h_0 corresponds roughly to the time at which the nose penetrates the granular material, and presumably to the formation of a steady-state velocity field around the

intruder, as discussed in the next chapter. The transient behavior also depends on the shape, where blunt-nosed intruders ($s < 1$) have $h(z = 0) > h_0$, and elongated-nosed intruders ($s \geq 1$) have $h(z = 0) < h_0$. Additionally, as discussed previously, we also measure h_0 using the calibrated photoelastic response starting after the nose is fully submerged. This allows us to examine the contributions made by different pieces of the intruder nose (i.e., the sides or the tip of the triangular nose).

Figure 6.8 shows a summary of the behavior of the velocity-squared drag coefficient, h_0, and its dependence on shape for different intruders, as well as a comparison to the collisional model predictions in Eqs. (6.3) and (6.4). Specifically, the top of Fig. 6.8 shows results for triangular-nosed intruders that demonstrate the two methods of calculating the total collisional drag coefficient: from the intruder trajectories (open, red circles) and using the photoelastic response (red dots). These two very different approaches are in good agreement with each other. Using the photoelastic data, shown in Fig. 6.4, we decompose these drag coefficients into contributions from the sides (open, black squares), which matches well to the predictions for the collisional stresses with the flat surfaces of the triangular-nose intruders dependence (solid, black line), and contributions from the tip (blue crosses). These latter data asymptotically approach a constant value as the aspect ratio is increased from $s = 0$ to $s = 3$ (i.e., as the tip is made more prominent), which we capture with an approximate fit of $h_{tip} \approx 0.2(1 - e^{-2s})$. Considering the tip as a small flat section with a width of 3 mm, its contribution for large s is approximately 10 times bigger than what occurs for a comparable area on the flat part of the intruders. The large contribution from the tip is clear by inspection of the photoelastic videos, which show a surprisingly large amount of acoustic pulses emanating from the intruder tip. (The examples shown in Fig. 6.1 are representative of this). In this regard, we note that the model is based on an assumption of locally smooth surfaces such that the flux of clusters impinging on the surface is a coarse-grained measure. At the tip,

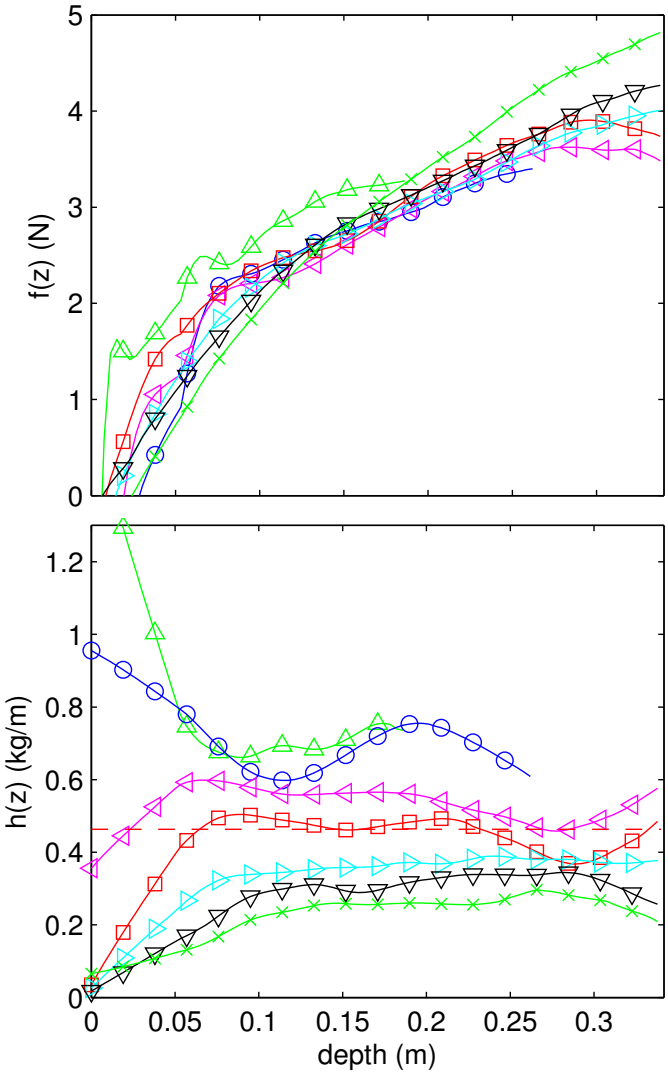

FIGURE 6.7: Plots of $f(z)$ (top panel) and $h(z)$ (bottom panel) versus depth for each of the seven triangular-nosed intruders, measured from the intruder dynamics ($s = 0$ to $s = 3$ are denoted in order by $\triangle$, $\circ$, $\triangleleft$, $\square$, $\triangleright$, $\triangledown$, $\times$, as in Fig. 6.6). Note that $f(z)$ shows almost no dependence on intruder shape, and $h(z)$ is relatively constant, denoted h_0, after an initial transient which is larger or smaller depending on the shape of the intruder nose. The red dashed line shows h_0 for $s = 1.5$.

this assumption is violated, implying that the tip needs to be treated on a separate footing.

In the bottom panel of Fig. 6.8, we plot h_0 versus $I[C(x)]$, also including data

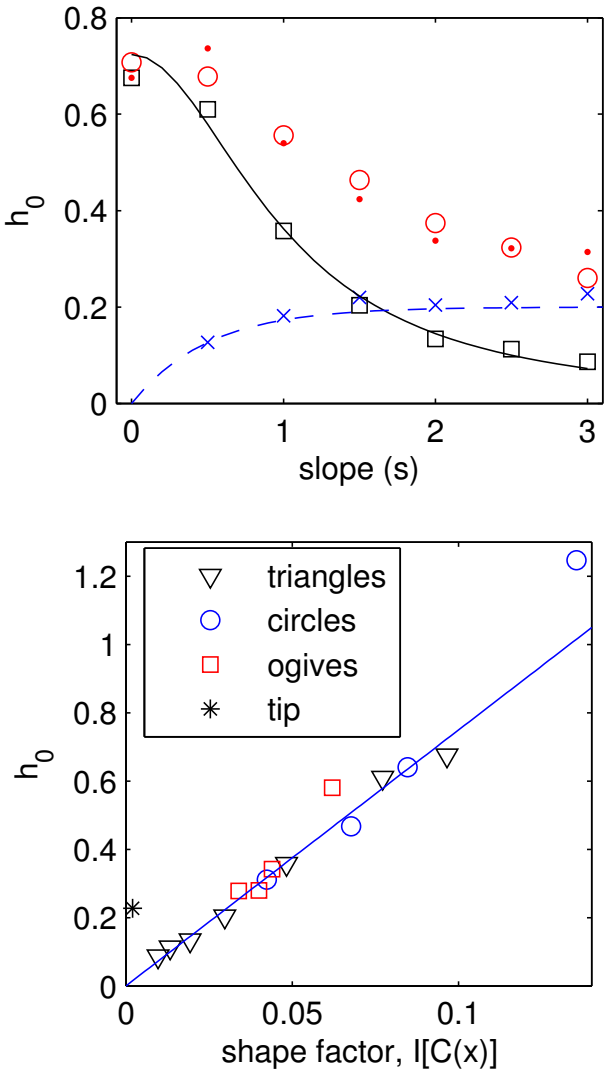

FIGURE 6.8: Plot of h_0 (top panel) measured from the trajectory (open red circles) and force measurements inferred from the photoelastic response (red dots). The latter is also decomposed into contributions from the sides (black squares) and the tip (blue crosses). The fit line for the tip contribution (dashed, blue line) is given by $0.2(1 - e^{-2s})$. The contribution from the sides matches extremely well to the model (solid black line), $I(s) = W(1 + s^2)^{-1}$, from Eq. (6.4). Bottom panel shows a plot of h_0 versus $I[C(x)]$ for all intruders. The solid line shows a linear fit through the origin, where the slope is $B_0 \approx 7.6$. The h_0 value for triangular noses is the photoelastic measurement from the sides (excluding the tip), while the asymptotic value (~ 0.2 N) for the tip measurement is shown separately (black asterisk).

for circular- and elliptical-nosed intruders from the previous chapter. Since intruders with circular or elliptical noses are smooth (i.e., have no small tips), we use the value of h_0 extracted from the trajectories. In this figure, we have also plotted separately the contributions from the sides and from the tip of triangular-nosed intruders. There is a good linear collapse of all the data, except perhaps the heaviest circular-nosed intruder. The successful linear collapse of h_0, measured from experimental data, versus $I[C(x)]$, calculated from the theory, is a strong confirmation of the collisional model and is the first main result of this chapter. This implies that $B_0 = h_0/I[C(x)]$, which contains the microscopic details for collisions, is relatively constant for all intruders used.

6.3.2 Rotational Dynamics

Thus far, the collisional model has provided a good description of the vertical force on the intruder. We now examine the intruder rotations in the context of the collisional model, as in Eqs. (6.6) and (6.7). An image of an intruder which is rotated by an angle θ is shown in Fig. 6.9.

For the symmetric intruders used here,when $\theta = 0$, the integral $J[C(x,\theta)]$ is equal to zero (since x and C' are both odd functions in x, and everything else is even). However, as noted earlier, for $\theta \neq 0$, the integral in Eq. (6.7) is non-zero. To first order in θ, we can write:

$$J[C(x,\theta)] = J_1\theta + O(\theta^2), \tag{6.8}$$

where $J_1 > 0$ corresponds to intruders which are unstable to small perturbations in their angular orientation. Writing an equation for torque about the center of mass for small angles, and setting it equal to the moment of inertia, I_{mom}, times the angular acceleration, $\ddot{\theta}$, yields:

$$\ddot{\theta} = \frac{\tau}{I_{mom}} \approx \frac{B_0 J_1}{I_{mom}} v^2\theta = \Gamma v^2\theta, \tag{6.9}$$

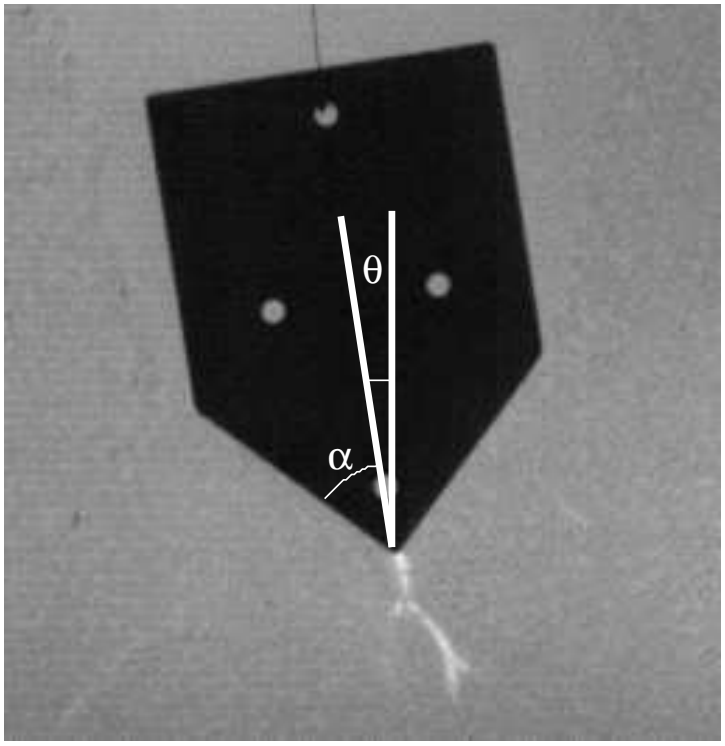

FIGURE 6.9: Image of a triangular-nosed intruder ($s = 1$) which has rotated by an angle θ.

where, $\Gamma \equiv \frac{B_0 J_1}{I_{mom}}$.

Testing this relation in this form requires $\ddot{\theta}$ and v^2. However, as discussed in the previous chapters, the numerical computation of each time derivative of θ obtained from experiment amplifies the measurement noise. However, examination of the angular trajectories, vs. z indicates approximately exponential growth: $\theta(z) \approx \theta_0 e^{\lambda z}$, as shown in Fig. 6.10. Thus, instead of directly testing Eq. (6.9), the data suggest that analyzing the angular orientation as a function of depth, $\theta(z)$ might be a useful approach. To facilitate such analysis, we use product and chain rules, along with the

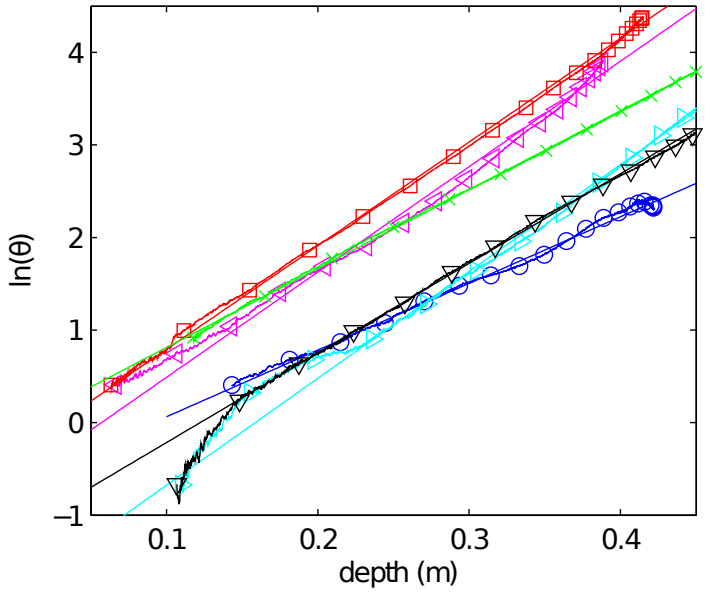

FIGURE 6.10: Plot of the natural log of the angular deviation versus depth from single trajectories, where all angular deviations are considered positive. The straight lines suggest exponential growth for θ vs. depth; the slope on the semi-log plot corresponds to the exponential growth rate, λ_+, as discussed in the text. Different colors and symbols denote different intruders, with the same designations as in Figs. 6.6 and 6.7.

decelerating force from Eq. (1.8), to write:

$$\begin{aligned} \ddot{\theta} &= v^2 \frac{d^2\theta}{dz^2} + \frac{dv}{dt}\frac{d\theta}{dz} \\ &= v^2 \frac{d^2\theta}{dz^2} + \left(g - \frac{f(z)}{m} - \frac{h(z)}{m} v^2 \right) \frac{d\theta}{dz} \end{aligned} \tag{6.10}$$

Combining this result with Eq. (6.9) yields:

$$\frac{d^2\theta}{dz^2} - \left(\frac{h(z)}{m} \right) \frac{d\theta}{dz} - \Gamma\theta = \frac{1}{v^2} \left(\frac{f(z)}{m} - g \right) \frac{d\theta}{dz}. \tag{6.11}$$

In the large-velocity regime (i.e., where the velocity-squared force dominates), the right-hand side of this equation is small, and, if $h(z)$ is constant, this equation

can be easily solved. Examining Figs. 6.5 and 6.7, we see that $f(z) \approx mg = 2.15$ N for much of the trajectory (recall, the intruder mass is 0.219 kg), and right side is further reduced for large velocities by $1/v^2$. Hence, for the moment, we assume that the right side of Eq. (6.11) is negligible (we return later to the validity of this approximation). Replacing $h(z)$ with h_0, we obtain:

$$\theta(z) = \theta_{0+} e^{\lambda_+ z} + \theta_{0-} e^{\lambda_- z}, \tag{6.12}$$

where $\theta_{0\pm}$ are constants of integration, and

$$\lambda_\pm = \frac{h_0}{2m} \pm \sqrt{\left(\frac{h_0}{2m}\right)^2 + \Gamma} \tag{6.13}$$

For $\Gamma > -\left(\frac{h_0}{2m}\right)^2$, the $\lambda_\pm$ are purely real, with $\lambda_+ > 0$ and $\lambda_- < 0$. In this case, the collisional model predicts exponential growth in depth of the angle of rotation, with a growth rate $\lambda_+ = \frac{h_0}{2m} + \sqrt{\left(\frac{h_0}{2m}\right)^2 + \Gamma}$. The quantities $J[C(x,\theta)]$ and I_{mom}, which yield Γ, are straightforward to calculate from the intruder geometry, and h_0 is already calculated for the intruders used here (Figs. 6.7 and 6.8).

As noted, plots of the natural log of the angle versus depth follow approximately straight lines, where the slope corresponds to λ_+ (Fig. 6.10). Leftward and rightward rotation are both plotted as positive. We measure the slope of these lines for all trajectories which break symmetry sufficiently (i.e., have at least 3000 data points where $\theta > 10°$) and which have initial velocities $v_0 > 3.5$ m/s. (This ensures that the right-hand side of Eq. (6.11) is small for the bulk of the trajectory). The resulting data for $\theta(z)$ show reasonable reproducibility for each shape and initial velocity, and clear variations from one shape to another (bottom panel of Fig. 6.11). Note that no $s = 0$ trajectories are plotted, as they do not show sufficient rotation. Moreover, rotational stability of the $s = 0$ intruder is expected, since $J_1 < 0$ (top panel of Fig. 6.11). For instance, when $J_1 < 0$, a small perturbation of θ from zero will lead

to behavior in time that will be roughly oscillatory. For instance, if we freeze v^2, the resulting equation of motion $\ddot{\theta}$ is oscillatory. However, when $J_1 > 0$, the dynamics are predicted to be saddle-like.

To compare these predictions to the experimental data, we calculate λ_+ for the triangular intruders according to Eqs. (6.6)-(6.13). Fig. 6.12 is intended as a visual aid for the following discussion, as it depicts the geometrical quantities used in this calculation. We break the integral for $J[C(x,\theta)]$ into two sections for the left and right sides. We replace the terms involving C' with terms involving α (the intruder nose angle) and θ; specifically, $(1+C'^2)^{-1/2} = \sin(\alpha \pm \theta)$ and $C'(1+C'^2)^{-1/2} = \cos(\alpha \pm \theta)$. This simplifies the calculation, yielding the torques for the left and right sides,

$$\begin{aligned} |\vec{\tau}_l| &= B_0 v^2 W_l \times \\ &\quad \left[\bar{C}_l \sin(\alpha+\theta)\cos(\alpha+\theta) - \bar{x}_l \sin^2(\alpha+\theta)\right] \qquad (6.14) \\ |\vec{\tau}_r| &= B_0 v^2 W_r \times \\ &\quad \left[\bar{C}_r \sin(\alpha-\theta)\cos(\alpha-\theta) - \bar{x}_r \sin^2(\alpha-\theta)\right] \qquad (6.15) \end{aligned}$$

where the total torque in Eqs. (6.6) and (6.7) is then given by the difference between these two expressions. Here, z_{cm} is the distance from the nose-tail boundary to the center of mass as shown in Fig. 6.12. Positive z_{cm} is into the triangular nose, negative z_{cm} is into the rectangular tail, $W_{l,r} = \frac{W}{2}\sqrt{s^2+1}\sin(\alpha \pm \theta)$ are the horizontal projections of the left and right sides of the triangular nose, and $\bar{C}_{l,r} = (\frac{sW}{4} - z_{cm})\cos\theta \pm \frac{W}{4}\sin\theta$ and $\bar{x}_{l,r} = \frac{W}{4}\cos\theta \mp (\frac{sW}{4} - z_{cm})\sin\theta$ are the strictly positive vertical and horizontal distances, respectively, from the center of mass to the midpoint of the sides of the triangular nose. The expressions for z_{cm} and I_{mom} are functions of area, A, mass, m, and width, W, although we hold these quantities constant, as well as

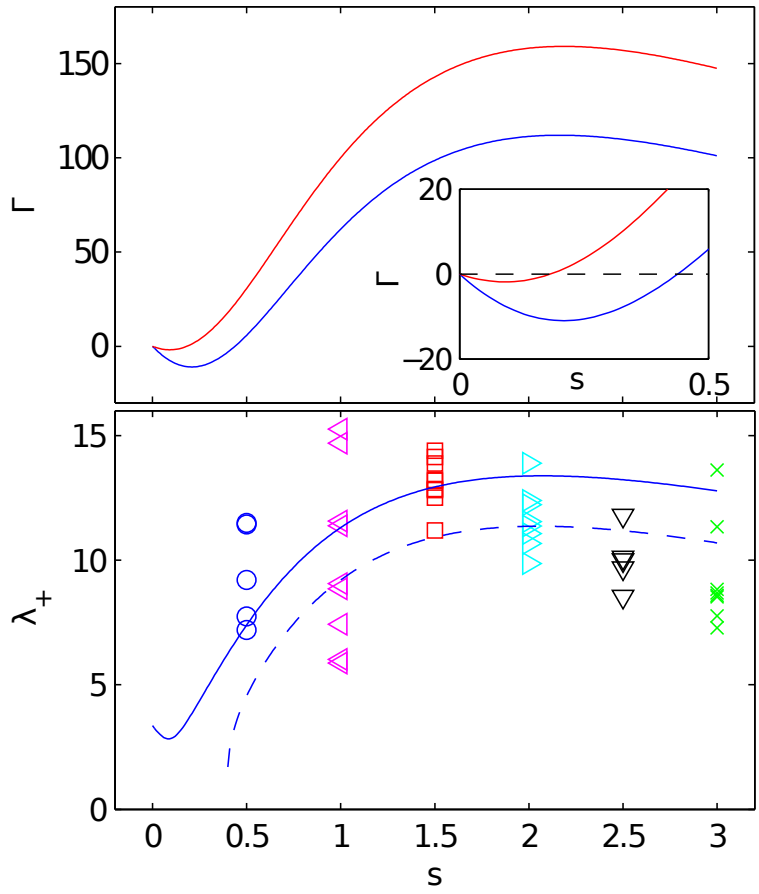

FIGURE 6.11: Top panel shows a plot of Γ, calculated from Eq. (6.20) and preceding equations, with (red, upper curve) and without (blue, lower curve) the tip contribution included. As discussed in the text, $\Gamma > 0$ corresponds to a rotational instability, which occurs at $s \approx 0.2$ with the tip included and $s \approx 0.4$ without the tip included. Thus, $s = 0$ intruders should be stable, and all other intruders should be unstable, which is consistent with data presented here. Bottom panel shows a plot of all measured values of λ_+ versus the aspect ratio, s. Each data point represents a trajectory with sufficient angular deviation (i.e., it has at least 3000 data points where $\theta > 10°$), where wee measure the growth rate as shown by the linear fits imposed on each trajectory in Fig. 6.10. Also plotted is the prediction for λ_+ from Eqs. (6.13) and (6.20) with (solid line) and without (dashed line) the contribution from the intruder tip.

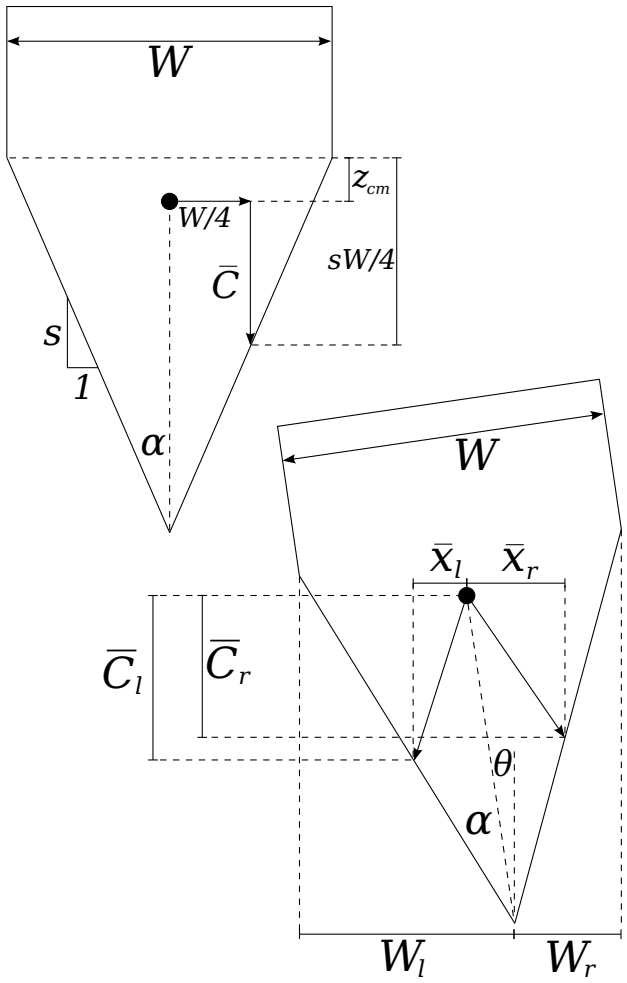

FIGURE 6.12: A sketch of a triangular-nosed intruder which depicts the various quantities used in calculating the torque. See the text for details.

functions of the nose aspect ratio, s which we vary in these experiments:

$$z_{cm} = \frac{s^2 W^3}{96A} + \frac{sW}{4} - \frac{A}{2W} \tag{6.16}$$

$$I_{mom} = \left(\frac{A^3}{12W^2} + \frac{AW^2}{12}\right) - s\left(\frac{W^4}{96}\right) + s^2\left(\frac{AW^2}{96}\right) - s^4\left(\frac{W^6}{9216A}\right) \tag{6.17}$$

The contribution from the tip must also be included, since the force there can be substantial, e.g. Fig. 6.8. We model the tip force, F_t, according to the dashed fit line in Fig. 6.8, given by:

$$F_t(s) \approx 0.2\left(1 - e^{-2s}\right) v^2 \tag{6.18}$$

We assume this force always acts in the $-\hat{z}$-direction, which allows a calculation of the torque from the tip, $\vec{\tau}_t$:

$$|\vec{\tau}_t| = F_t\left(\tfrac{sW}{2} - z_{cm}\right)\sin\theta \tag{6.19}$$

Finally, we obtain:

$$\Gamma = \lim_{\theta\to 0}\frac{1}{\theta}\left(\frac{|\vec{\tau}_l| + |\vec{\tau}_t| - |\vec{\tau}_r|}{v^2 I_{tot}}\right), \tag{6.20}$$

where we consider the small θ limit.

The top panel of Fig. 6.11 shows a plot of Γ versus aspect ratio, with (red line) and without (blue line) the contribution from the tip included. Recall from Eqs. (6.8) and (6.9) that $\Gamma > 0$ corresponds to a rotational instability. Thus, with or without the tip contribution included, the instability occurs between $s = 0$ and $s = 0.5$, which is consistent with the experimental data, as no $s = 0$ intruders show substantial rotations. The value for Γ is then used to calculate λ_+ according to Eq. (6.13). Note also that there are *no free parameters* here, since the values of $B_0 \approx 7.6$ Ns^2/m and F_t, given by Eq. (6.18), are inputs from the collisional drag measurements shown in Fig. 6.7. The model prediction for λ_+ is in good agreement with the experimental results, as shown in the bottom panel of Fig. 6.11. The dashed line shows the prediction without the tip contribution, while the solid line includes the tip. This constitutes the second main result of this chapter.

Concerning the scatter in the data for measured values of λ_+, we suggest several possible explanations. First, we neglected the right-hand side of Eq. (6.11). In practice, this term is associated with a velocity- and depth-dependent correction to

λ_+ through the coefficient in front of $\frac{d\theta}{dz}$. The strength of this correction depends on the velocity and depth at which the bulk of the rotation occurs. However, Fig. 6.13 shows that the error introduced into λ_+ is small for approximately 80-90% of the trajectory. Thus, the data for exponential fits in Fig. 6.10 are primarily in the regime where the approximation made here is valid. Second, the collisional process which is responsible for rotations is stochastic (in time, in space, and in magnitude). Thus, we expect some fluctuations, especially when considering a single trajectory. Previous chapters have shown that the deceleration is highly fluctuating for individual trajectories, but for long times and many trajectories, it approaches the average behavior. Third, we assumed that the force from the tip always pointed directly upwards, but a horizontal component of the tip force could have a strong effect, particularly given the relatively large distance from the center of mass to the tip. Fourth, we assumed that the collisions were *equally likely* everywhere over the intruder surface. If this assumption is not strictly true, it would not substantially affect the velocity-squared drag, but it could have a stronger affect on the torque. However, on average, the collisional model captures the overall behavior of exponential growth, as well as the magnitude and scaling of the growth rate with intruder shape.

6.4 Conclusions

In this chapter, I have presented data for the dynamics of triangular-nosed intruders impinging on a granular bed from above, which can be summarized as follows. The average dynamics are captured well by a macroscopic force law, Eq. (1.8), and the magnitude of the velocity-squared drag force, $h(z)$, depends strongly on intruder shape, while the static term, $f(z)$, shows very little dependence on intruder shape. Additionally, intruder rotations become increasingly significant as the intruder nose is elongated, and that in such cases, the angle of the intruder grows approximately exponentially in depth, $\theta(z) \sim e^{\lambda_+ z}$.

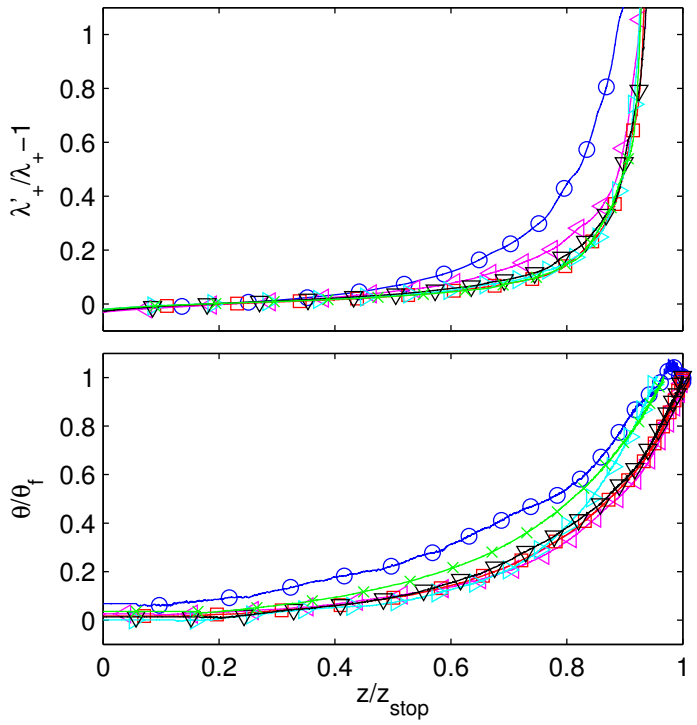

FIGURE 6.13: Top panel shows the error in the growth rate, λ_+, plotted versus the normalized depth for the intruder trajectories shown in Fig. 6.10. We calculate this error by including the neglected term on the right-hand side of Eq. (6.9), using the instantaneous velocity and depth, which yields λ'_+. We divide this by λ_+ and subtract 1, yielding the error made by the approximation (0 corresponds to no error, and 1 corresponds to an error of the same size as λ_+). As the intruder slows down, the approximation is no longer valid, but this does not occur until very late in the trajectory, at approximately 80-90% of the final depth, z_{stop}. Bottom panel shows a plot of the angle versus depth, where the angle and depth are both normalized by their final values. In terms of total rotation angle, a substantial amount of rotation (roughly 40% of the total rotation) happens at the end of the trajectory, after the error in λ_+ begins to grow substantially. However, plotted on a semi-log scale, as in Fig. 6.10, the bulk of the dynamics are clearly exponential in depth, with a well defined growth rate.

Additionally, I have discussed a collisional model for the velocity-squared drag on an intruder moving through a granular medium, and I have used experimental data to test this model. The key component in the model is momentum transfer from the

intruder to the grains. By focusing on intruders with triangular noses, we are able to systematically explore the effect of intruder shape on the collision process. We observe experimentally that momentum transfer per unit surface length is larger at the tip than elsewhere along the sides of the intruders. By modeling the collision process in terms of both tip and side contributions, we observe excellent agreement with both the intruder deceleration and angular orientation. The agreement between these two *linearly independent* measurements of the mesoscopic collisional theory serves as an additional confirmation of the basic assumptions, which are as follows. The velocity squared drag and angular rotations:

1. are dominated by intermittent, generally inelastic, collisions;
2. collisions involve grain clusters which can be modeled by as having a fixed (mean) mass;
3. collisions occur with equal probability throughout the granular material;
4. momentum transfer acts normally inward at the site of collision on the intruder surface;
5. there is a disproportionately larger contribution from collisions occuring at the tip of the intruder when s is large.

There are several important aspects to the physics that underlie the model. First, the momentum transfer acts normally at the point of collision, which essentially says that friction between the grains and intruder is not important in this process (Seguin et al., 2009). The shape factors, $I[C(x)]$ and $J[C(x,\theta)]$, were derived under this assumption, which is verified by the agreement with experimental data (shown in Figs. 6.8 and 6.11). We note that this is simply for the collisional term, which controls the velocity-squared drag and the corresponding off-axis rotations. Another point

is that there is a force network that is dynamically excited by the intruder. If the network were to fail rapidly under the advance of an intruder, we would not expect to excite "clusters", at least not in the same way as we observe in the experiments. Also of importance is the characteristic length of the force network that is excited by a single event. In chapter 3, we saw that this characteristic length was in the range of ten to a few tens of grains (note that this is consistent with our estimate of the cluster size from Fig. 6.2). It is interesting to contrast the collisional picture of Poncelet with Bagnold scaling (Bagnold, 1954) for shear flow, where shear stresses are expected to vary as v^2 due to inter-particle collisions, but in a much less dense granular phase. Finally, we note the relevance of the speed of the intruder (at impact and later) relative to the granular sound speed. In the present experiments, this ratio is small, no more than 0.02. As the intruder speed increases relative to the granular sound speed, the present model scenario needs modification. In particular, when the intruder speed is high enough, the force signal propagating into the material cannot travel away from the intruder and relax. In any event, one might expect the typical cluster size in a collision event to grow as the impact speed approaches the granular sound speed.

How might the analysis presented in this chapter be extended to three dimensions? The fact that a number of 3D experiments with comparable impact and granular wave speeds also find v^2 scaling for the dynamic part of the drag suggests that a collisional model of the type developed here could be applied successfully to 3D. The fact that stresses from collisions can be determined within $O(1)$ normalization suggests that it may be possible to use such an approach for applications, such as maximizing or minimizing the inertial drag or understanding the stability and dynamics of rotations of granular intruders as a function of intruder shape.

7

Particle Flow Fields and Adiabatic Equilibrium

To this point, I have only considered the force response of the granular material. Surprisingly, this is sufficient to explain many aspects of the dynamics. We have observed that the photoelastic response from the grains matches well to the force the intruder feels (Chapters 3 and 4), and that the nature of the particle forces can be used to understand the velocity-squared drag and rotations (Chapter 6). However, the particle force response is only half of the story. These forces are transferring momentum to the particles, which causes the particles to flow around the intruder in a particular way. Understanding the particle flow fields, particularly how they might relate to the force picture, is the focus of this chapter.

In this chapter, I will present data on the flow of particles around circular intruders. These flow fields are obtained from non-polarized movies using particle image velocimetry (PIV), as shown in Fig. 7.1. The main result from this chapter is that, for the bulk of the trajectory (i.e., the region where $h(z) = h_0$), the intruders reach a condition of *adiabatic equilibrium* with the flow of the granular material. Specifically, the overall magnitude of the flow field is set by the intruder speed, but it is otherwise constant in the frame of the intruder. Additionally, the flow fields for all sizes

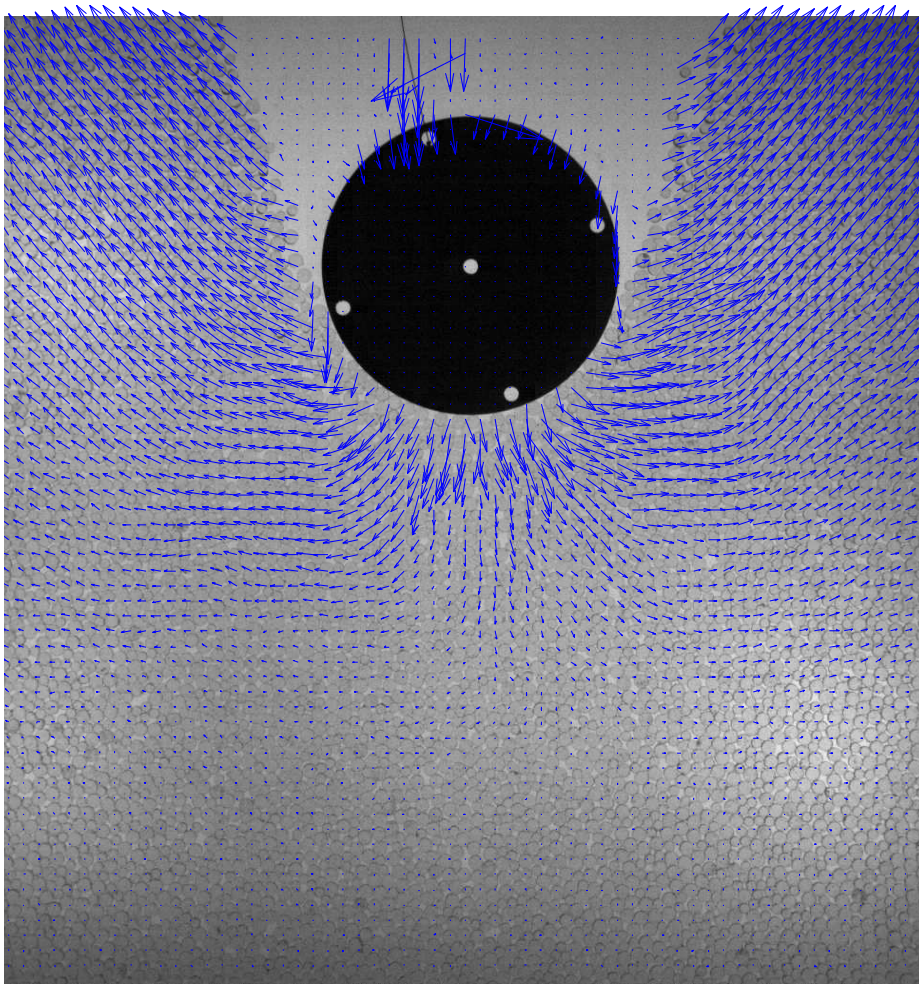

FIGURE 7.1: PIV flow field for a circular intruder at a particular frame. Arrows are estimates of local flow fields (with magnitude proportional to the arrow length) which are obtained from PIV. PIV is most successful where there is significant structure to the image (i.e., where many particles exist), but errors are much more common in empty regions, such as at the top of the image. However, these regions are not of interest physically.

of circular intruders are virtually identical when all length scales are normalized by the intruder radius. This flow field is necessarily maintained by the granular forces discussed in previous chapters.

7.1 A Steady-State Flow Field

At any instant in time, the particle flow field can be smoothed out with local spatial averaging to give an estimate of the continuum flow-field, $\mathbf{u}(\mathbf{r}, t)$, where $\mathbf{r}$ are spatial coordinates in the lab frame. If a steady-state flow field, as described above, exists, then the flow field near the intruder at each frame should be well approximated by

$$\mathbf{u}(\mathbf{r}, t) \simeq v(t)\mathbf{A}[\mathbf{r} - \mathbf{r}_0(t)], \tag{7.1}$$

where $v(t)$ is the intruder velocity (assumed to be strictly downward), $\mathbf{r}_0(t)$ is the intruder position in the lab frame (for future equations, time dependence of $\mathbf{r}_0$ is suppressed), and $\mathbf{A}$ is the steady-state velocity field. Generally, for any functional form of $\mathbf{A}$, it is possible to write the velocity field in terms of the steady-state field plus fluctuations:

$$\mathbf{u}(\mathbf{r}, t) = v(t)\mathbf{A}(\mathbf{r} - \mathbf{r}_0) + \mathbf{u}'(\mathbf{r}, t), \tag{7.2}$$

where $\mathbf{u}'$ represents the temporal fluctuations in the velocity field. If a description using a steady-state velocity field is physically reasonable, then there are obviously some constraints on the properties of $\mathbf{u}'$. For instance, $\mathbf{u}'$ should be small compared to $\mathbf{u}$, and should have temporal and spatial mean of zero. If the magnitude of the velocity is set by the intruder velocity, one might also expect that the fluctuations would scale with the intruder velocity, $\mathbf{u}' = v(t)\mathbf{A}'(\mathbf{r} - \mathbf{r}_0)$, which yields:

$$\mathbf{u}(\mathbf{r}, t) = v(t)\left[\mathbf{A}(\mathbf{r} - \mathbf{r}_0) + \mathbf{A}'(\mathbf{r} - \mathbf{r}_0, t)\right], \tag{7.3}$$

A can be measured by coarse-graining the normalized velocity field near the intruder at each time step:

$$\mathbf{A}(\mathbf{r}) = \left\langle \frac{1}{v(t)} \mathbf{u}(\mathbf{r} - \mathbf{r}_0, t) \right\rangle, \tag{7.4}$$

where the chevrons denote a time average over as much of the trajectory as possible (i.e., when the intruder is well within the video frame). Then, the fluctuating velocity field can be calculated at each frame, and the statistics of the velocity field fluctuations can be examined to determine if the steady-state velocity field picture is accurate.

7.2 Finding the Average Flow Field

The results from each PIV calculation, as shown in Fig. 7.1, can be coarse-grained to give an estimate of the continuum flow-field, $\mathbf{u}(\mathbf{r}, t)$. This continuum flow field can then be decomposed into $u_z(\mathbf{r}, t)$, the vertical component (z-direction, with downward being positive), and $u_x(\mathbf{r}, t)$, the horizontal compoen (x-direction, with rightward being positive) components of the flow field, as shown in Fig. 7.2. While velocity fields obtained from PIV are less precise than those obtained from tracking individual particles, PIV is used since the PSM-1 material is too transparent for typical particle-tracking algorithms to work. However, the grid size used for the PIV algorithm is approximately the same size as a single particle, so the particle-scale fluctuations in the velocity fields still persist.

Observation of coarse-grained velocity fields from the entire trajectory shows that flow fields from different times appear very similar when rescaled by the intruder velocity, with slight fluctuations, which is consistent with Eq. (7.3). The steady-state flow field, **A**, is measured inside the region marked in Fig. 7.2 at each frame where the entire region is inside the field of view of the camera (i.e., the red box shown in Fig. 7.2 is not cut off at the top or bottom). The average flow field, taken

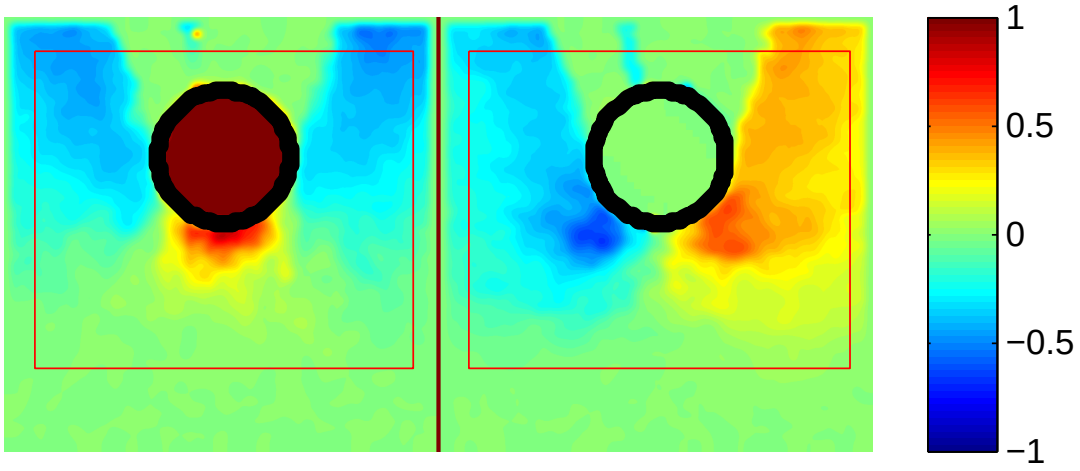

FIGURE 7.2: Coarse-grained PIV flow field for a circular intruder with diameter $D = 12.7$ cm, normalized by the instantaneous intruder velocity ($v = 3.05$ m/s). The left panel shows the normalized vertical velocity, u_z/v, and the right panel shows the horizontal velocity, u_x/v. The region inside the intruder boundary is given the velocity of the intruder to make the coarse-graining more smooth. The red box encloses the region over which the steady-state velocity field will be obtained, which will move along with the intruder (i.e., the steady-state velocity field is in the frame of the intruder).

over approximately 300 pairs of frames in a single trajectory, is shown in Fig. 7.3. Note that it appears very similar to the instantaneous flow field shown in Fig. 7.2, but smoother spatially.

7.3 Fluctuations in the Flow Field

Once the average flow field is defined and measured, temporal fluctuations at each frame can be measured as:

$$\mathbf{A}'(\mathbf{r},t) = \frac{1}{v(t)}\mathbf{u}(\mathbf{r}-\mathbf{r}_0,t) - \mathbf{A}(\mathbf{r}) \tag{7.5}$$

A representative measurement of $\mathbf{A}'$ is shown in Fig. 7.3. The absolute magnitude of $\mathbf{A}'$ is small, with a maximum of about 0.2 (where a value of 1 would correspond

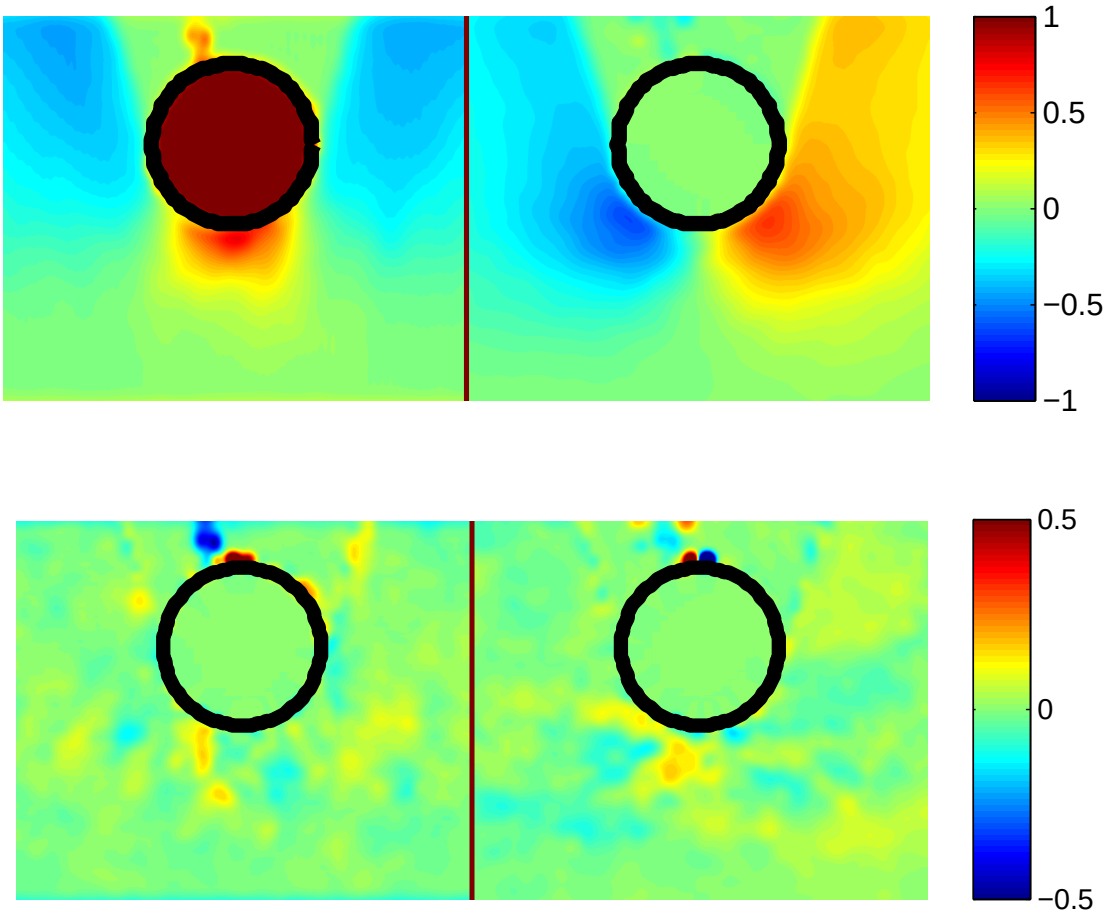

FIGURE 7.3: Top panel shows the average flow field, $\mathbf{A}(\mathbf{r}-\mathbf{r}_0)$, for a circular intruder with diameter $D = 12.7$ cm (see text for details). The left side shows the vertical velocity A_z, with downward being positive, and the right side shows the horizontal velocity, A_x, with rightward being positive. The bottom panel shows the instantaneous fluctuations in the flow field at a particular frame, $\mathbf{A}'(\mathbf{r}-\mathbf{r}_0, t)$, for a circular intruder with diameter $D = 12.7$ cm. The left side shows the vertical velocity fluctuations, A'_z, with downward being positive, and the right side shows the horizontal velocity fluctuations, A'_x, with rightward being positive.

to a local velocity fluctuation of the same size as the intruder speed).

By construction, the time average of the fluctuating field is zero. However, physically, it is intended to represent fluctuations arising from the finite size of the particles and collecive particle rearrangements, not a systematic fluctuation as the intruder speed changes. That is, it should be stochastic in time and decoupled from the intruder dynamics, similar in spirit to the fluctuating force term, $\eta(t)$, in Chapter 4.

To test this, I evaluate the average magnitude of the fluctuations beneath the intruder at each frame,

$$A'_{avg}(t) = \frac{\iint_\Omega |\mathbf{A}'| dxdz}{\iint_\Omega dxdz}, \tag{7.6}$$

where Ω is the domain defined by a half annulus extending from the bottom of the intruder out one intruder radius and spanning 180° centered beneath the intruder (similar to the region used to measure force in Chapter 3). For reference, the area of this half annulus is approximately 0.17 m^2. This yields a time series which is shown in Fig. 7.4. The plot shows that A'_{avg} is approximately constant in time, suggesting that the characteristic size of the fluctuations is set by the intruder velocity as in Eq. (7.3).

As a further test, to observe how the fluctuations vary in time locally, I examine a time series of the fluctuations evaluated at a particular point in space. Specifically, I plot A'_z evaluated at $(r - r_0) = 3R/2$ and $\theta = 0$ (i.e., $R/2$ beneath the lowest point of the intruder). This plot is shown in the bottom panel of Fig. 7.4. This time series appears to be randomly fluctuating around zero, with no systematic behavior as the intruder slows down (i.e., not monotonically increasing or decreasing), which is representative of the velocity fluctuations at any point in space.

To spatially characterize the size of the velocity fluctuations, Fig. 7.5 shows the

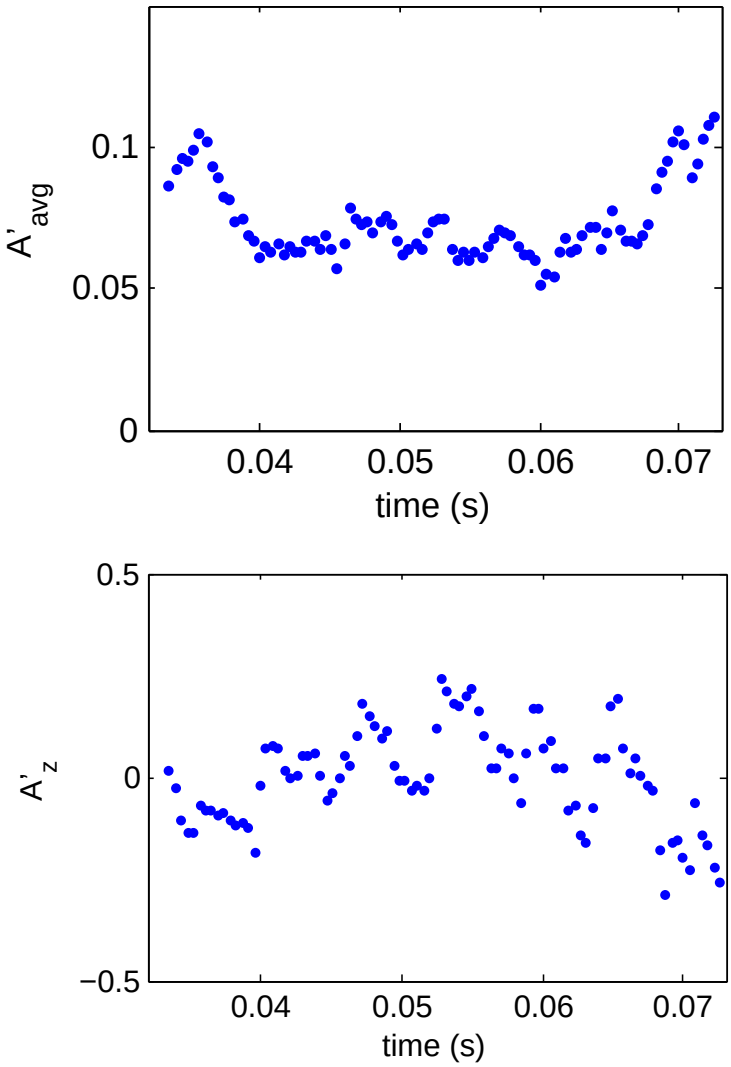

FIGURE 7.4: Top panel shows a plot of A'_{avg} evaluated in a half annulus beneath the intruder, defined by $R < r - r_0 < 2R$ and $-\pi/2 < \theta < \pi/2$, where R is the intruder radius, and θ is measured from the intruder center with $\theta = 0$ corresponding to downward (positive z-axis). The plot is relatively flat in time, suggesting that the characteristic size of the fluctuations captured by $\mathbf{A}'$ is unchanged as the intruder slows down. The characteristic size of $\mathbf{A}'$ is close to 0.1, which is consistent with Fig. 7.3. Bottom panel shows a plot of A'_z evaluated at $(r - r_0) = 3R/2$ and $\theta = 0$, which corresponds to the point $R/2$ beneath the lowest point of the intruder. The signal appears to be randomly fluctuating around zero, with no systematic behavior as the intruder slows down (i.e., not monotonically increasing or decreasing). This is characteristic of any measure of the velocity fluctuations at any point.

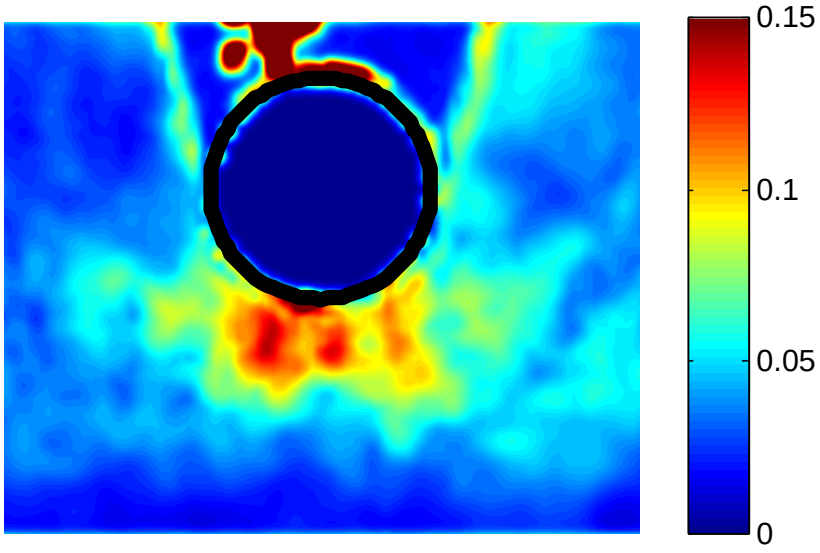

FIGURE 7.5: Plot of the time-averaged fluctuation magnitude, $A'_{rms}(\mathbf{r})$. The fluctuations are strongest, around $|\mathbf{A}'| \approx 0.1$, directly beneath the intruder.

time-averaged magnitude of the fluctuations $\mathbf{A}_{rms}$, defined as:

$$A'_{rms}(\mathbf{r}) = \frac{\int |\mathbf{A}'| dt}{\Delta t}. \tag{7.7}$$

This plot shows that the velocity fluctuations are strongest in the region beneath the intruder (e.g., in the region Ω used to calculate A'_{avg}). In this region, the average fluctuations are about $|\mathbf{A}'| \approx 0.1$, which is consistent with previous measurements A'_{avg} and A'_z. The region where the velocity fluctuations are the strongest can be understood in terms of geometry of particle flow: this is also the region with strong velocity gradients, meaning that particles are forced to rearrange as they move past each other.

7.4 Steady-State Flow Fields for Different Intruder Sizes

Now that the idea of a steady-state flow field is justified, one interesting question is how the steady-state flow field changes with varying intruder size. The average flow fields, $\mathbf{A}(\mathbf{r}, t)$, for four different sizes of circular-nosed intruders are shown in Fig. 7.6. Three circles are shown, with diameters D =6.35, 9.3, 12.7, and 20.3 cm. The $D = 9.3$ intruder is an ogive, with a circular nose and rectangular tail, but the particles are never in contact with the intruder tail. All four flow fields appear very similar relative to the diameter of the intruder. To test this further, I attempt to fit functions to mathematically characterize each steady-state vector field, and the fits can be compared for different intruder sizes. For these fits, I will consider the flow field in the frame of the circular intruder, $\mathbf{A}_{circ} = \mathbf{A} - \hat{\mathbf{z}}$. This transformation yields a flow field which is equivalent the case where the material is being pushed past a stationary intruder. Similar to Seguin et al. (2013), I assume a decomposition of $\mathbf{A}_{circ}$ into radial and angular components:

$$\mathbf{A}_{circ}(\mathbf{r}) = A_r(\mathbf{r})\,\hat{\mathbf{r}} + A_\theta(\mathbf{r})\,\hat{\boldsymbol{\theta}} \tag{7.8}$$

$$= a_r(r)\cos[b_r(r)\theta]\,\hat{\mathbf{r}} + a_\theta(r)\sin[b_\theta(r)\theta]\,\hat{\boldsymbol{\theta}}, \tag{7.9}$$

where $\mathbf{r} = 0$ corresponds to the center of the intruder. Seguin et al. used this form to describe quasistatic granular flow around circular obstacles, but with $b_r = b_\theta = 1$, since, in the quasistatic case, the flow is symmetric ahead of and behind the intruder. Here, I will consider fits only to the half-space in front of the intruder. Sample fits at particular values of r are shown in Fig. 7.7. The error in these fits is greatest very near the intruder edge.

By looking at various values of r, the fit parameters—$a_r(r), b_r(r), a_\theta(r), b_\theta(r)$—can be found for each intruder, and plotted as a function of r/R. This plot is shown in Fig. 7.8. When rescaled by the intruder radius, the fit parameters for each intruder appear very similar. This suggests that there is a particular form for the steady-state

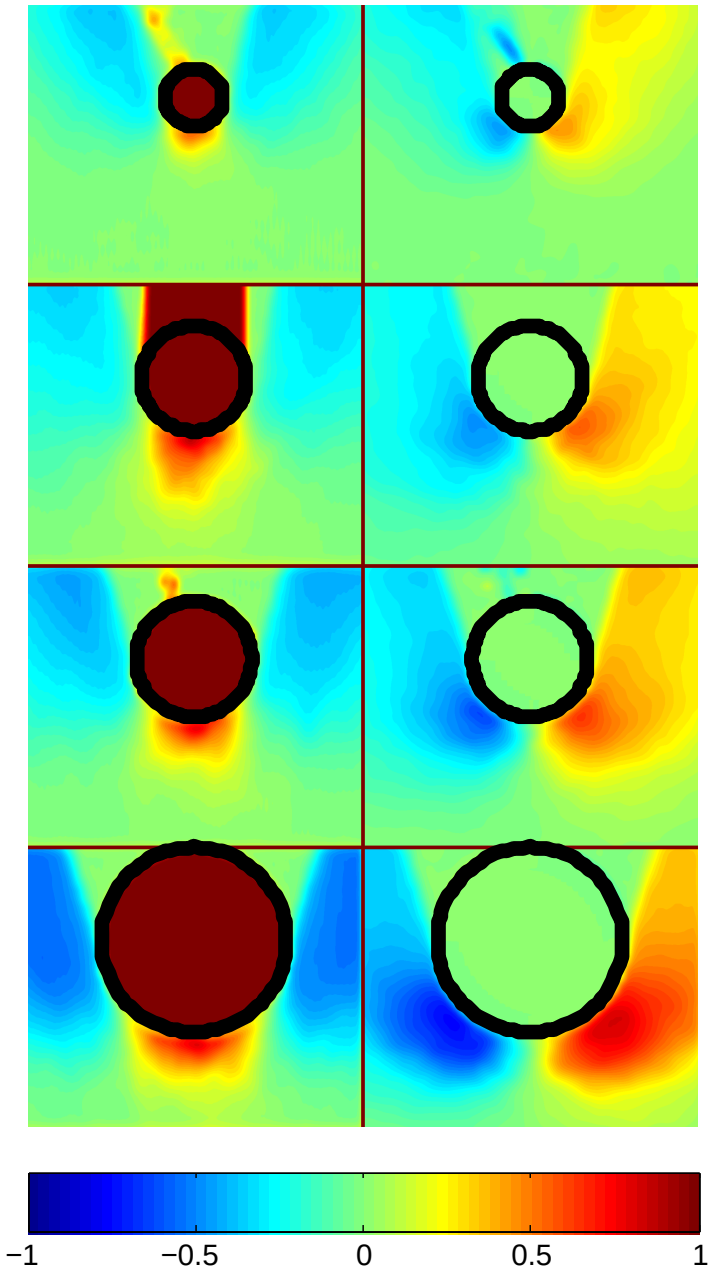

FIGURE 7.6: Plot of the average flow fields, A_z (left) and A_x (right), for four different circular intruders, with diameters

vector field for circles, $\mathbf{A}_{circ}$, and, for circular intruders, Eq. (7.1) can be written:

$$\mathbf{u}(\mathbf{r},t) \simeq v(t)\mathbf{A}_{circ}\left[\frac{\mathbf{r}-\mathbf{r}_0(t)}{R}\right], \tag{7.10}$$

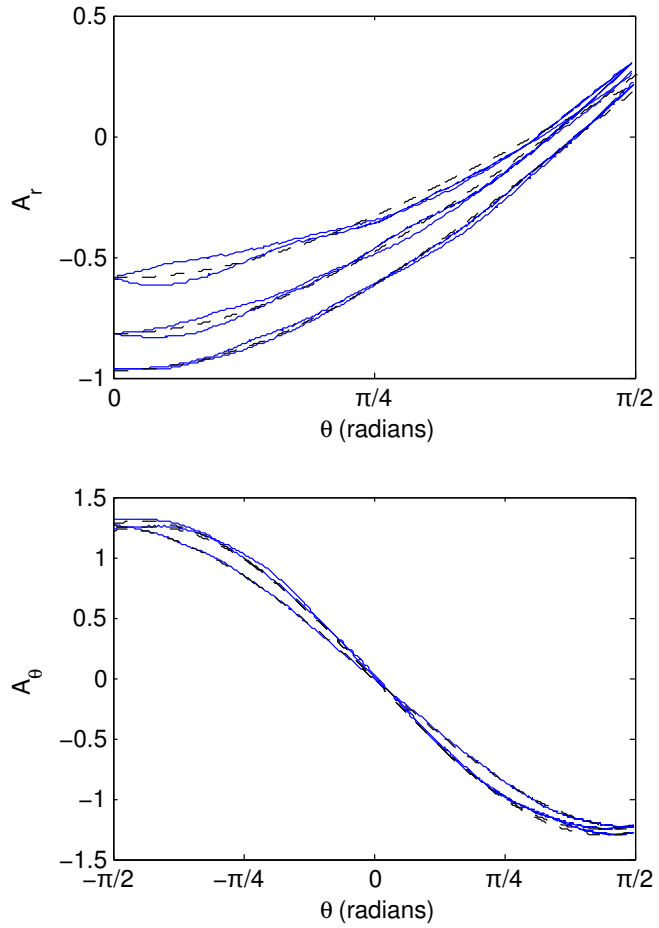

FIGURE 7.7: Sample fits of the flow field to the form shown in Eq. (7.9) for the smallest intruder ($D = 6.35$ cm at particular values of r, namely $r = 1.5R, 2R$, and $3R$, where $r = R$ corresponds to the intruder boundary. Solid blue lines are data, and dashed black lines are fits of the form shown in Eq. (7.9). These fits are typical for all fits.

Thus, even for circular intruders with diameters (D) ranging from about 10 about 30 particle diameters (d), the shape of the steady-state flow field is not substantially affected by the intruder size.

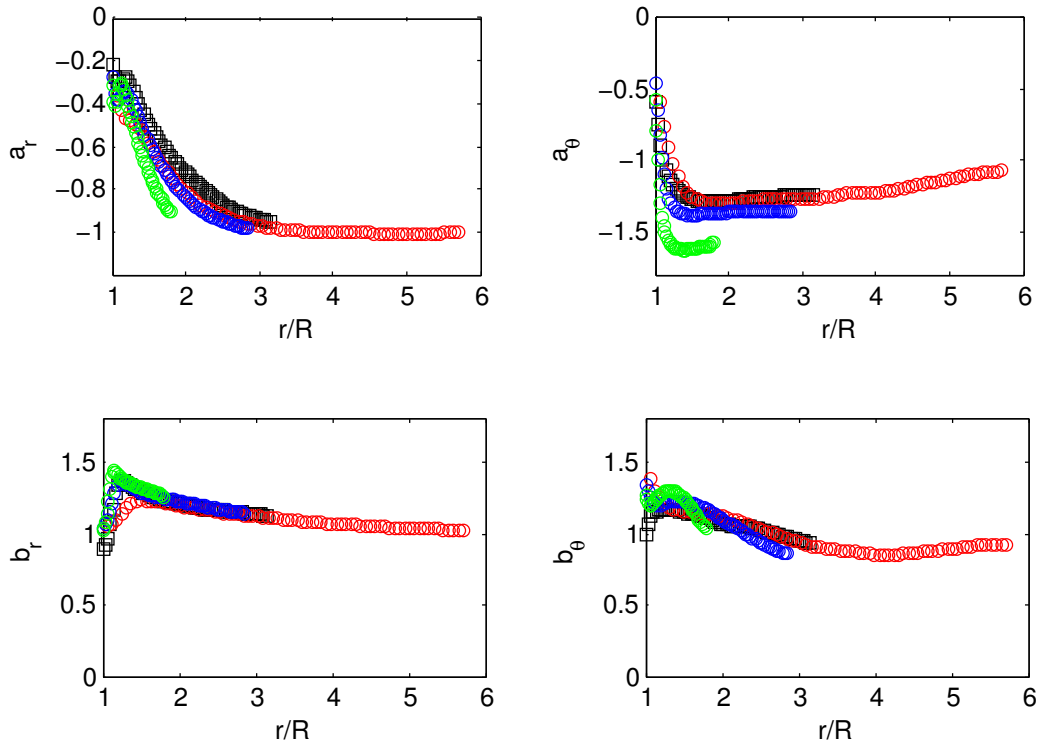

FIGURE 7.8: Comparison of the fit parameters—$a_r(r), b_r(r), a_\theta(r), b_\theta(r)$—for each of the four circular intruders shown in Fig. 7.6.

7.5 Conclusion

In this chapter, I have presented data on the velocity flow fields of the granular material around circular intruders of varying diameter. These data demonstrate the existence of a steady-state velocity flow field, such that the particle flow near the intruder is well approximated at any time by the intruder velocity times some constant vector-valued function, **A**, which is centered at the intruder center, as in Eq. (7.1). Additionally, the velocity fluctuations with respect to the steady-state flow field have a characteristic size which also scales with the intruder speed, as in Eq. (7.3), with a typical magnitude of about 10% of the intruder velocity.

Additionally, the steady-state flow field for four different circular intruders was fitted to the form given in Eq. (7.9). This procedure showed that for all four circular intruders, the steady-state flow field is very similar when spatially rescaled by the size of the intruder.

These results provide several important physical insights. First, the particular form of Eq. (7.3) suggests that, during the bulk of the trajectory, the particle motion near the intruder is linearly dependent on the intruder velocity and otherwise constant. A constant flow field and fluctuations which scale linearly with the intruder velocity suggest that the particle motion is determined by how far the intruder moved, not how fast it is moving. Second, the intruder and particles are in a kind of *adiabatic steady-state*: as the intruder advances, the particles happily clear a path at the proper rate. Maintaining this flow takes away momentum and energy from the intruder, which is necessarily consistent with the force picture discussed in previous chapters. Thus, the force pulses from previous chapters are transmitting information on how the particles should move. The fact that these pulses move so fast compared to the intruder speed means that the particles are able to respond quickly compared to intruder motion. Third, the existence of a steady-state flow field as defined in this chapter implies that the particles near the intruder are always moving at a velocity which scales with the intruder velocity. This justifies the assumption in the previous chapter, where the clusters were assumed to be stationary or at least to have a velocity which is proportional to the intruder velocity. Fourth, the fact that the steady-state field is very similar for different circles when rescaled by the intruder size means that the granular material is behaving like a continuum, and the microscopic length scale plays a smaller role than the other characteristic length scale in the problem (i.e., intruder size).

Finally, the fact that the flow field is constantly slowing to match the intruder speed is reminiscent of an adiabatic process, where a dynamical process is driven by

a state variable which changes sufficiently slowly such that the system is always in equilibrium. Since the flow field appears to be in a kind of equilibrium state, it is possible that the impact process, under the set of conditions which yield a steady-state flow field, can be thought of as a well developed flow, placing it in the same regime as constant-velocity drag experiments (Takehara et al., 2010). Additionally, perhaps this flow could even be compared to continuum rheologies for well developed flows, such as $\mu(I)$ (da Cruz et al., 2005; Jop et al., 2006; Kamrin and Koval, 2012). Testing its consistency with a continuum description presents a very interesting direction for future research. Many of these rheologies, such as $\mu(I)$, were developed for shear flows, and have not yet been tested for something like flow around an intruder.

8

Limits of the Force Law: Increasing Mach Number

In the previous chapters, I have presented a comprehensive picture of two-dimensional impact experiments into hard, photoelastic disks (PSM-1 material). The impacts speeds were limited to $v_0 \leq 6.6$ m/s, and a typical sound speed is $c \approx 300$ m/s, meaning that the speed at which particles transfer force and momentum to one another is about two orders of magnitude faster than the speed at which the intruder moves. In this regime, we observe the formation of a steady-state flow field around the intruder, which is maintained by intermittent force pulses generated randomly at the intruder surface. Thus, the intruder and the particles are in a kind of adiabatic equilibrium, where the driving (i.e., the intruder speed) is changing sufficiently slowly that the flow field stays in equilibrium with the intruder.

The idea of a adiabatic elimination is used in a variety of dynamical systems, when the evolution of two state variables happens at very different rates. The slow variable is assumed to be constant on the time scale of the fast variable, and the fast variable can be averaged over when considering changes in the slow variable. However, when the system parameters which affect these rates are changed, these assumptions can obviously break down. In the present case, the fast process is the

force transmission between individual particles, which enacts the particle flow field. The rate of force transmission is governed by a characteristic collision time t_c which depends on softness of the particles. The slow process is the intruder motion with a typical time scale t_d, which is very large compared to the time scale of force pulses (see Fig. 3.1).

For impacts where these rates are more similar, one might expect the dynamics to change. Since increasing v_0 substantially is very difficult in our experiment, we accomplish this by using softer particles and thereby lowering the speed of force transmission in the material. In this chapter, I will present results from experiments using two varieties of particles (Shore 60A and 80A) which are softer than the particles discussed in previous chapters. We will see that the description for hard particles from previous chapters, involving a steady-state flow field and a velocity-squared drag force, breaks down for softer particles. As the particles are made softer and t_c becomes larger, the response of the granular assembly becomes more elastic like: instead of moving out of the way of the advancing intruder, the particles store energy via elastic compression, and the final penetration depth is drastically reduced.

Thus, by making the particles *softer*, the system becomes significantly more difficult to penetrate. This is demonstrated in Fig. 8.1, where the final penetration depth is plotted as a function of initial kinetic energy for impacts into each of the three different materials. Surprisingly, the final penetration depth is approximately the same for Shore 60A and Shore 80A particles. As mentioned in the introduction, looking at the final penetration depth as a function of time gives limited information, and the trajectories themselves (e.g., the force law approach used for hard particles) must be analyzed to paint a more complete picture.

The rest of this chapter is structured as follows. First, I will derive a dimensionless number, $M' \equiv t_c/t_d$, which I will use to classify the different impact regimes. I will then present data from the softest particles (Shore 60A), where M' is typically

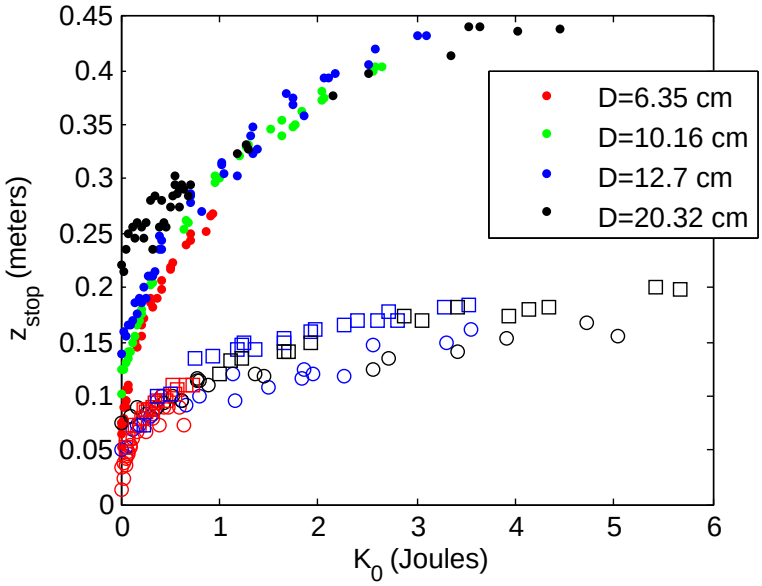

FIGURE 8.1: The final stopping depth, z_{stop}, is plotted versus the initial kinetic energy, K_0, for circular intruders of three different sizes into three different materials. Color code for the circular intruders is shown in the legend. Dots represent impacts into PSM-1, squares represent impacts into Shore 80A, and circles represent impacts into Shore 60A. The legend shows color scheme for different intruders. Surprisingly, by making the system softer, final penetration depth becomes much smaller.

around 0.5 and as high as 0.7 for the fastest impacts. These impacts are solidly in a new, *elastic-like regime*, which I will describe. I will also present data for particles with an intermediate stiffness (Shore 80A), with $M' \sim 0.2$, which shows the crossover between the elastic-like regime, where $M' \to 1$, and the inertial drag regime studied in previous chapters, where $M' \sim 0.01$. Impacts into these particles will show characteristics of both regimes.

8.1 Defining a Dimensionless Number

In granular materials, grain-grain interactions are typically governed by a nonlinear force law, leading to a sound speed which is not constant but dependent on the local confining pressure (Liu and Nagel, 1992). A sound speed is found by linearizing about the confining pressure, which gives the speed a which small-amplitude pressure pulses

propagate. Pulses with a large enough pressure amplitude can violate the linear assumption, which yields a propagation speed which depends on the amplitude of the pulse (Liu and Nagel, 1992). As local confining pressure vanishes, as it does at the top of the granular assembly discussed in present experiments, the linear response region vanishes (Liu and Nagel, 1992; Makse et al., 2004; Gómez et al., 2012). In this case, or in the limit of large-amplitude pulses, the speed at which forces propagate is dominated by the form of the nonlinear force law for grain-grain interactions (Gómez et al., 2012), and it can be strongly dependent on the characteristic pressure associated with the pulse.

For these reasons, one must take care in clearly defining something like a Mach number for granular materials. Here, we will use a dimensionless number which is the ratio of two time scales: t_c, the characteristic collision time between two particles which are initially only just contacting each other, and t_d, the time scale for the intruder to move one particle diameter. Obviously, t_d is just the particle size, d, divided by the characteristic intruder speed, which is chosen as the initial speed at impact, v_0.

$$t_d \equiv \frac{d}{v_0} \tag{8.1}$$

The most obvious definition for t_c is the total contact time during a normal collision of two identical particles, given a particular form for the grain-grain force law.

To solve for t_c, we consider a one-dimensional collision between two identical particles of mass m_p which are governed by the following force law:

$$\mathcal{F} = k\delta^{\alpha}. \tag{8.2}$$

Here, $\mathcal{F}$ is the force given a total compression δ shared between both particles, and α is a positive number. One particle is moving at some characteristic velocity, which I will choose to set as the initial intruder velocity, v_0, and it collides with another

particle which is stationary, where the incident velocity is parallel to the vector which connects the particle centers (i.e., the collision is one-dimensional). In this case, energy conservation in the center of mass frame yields:

$$2 \cdot \left[\frac{1}{2} m_p \left(\frac{v_0}{2}\right)^2\right] = 2 \cdot \left[\frac{1}{2} m_p v_p'^2\right] + \frac{k\delta^{\alpha+1}}{\alpha+1}. \tag{8.3}$$

Here, v_p' is the velocity of each particle in the center of mass frame, where the center of mass velocity is given by $v_0/2$. By setting $v_p' = 0$, we can solve for the maximum compression of each particle:

$$\delta_{max} = \left[\frac{m_p v_0^2(\alpha+1)}{4k}\right]^{\frac{1}{\alpha+1}}. \tag{8.4}$$

Additionally, integrating Eq. (8.3) from $\delta = 0$ to $\delta = \delta_{max}$ and multiplying by a factor of two yields the total time the two particles are in contact:

$$\begin{aligned} t_c &= \frac{4}{v_0}\left[\frac{m_p v_0^2(\alpha+1)}{4k}\right]^{\frac{1}{\alpha+1}} \int_0^1 \frac{du}{\sqrt{1-u^{\alpha+1}}} \\ &= \frac{4\sqrt{\pi}}{v_0}\left[\frac{m_p v_0^2(\alpha+1)}{4k}\right]^{\frac{1}{\alpha+1}} \frac{\Gamma\left(1+\frac{1}{\alpha+1}\right)}{\Gamma\left(\frac{1}{2}+\frac{1}{\alpha+1}\right)}. \end{aligned} \tag{8.5}$$

Note that for linear springs, where $\alpha = 1$, the collision time is independent of velocity, as expected.

Thus, I define a dimensionless number, M', as the ratio of these two time scales:

$$M' \equiv \frac{t_c}{t_d} = \frac{4\sqrt{\pi}}{d}\left[\frac{m_p v_0^2(\alpha+1)}{4k}\right]^{\frac{1}{\alpha+1}} \frac{\Gamma\left(1+\frac{1}{\alpha+1}\right)}{\Gamma\left(\frac{1}{2}+\frac{1}{\alpha+1}\right)}. \tag{8.6}$$

The particles mass, m_p, and diameter, d, are known, and the values for k and α can be taken from the measurements in Fig. 2.3. Thus, we can plot M' for each of the three particles used, as shown in Fig. 8.2. This plot shows that typical impact speeds into the softest particles (Shore 60A) are approaching the point where $M' \sim 1$ (for

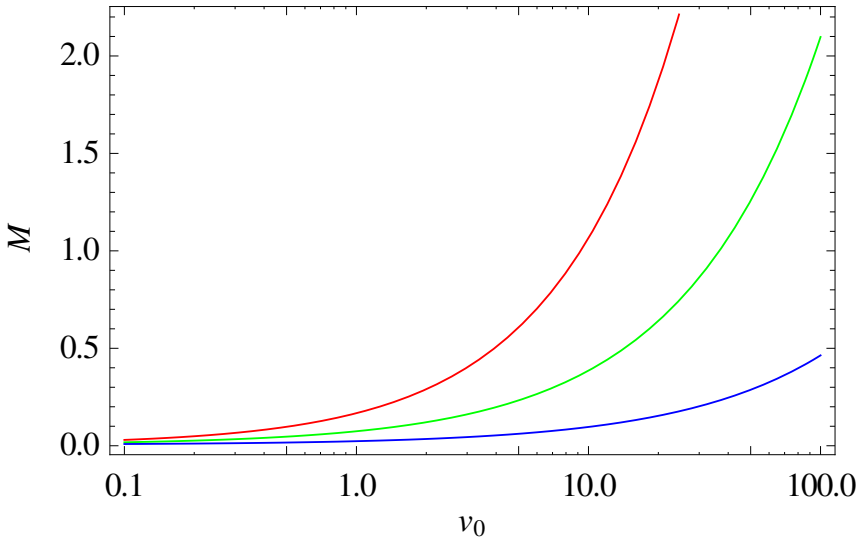

FIGURE 8.2: Plot of the dimensionless number, M', versus initial impact velocity for each of the three types of particles used here. The softest particles (Shore 60A) are represented by the red, leftmost curve, the intermediate stiffness (Shore 80A) particles are represented by the green, center curve, and the hardest particles (PSM-1) are represented by the blue, rightmost curve. When $M' = 1$ is when the intruder motion time, t_d, is equal to the characteristic particle collision time, t_c, as defined in the text.

$v_0 = 6$ m/s, $M' \approx 0.7$). For the intermediate stiffness (Shore 80A), $M' \sim 1$ at impact speeds between 10 and 50 m/s, and $M' < 0.25$ at typical impact speeds in these experiments. For the hardest particles (PSM-1), $M' \sim 1$ at impact speeds between 100 and 500 m/s, and $M' < 0.06$ at typical impact speeds in present experiments.

Using this time scale, we can approximate the zero-pressure limit (or large-amplitude limit) of a one-dimensional pulse propagating from grain to grain as a series of these collisions, where the velocity is given by the grain diameter divided by the collision time:

$$c \sim \frac{d}{t_c} \sim v_0^{\left(\frac{\alpha-1}{\alpha+1}\right)}. \tag{8.7}$$

This scaling agrees with the result from Gómez et al. (2012), where the authors

performed simulations with Hertzian particles ($\alpha = 3/2$) in a channel where one wall is given a fixed velocity. In this case, a compression front propagated through the granular material with a velocity which scaled with the wall velocity to the power 1/5. Inserting $\alpha = 3/2$ into Eq. (8.7) yields the same result. The propagating wave was quasi-1D in this case, since the sidewalls were fixed and the particles could not expand laterally; in our case, particle can and do expand laterally, so the quasi-1D scaling may not hold.

Finally, one would expect the ratio d/t_c to underestimate the propagation velocity, since the simplified picture assumes that each collision will finish before another one begins. However, we can estimate the force propagation speed from space-time plots, such as in Fig. 3.1. This yields values of $c \approx 30$ m/s for Shore 60A, $c \approx 100$ m/s for Shore 80A, and $c \approx 300$ m/s for PSM-1. By plugging in measured values for k and α, along with a typical values for the initial velocity v_0, we find that the measured values for force propagation do roughly scale with d/t_c for different materials:

$$c \approx 4 \left(\frac{d}{t_c} \right). \tag{8.8}$$

8.2 Impacts into Soft Particles

As in the previous chapters, we would like to examine the impacts using photoelastic data as well as the trajectory of the intruder with the goal of describing the basic physical processes which govern dissipation of the intruder's energy and momentum. For the softest particles, we know that we are approaching $M' \sim 1$, so we expect the particle-collision time scale to begin to dominate, and the response to become more elastic-like.

8.2.1 Qualitative Behavior

Three sample trajectories for impacts into soft particles are shown in Fig. 8.3. These three impacts are for a circular intruder with a diameter of 12.7 cm, with initial impact speeds of around 1, 2.5, and 5 m/s. Immediately, we see that the intruder dynamics are very different from the hardest particles. All three trajectories have a local minimum in their velocity curves at around 50 milliseconds (ms), where the intruder velocity is almost zero. They are then accelerated downward again after this initial "bounce" (i.e., the local velocity minimum) until they reach their final depth, which is roughly 50% deeper than the depth at which the intruder reached its first velocity minimum. These trajectories are obviously inconsistent with a velocity-squared drag; indeed, plotting the acceleration versus velocity-squared at constant depth, as in Fig. 3.6, does not yield straight lines.

Photoelastic images of these impacts provide additional insight, as shown in Fig. 8.4, which shows still frames from the first 5 ms of the slowest (top frames, $v_0 \approx 1$ m/s, $M' \approx 0.15$) and fastest (bottom frames, $v_0 \approx 5$ m/s, $M' \approx 0.6$) from Fig. 8.3. For the slowest impact, the first two frames appear qualitatively similar to images from similar impacts into hard particles: forces propagate away from the intruder in force-chain-like structures. However, the force information propagates much more slowly, and the granular material is unable to relax as the intruder continues to move forward. Thus, the intruder energy is stored elastically via compression of particles.

The bottom row of frames in Fig. 8.4, showing the impact with $v_0 \approx 5$ m/s and $M' \approx 0.6$, shows a more extreme case of this behavior. When the intruder strikes, the pressures beneath the intruder are very strong, and the forces are not carried in force-chain-like structures, but in a strongly compressed front with a well defined boundary which moves away. This compression front quickly connects to the lower boundary

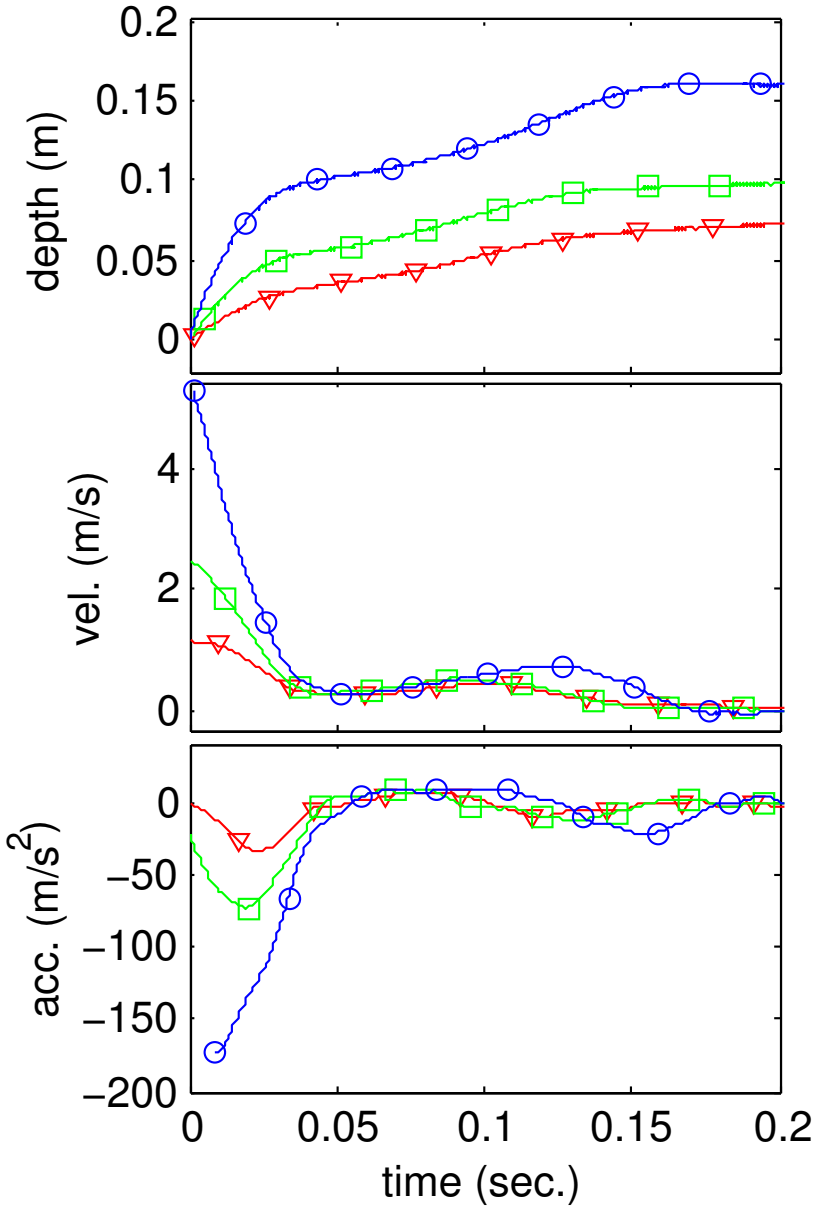

FIGURE 8.3: Plots of depth, velocity, and acceleration for three different impacts into soft particles (Shore 60A) by the $D = 12.7$ cm disk. These trajectories appear qualitatively different from the impacts into hard particles.

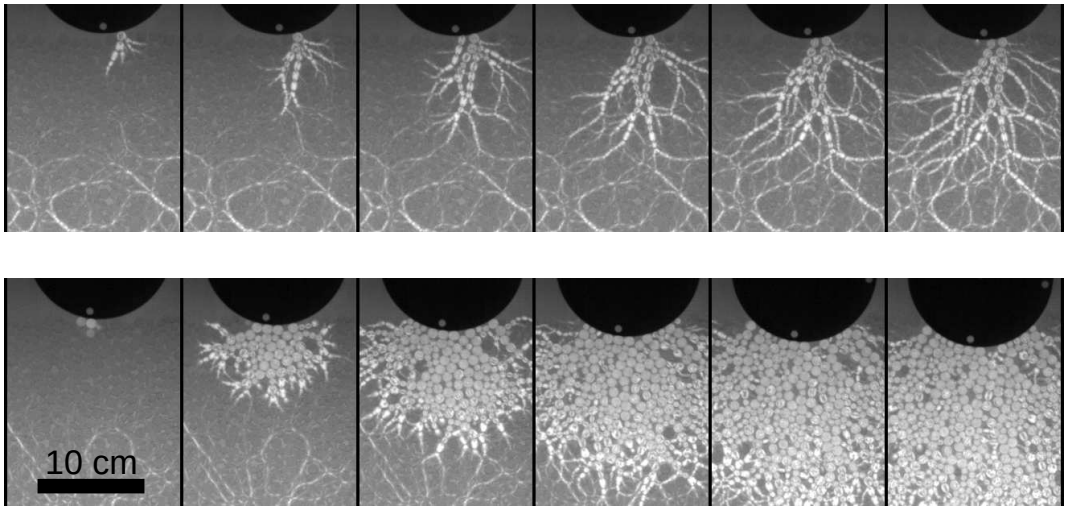

FIGURE 8.4: Sequence of frames depicting an impact into soft particles (Shore 60A). The frames shown are at times 0, 1, 2, 3, 4, and 5 ms after initial impact. The top row corresponds to the weakest impact shown in Fig. 8.3 with $v_0 \approx 1$ m/s, and the bottom row corresponds to the strongest impact trajectory shown in Fig. 8.3 with $v_0 \approx 5$ m/s.

of the experiment. Thus, in the impacts shown in Figs. 8.3 and 8.4, the intruder energy is transmitted to elastic compression of the particles beneath it, as opposed to momentum in the flow field which is transmitted via intermittent collisions, as in impacts into hard particles. The elastic compression takes the intruder energy away much more quickly than before, and the intruder essentially comes to a stop after 50 ms, much faster than for impacts into hard particles (Fig. 6.6).

After this, the stored elastic energy unloads, imparting an upward momentum to almost the entire collection of grains. This reduces the density of the granular material beneath the intruder, allowing it to sink a bit farther. This effect can be observed by examining photoelastic force response and particle flow together. Figure 8.5 shows data from two different movies: one is taken with polarizers, yielding the intruder trajectory and the particle force response, and the other is taken without

polarizers, yielding the intruder trajectory and the particle positions. However, the two have very similar trajectories, so we examine them together to get a qualitative idea of the correspondence between particle forces and motion.

During the first two frames in each row of Fig. 8.5, the elastic compression is spreading toward the lower boundary of the experiment (which is only a few particle diameters from the bottom of the photoelastic images shown in Fig. 8.5). During these first two frames, the particles are being forced down as the system is compressed, which is reflected in the flow fields. The third frame, taken when the intruder is essentially stationary, shows that the elastic energy is in the process of unloading (shown in the photoelastic image) and transferring upward momentum to the grains (shown in the particle tracking and momentum flow fields). In the fourth frame, the elastic energy is finished unloading and the intruder is moving downward. Note that the first and fourth photoelastic frame show that the photoelastic response near the bottom of the bed is even weaker than before the intruder struck at all. After the intruder has come to rest, the photoelastic response near the bottom of the bed is back to its original state plus a moderate amount from the intruder weight.

8.2.2 Front Propagation

By looking at a thin, vertical slice beneath the intruder, and considering the total photoelastic response at each depth as a function of time, we can measure a velocity at which the compression front is propagating. The top panel of Fig. 8.6 shows a space-time plot of a thin region of a photoelastic image (width of R, the intruder radius, centered vertically with the intruder center) for an impact with initial velocity $v_0 \approx 4$ m/s. Red colors represent strong photoelastic response, and blue colors represent weak photoelastic response (the dark blue region at the top of the image corresponds to the region occupied by the intruder). The slope of the front (visualized by a thick, red line) represents the front velocity (here, about 40 m/s).

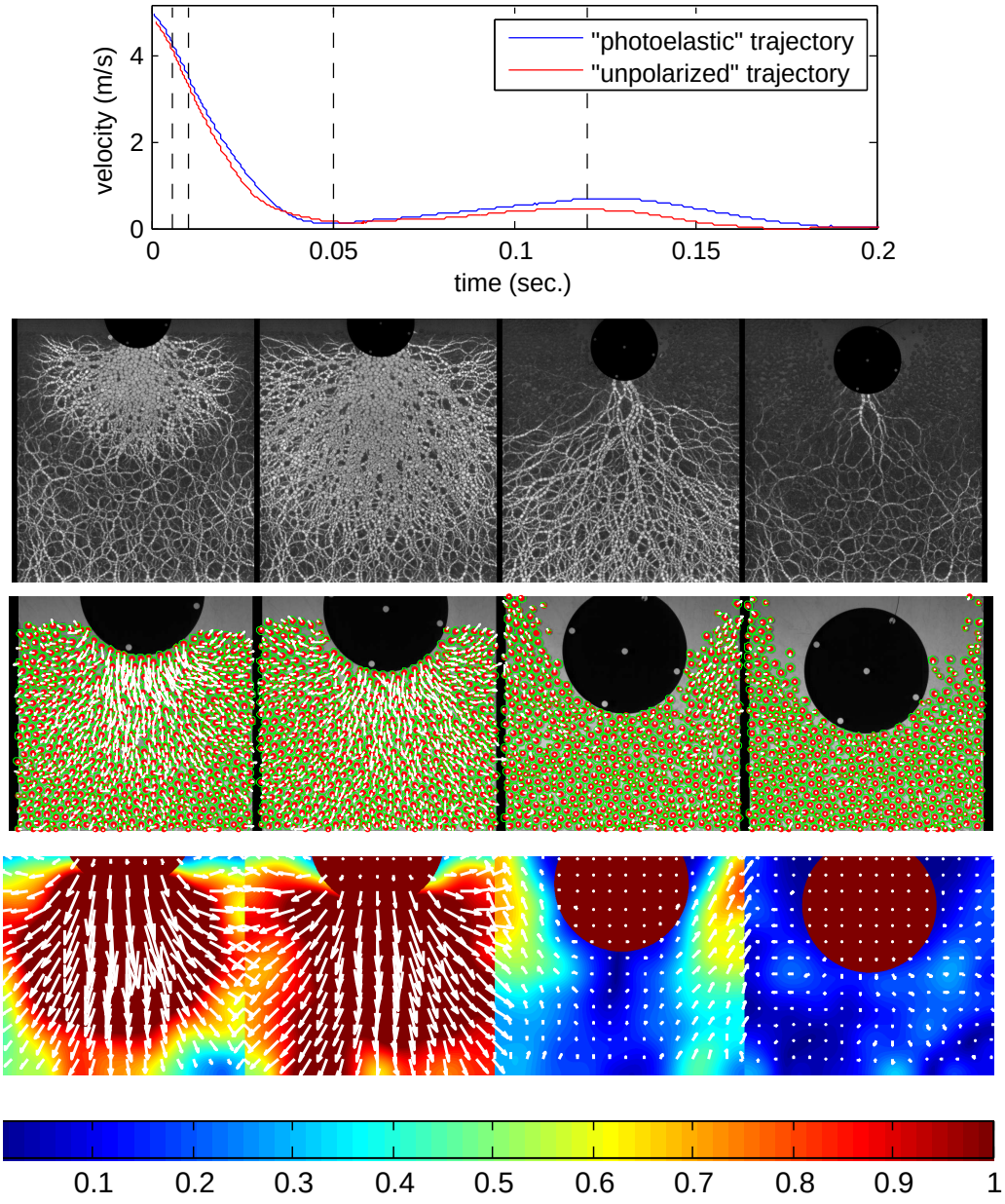

FIGURE 8.5: Frames from two impacts with $v_0 \approx 5$ m/s: the "photoelastic" impact is recorded with polarizers and shows forces, while the "unpolarized" impact is recorded without polarizers which allows particle tracking. The top panel shows the velocity profiles, along with the four time slices where the images and flow fields are shown (dashed black lines, at 5.5, 10, 50, and 120 ms after impact). First row of images shows particle force response, second row shows particle positions and velocities (marked with small arrows), and the bottom row shows coarse-grained momentum fields with units of particle area fraction (or packing fraction) times velocity.

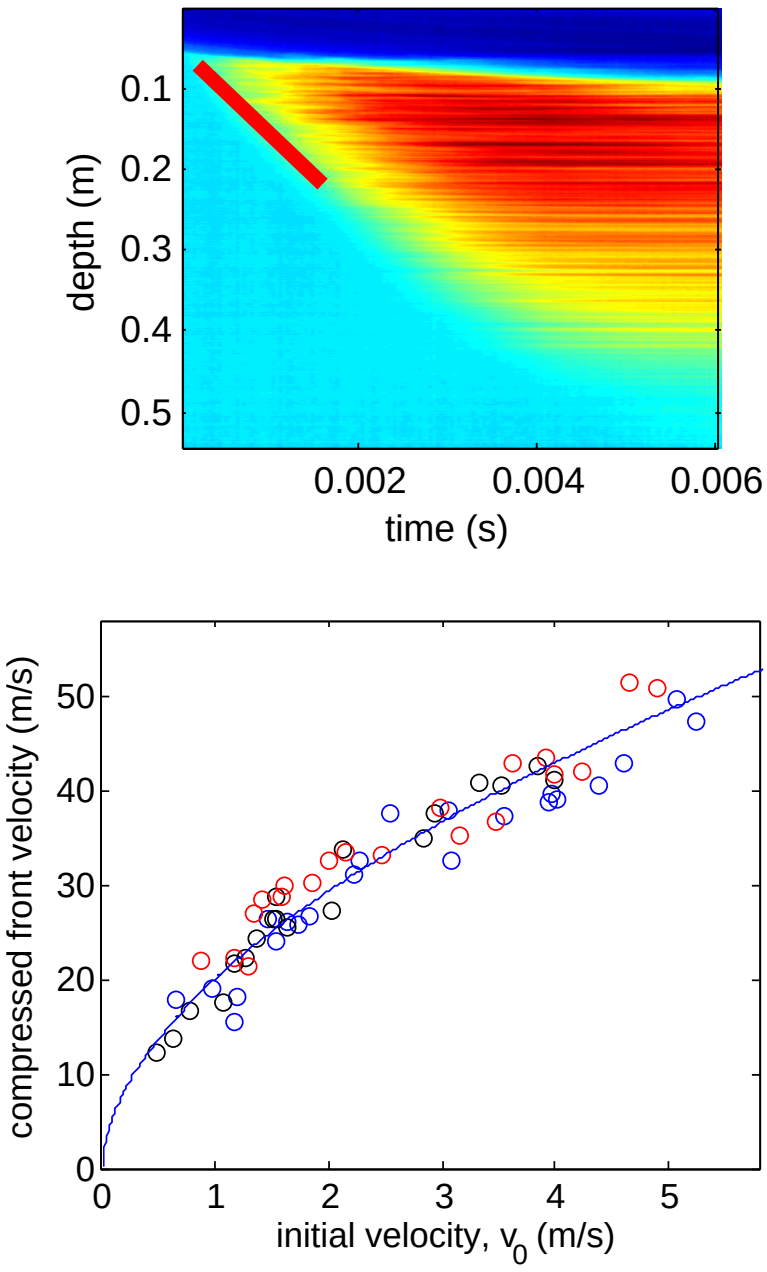

FIGURE 8.6: Top panel shows a space-time plot of the photoelastic response in thin column beneath the intruder. The speed of this front can be clearly measured for different impacts with varying v_0. The bottom panel shows a plot of the speed of the compressed front versus the initial impact speed, v_0. As expected for a nonlinear force law, the wave speed is not constant but increases with increasing v_0.

The bottom panel shows the front velocity as a function of impact speed for many different trajectories with three different circular intruders, which appear to lie on a single curve. Thus, the intruder velocity appears to set the wave speed (as opposed to the kinetic energy, for example), which is consistent with the earlier discussion on scaling of propagation velocity. However, the fit line shown is a power law with exponent of 0.55, much stronger than the exponent of 1/5 which would be expected in a one-dimensional case.

8.2.3 Particle Flow Lags the Intruder Motion

The main result from the previous chapter was that, for impacts into the hardest particles, a "steady-state" flow field forms quickly, and, for the bulk of the trajectory, the particle flow field has an overall magnitude set by the instantaneous intruder velocity and is otherwise constant. Thus, the flux of particles out of the column beneath the intruder is always proportional to the rate at which area is being swept out by the intruder. Simply put, particles are getting out of the way as fast as the intruder is moving forward. This is made possible by the fact that M' is very small (i.e., less than 0.06) which allows the particles to respond quickly as the intruder is advancing. We can compare the area flux of the intruder, computed as its width times its velocity, with the area flux of particles leaving the column beneath the intruder, where the latter can easily be computed at each frame by using the coarse-grained velocity flow fields from the previous chapter. A comparison of the two area fluxes is shown in Fig. 8.7.

For the soft particles, this is not the case. Particles do not have time to respond, and they remain temporarily trapped beneath the intruder, as shown in Fig. 8.8. The top panel compares the area flux of the intruder with the area flux of the particles moving out from beneath the intruder. The area flux for the particles is more complicated, since we want to include the area vacated by particles as well as

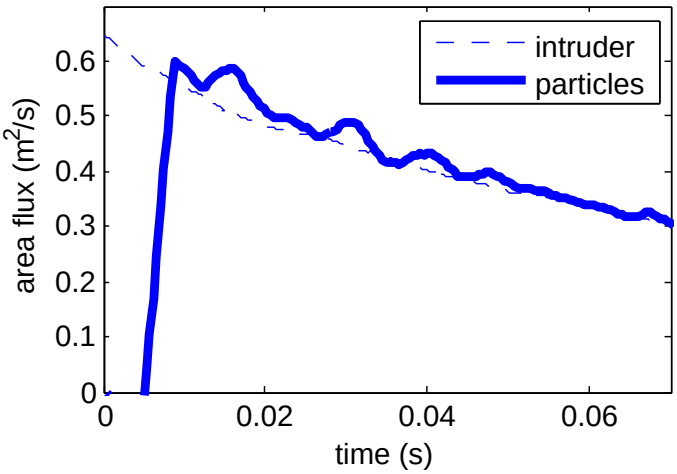

FIGURE 8.7: This figure shows a comparison of the area flux corresponding with the intruder motion and particle motion. The intruder area flux is simply the product of its width and velocity, while the particle area flux is the total particle area which is vacating the column beneath the intruder. These two quantities agree, which is consistent with the results of the previous chapter.

the typical area in the voids in the packing. Thus, the particle area flux is computed as the integral of the horizontal momentum flux divided by average mass density. The momentum flux is integrated over vertical lines which extend downward from the leftmost and rightmost points of the intruder, all the way to the bottom of the field of view. The momentum flux integral is normalized by the average mass density, which accounts for the fact that the particles do not completely fill the space; this allow the area flux of the intruder to be directly compared to the area flux for the particle flow.

The time integral of the difference between these two rates corresponds to an excess (or deficit) of particle density beneath the intruder, which is reflected in the coarse-grained packing fraction in a small region directly beneath the intruder, shown in the middle panel of Fig. 8.8. At first, the particle flux lags the intruder motion, characterized by an increased packing fraction and a very strong force exerted by the grains, F_g, as shown in the bottom panel of Fig. 8.8. However, as the elastic energy

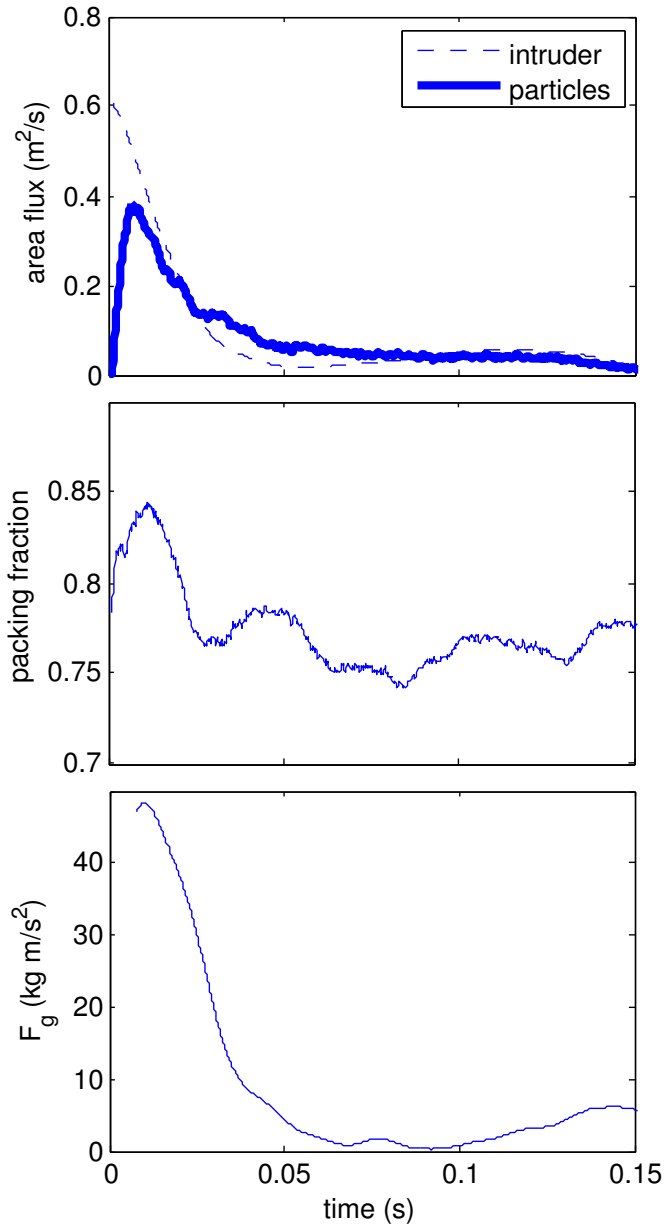

FIGURE 8.8: This figure shows that the particle motion differs from intruder motion for impacts into soft particles, which corresponds to an elastic-like response of the granular material. The top panel shows a comparison of the area flux, as in Fig. 8.7. Particle flow lags the intruder motion in early stages, leading to an increase in particle mass beneath the intruder, as shown in the middle panel. The bottom panel shows the force response of the granular material, measured from the trajectory of the intruder. This shows that the difference in particle and intruder motion corresponds to the force response by the material.

stored in the bed unloads, flinging particles upward, there is actually a deficit in the particle density beneath the intruder, and F_g essentially drops to zero as the granular medium breaks apart. This allows the intruder to sink down farther, as discussed previously. Note that the packing fraction directly beneath the intruder only barely reaches a packing fraction of 0.84, which is the point at which static 2D granular systems are isotropically jammed (O'Hern et al., 2003). Thus, isotropic jamming is not sufficient to explain the extremely strong forces exerted by the grains.

If we assume that the granular material is behaving like an elastic medium, and the time of the first local minimum in velocity scales like the time for the elastic medium to unload, we might expect this time to be proportional to the square-root of some effective mass (intruder plus some proportion of the particles) divided by some effective spring constant of the system. Figure 8.9 shows three trajectories each from three bronze circular intruders ($D = 6.35$ cm, $D = 12.7$ cm, and $D = 20.32$ cm) and one aluminum intruder ($D = 20.32$ cm, mass of approximately 75 g). If we rescale the time axis by $\sqrt{m + m_{eff}}$, where m_{eff} is 0.3 kg (corresponds to about 20% of the particles), we see that the local minimum in velocity seems to collapse. Therefore, the time scale for the particles to be lifted upward by the unloading elastic energy in the bed appears to be consistent with this idea.

8.3 Impacts into Moderately Stiff Particles

Thus far, we have examined what appear to be two limiting cases for granular impact, where $M' << 1$ and $M' \sim 1$. For impacts into the Shore 80A particles with an intermediate stiffness, we have access to a case where $M' \sim 0.1$. We will see that these particles show some of both the characteristics which we have used to characterize impacts into hard particles as well as the elastic-like response seen in soft particles.

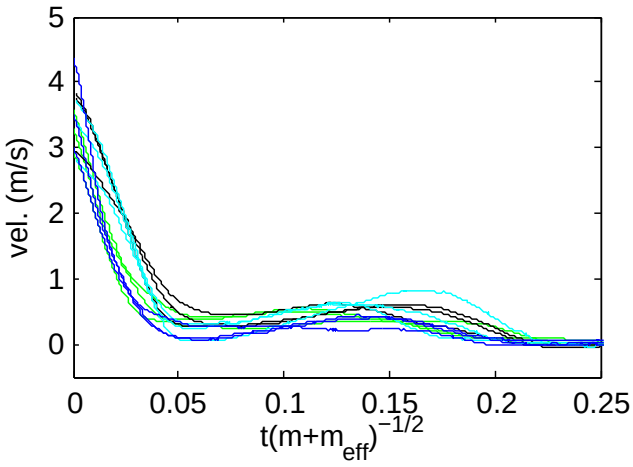

FIGURE 8.9: This plot shows three trajectories each from three bronze circular intruders ($D = 6.35$ cm, $D = 12.7$ cm, and $D = 20.32$ cm) and one aluminum intruder ($D = 20.32$ cm, mass of approximately 75 g), where the time axis is rescaled by $\sqrt{m + m_{eff}}$, where m_{eff} is 0.3 kg (corresponds to about 20% of the particles), we see that the local minimum in velocity seems to collapse. Therefore, the time scale for the particles to be lifted upward by the unloading elastic energy in the bed appears to be consistent with this idea.

8.3.1 Qualitative Behavior

Three sample trajectories for impacts into particles with intermediate stiffness are shown in Fig. 8.3. As in Fig. 8.3, these three impacts are for a circular intruder with a diameter of 12.7 cm, here with initial impact speeds of around 2.4, 3.5, and 5.2 m/s (these have $M' \approx 0.13$, 0.17, and 0.23, respectively). These trajectories are characterized by a sharp deceleration in the first 20 ms, then a relatively smooth deceleration as the intruder comes to a stop. Note that, as with the soft particles, the time scale of the sharp deceleration at the beginning of the trajectory is roughly constant for different intruder speeds. However, it is between one-third and half of the time scale for the initial deceleration in impacts into soft particles (Fig. 8.3, which is consistent with the fact that these particles are considerably stiffer.

As before, photoelastic images of these impacts give additional insight. Fig-

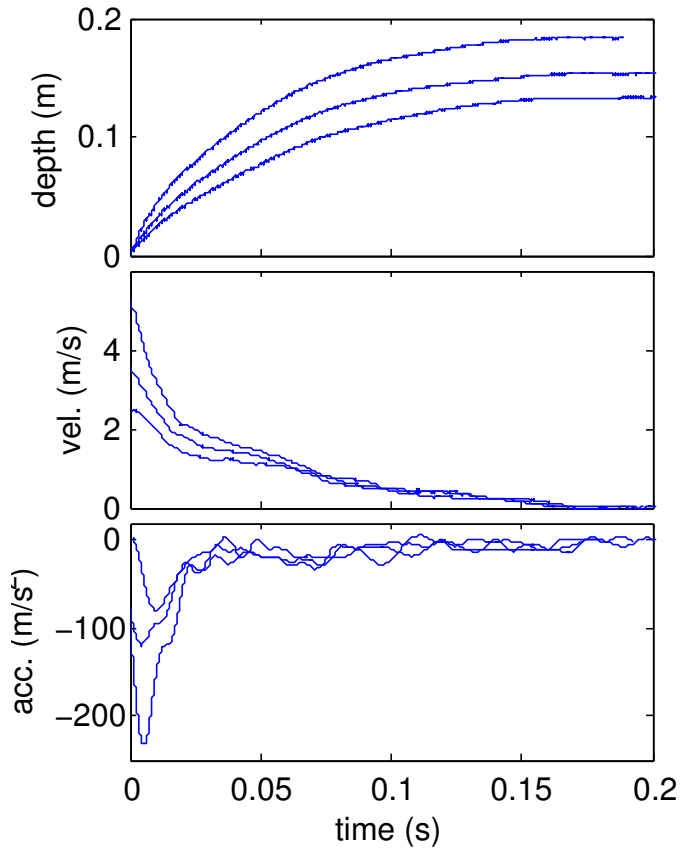

FIGURE 8.10: Plots of depth, velocity, and acceleration for three different impacts into particles with intermediate stiffness (Shore 80A) by the $D = 12.7$ cm disk.

ure 8.11 shows eight photoelastic frames which span the sharp deceleration at the beginning of the trajectories. When the intruder strikes, force response begins propagating downward, eventually connecting the intruder with particles at or very near the intruder boundary. This force propagation is similar to the shock-like fronts which propagate for soft particles: t_c is sufficiently large that the particles are unable to move fast enough.

There is a crucial qualitative difference between this and the shock-like fronts observed in the soft particles. For the intermediate-stiffness particles, particle rear-

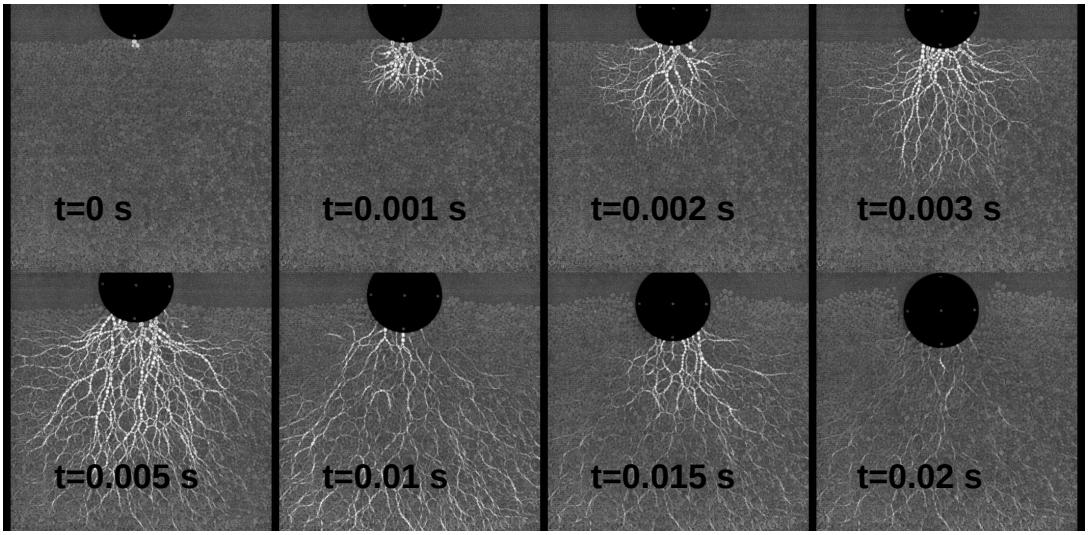

FIGURE 8.11: Sequence of frames depicting an impact into particles of intermediate stiffness (Shore 80A). These frames are for the fastest impact shown in Fig. 8.10 with the circular intruder with diameter $D = 12.7$ cm, and the times are labeled on each frame.

rangements are happening faster than in the soft particles, and these particle rearrangements allow the force network to rearrange and relax slightly, as shown in the top panel of Fig. 8.12. However, in contrast to the hard particles, these relaxations are sufficiently slow that the force network cannot completely relax. The force network grows until it reaches the bottom boundary of the experiment, but at a rate which is slower than the speed at which pulses tend to propagate (as opposed to the shock-like fronts in soft particles). This can be seen by examining space-time plots (bottom panel of Fig. 8.12, where there are clearly two distinct speeds: the speed at which pulses propagate (red lines), $c \approx 100$ m/s, and the speed at which the front grows (white line).

At about 15 ms, the force network begins to elastically unload (bottom panel of Fig. 8.12). This process is essentially finished by 20 or 25 ms after impact (Fig. 8.12), which leads to reduced force response throughout the bed (shown in the last frame of Fig. 8.11) and a slight plateau in the velocity profiles (shown in Fig. 8.10). After this,

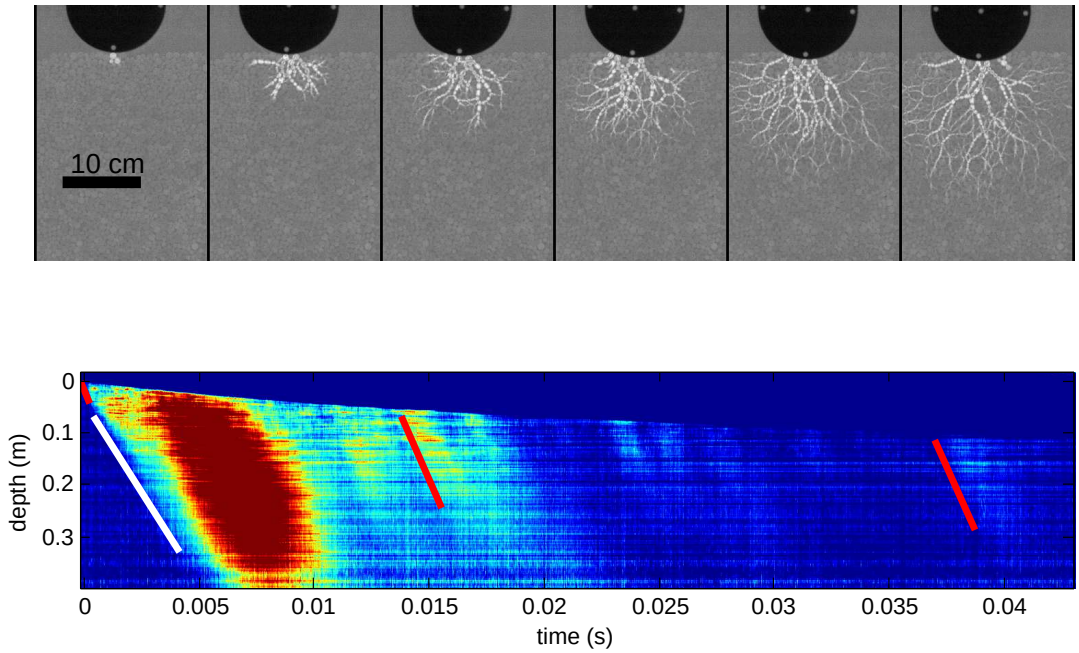

FIGURE 8.12: Top panel shows a sequence of frames depicting the early stages of an impact into particles of intermediate stiffness (Shore 80A). These frames are for the fastest impact shown in Fig. 8.10 with the circular intruder with diameter $D = 12.7$ cm (same trajectory as in Fig. 8.11). These frames are equally spaced over the first 2 ms, and are meant to show that the force network is rearranging as force signals propagate downward. Bottom panel shows a space-time plot of a column beneath the intruder. The red lines show a force-pulse speed of 100 m/s, and the white line shows the strong network during the initial stages growing at 70 m/s. This slower growth rate arises from competition between force propagation and particle rearrangements, which tend to relax the forces.

the photoelastic response during the remainder of the trajectory appears qualitatively similar to hard particle impacts. The forces are fluctuating in space and time.

8.3.2 Comparison to Macroscopic Force Law

With this in mind, one might ask how the trajectories in Fig. 8.10 fit to Eq. (1.8). Plotting the force versus velocity squared does yield approximately straight lines (Fig. 8.13), and so $f(z)$ and $h(z)$ can be measured and plotted. These are shown for one intruder (circular intruder with $D = 12.7$ cm) in Fig. 8.14. During the initial

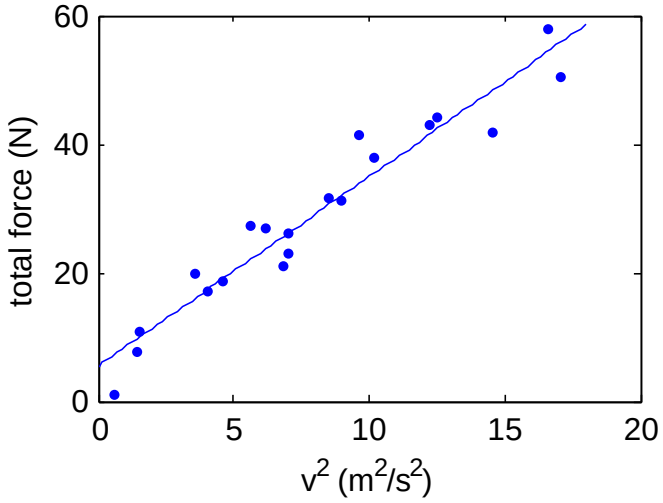

FIGURE 8.13: Plot of the net force on the intruder (circle, $D = 12.7$ cm) versus velocity-squared at a particular depth ($z \approx 2.5$ cm), where each data point represents a different trajectory. The scatter plot appears linear, suggesting that it is reasonable to fit to Eq. 1.8

stages, the intruder is essentially colliding with a growing cluster. This is reflected in a velocity-squared drag force which is also growing. At about $z \approx 0.06$ m, which is approximately the depth where the strong force network relaxes (0.02 seconds times 3 m/s, which is a typical intruder velocity). After this, $h(z)$ is relatively constant and $f(z)$ grows quasi-linearly.

Additionally, Fig. 8.15 shows similar fits to $f(z)$ and $h(z)$ for the triangular-nose intruders from Chapter 6, with $s = 0.5$, $s = 1.5$, and $s = 2.5$. As the aspect ratio is increase, the elastic-like effect becomes less dramatic and stretches over a longer depth, corresponding to the penetration of a longer nose. The overall magnitude of the $h(z)$ function seems to mirror the scaling of $I[C(x)]$, where blunt noses have a larger value, but the plateau region after the elastic-like response actually does the opposite: for blunt intruders, the value of $h(z)$ after the elastic-like effect is actually smaller than for more elongated noses. One potential explanation is that the blunt intruder creates a larger elastic response from the whole assembly, and the elastic

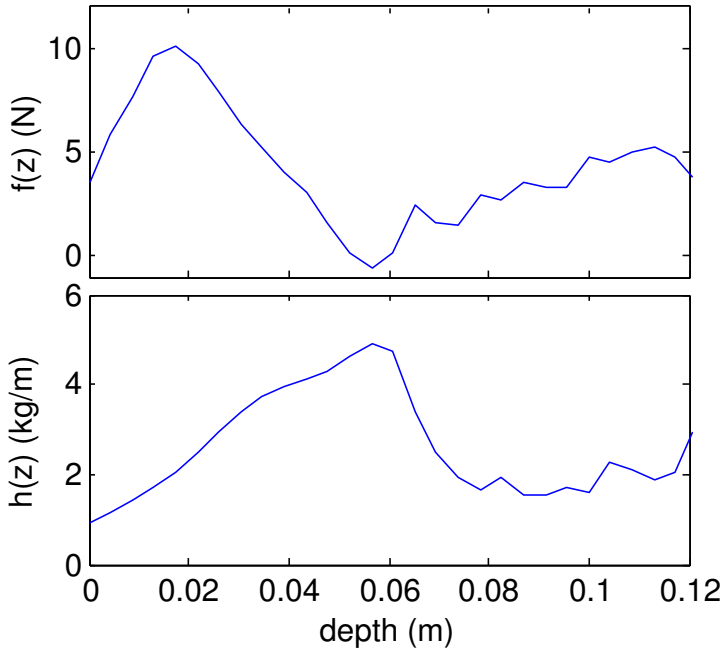

FIGURE 8.14: Plots of $f(z)$ and $h(z)$ for impacts into particles with intermediate stiffness (Shore 80A) by the $D = 12.7$ cm disk. Compared to the hardest particles (PSM-1), the transient behavior at the beginning is much larger and accounts for a far greater energy loss.

unloading leads to a sparser granular material and thus a lower drag coefficient. However, the simple macroscopic force law description has clearly begun to break down for these particles.

8.4 Conclusion

The focus of this chapter has been on the limits of when the macroscopic force law of Eq. (1.8) is valid to describe the dynamics of granular impact. Specifically, as the grain-grain collision time, t_c, begins to approach the intruder motion time, $t_d = d/v_0$, the granular response becomes more elastic-like and the force law begins to break down. Even when $M' = t_c/t_d \sim 0.1$, the flow field cannot reach an adiabatic equilib-

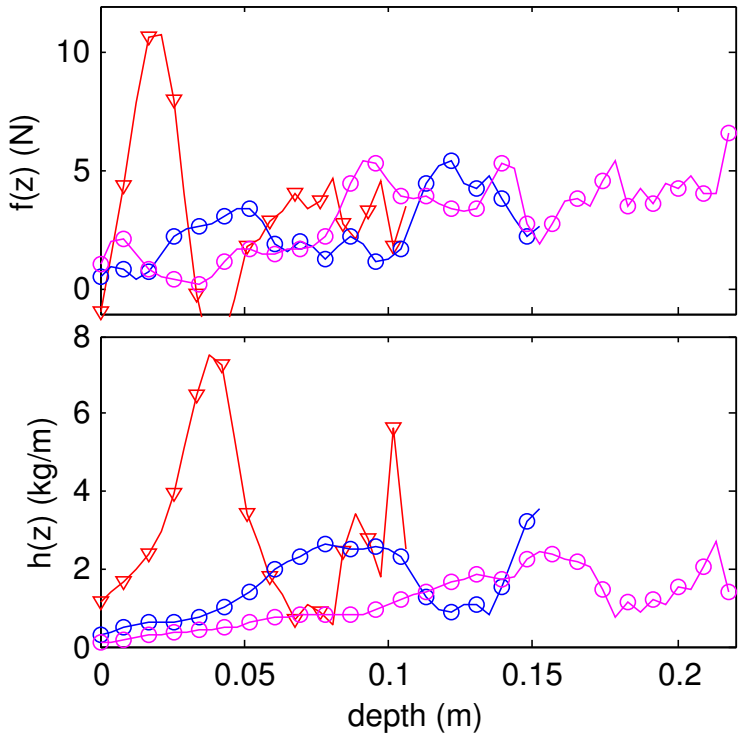

FIGURE 8.15: Plots of $f(z)$ and $h(z)$ for impacts into particles with intermediate stiffness (Shore 80A) by the triangular nosed intruders with $s = 0.5$ (red triangles), $s = 1.5$ (blue squares), and $s = 2.5$ (magenta triangles).

rium with the intruder motion, and the size of the effective cluster with which the intruder is colliding is no longer constant but increasing in time. As M' approaches unity, the force law is completely invalid, and the granular material is behaving like an elastic solid.

As a caveat, note that the way M' is increased in these experiments (keeping v_0 constant and changing the particle properties) is different from how it is typically increased in natural, industrial, or ballistics applications, where the intruder velocity is increased. While the basics of the granular response should be the same, the intruder would have significantly more energy to dissipate. In the present experiments, if the granular bed exhibits any kind of elastic-like response, this is sufficient to dissipate the majority of the intruder's energy. However, in the case where M' is increased

only be increasing the impact speed, one might expect that the intruder could have enough kinetic energy to pass continuously through the elastic-like regime into the regime where a velocity-squared force law would be valid. This is consistent with the findings of Allen et al. (1957), where the authors found that the trajectories of horizontal impacts into sand beds could be described with two different drag coefficients: one for high-speed at initial impact, and another after the intruder has slowed down.

9

Conclusions and Outlook

9.1 Summary of Results

In this thesis, I have presented a comprehensive study of the grain-scale dynamics in a series of two-dimensional granular impact experiments. By using photoelastic disks, we have access to the trajectory of the intruder as well as the dynamics of the granular material, both in the force response and the motion of the particles. Use of a sufficiently fast camera allows resolution of the smallest relevant space and time scales in the system. This yields microscopic data which has been previously inaccessible experimentally.

I have approached the problem of granular impact from the perspective of a family of macroscopic force laws which are dominated by a velocity-squared drag force. The particular form used in this thesis is given in Eq. (1.8), which is a generalization of force laws used in many studies on granular impact. The results from this thesis can be summarized as follows.

1) This force law, which has typically been used for impacts into three-dimensional granular systems composed of sand or glass beads, is also effective in describing

impacts into a two-dimensional system of photoelastic disks which are similar in stiffness and frictional properties to sand and glass beads. Thus, many of the microscopic insights gained in the two-dimensional system should also be applicable to impacts in three-dimensional systems.

2) Even though this macroscopic force law is effective at capturing the trajectories on average, the instantaneous force is highly fluctuating in space and time. Physically, these fluctuations correspond to rich, intermittent acoustic activity which occurs at the leading edge of the intruder as it moves. Thus, at the grain-scale, the intruder's energy is transferred to the granular material in a series of intermittent collisions which send the energy away in the form of acoustic pulses which are dissipated in the granular medium.

3) In light of this, the "smooth" force law in Eq. (1.8) must be modified to include a stochastic term, as in Eq. (4.1). We can use the photoelastic response beneath the intruder to estimate the statistics of the fluctuating force on the intruder as it moves. This fluctuating force has an overall magnitude that scales with the average force predicted by the macroscopic force law, but it is otherwise independent of the intruder dynamics. This suggests that the time-scale of the force fluctuations is set by the lifetime of the acoustic events, as opposed to particle rearrangements or breaking force chains. This is key to understanding the transition to elastic-like behavior for softer particles.

4) The terms in the force law, $f(z)$ and $h(z)$, can be calculated for various intruders, which we do in part by using a kinetic-energy reformulation of the force law, as developed in Chapter 5. This analysis shows that $f(z)$ scales up with intruder size and mass, but otherwise has no dependence on the shape of the intruder nose. However, $h(z)$ shows significant dependence on intruder shape,

even when holding mass and cross-sectional width constant. To understand this effect, we developed a collisional model which treated $h(z)$ as a series of random collisions with stationary clusters of grains. This model was extremely effective at capturing the drag coefficient over a wide range of intruder shapes, as well as capturing the dynamics of off-axis rotations. One of the most surprising results from this model is that friction between the grains and the intruder nose is of very little importance, as it was explicitly excluded from the model. This is consistent with photoelastic videos, where the forces emanate from the intruder at an angle which is very close to the local boundary normal.

5) By looking at the particle flow fields for impacts where the force law is valid, we see that the particle flow reaches a kind of adiabatic equilibrium with the intruder motion: the particle flow field near the intruder has a constant shape with an overall magnitude which scales with the intruder velocity. This is made possible by the fact that the acoustic pulses, which carry information about the intruder motion to the grains, travel very fast compared to the speed of the intruder. Thus, the particles are able to respond quickly to the intruder motion and rearrange accordingly. The forces from Chapters 3 through 7 are necessarily responsible for enacting these flow fields.

6) When the rate of force transmission becomes slower compared to the intruder speed, the force law picture breaks down. The particles do not transmit force and momentum fast enough and clear a path for the advancing intruder. Instead, they store energy elastically and the granular material begins to behave like an elastic solid.

9.2 Future Outlook

The ideas presented in this thesis can be extended or applied in several ways.

1) One obvious direction for future research would be to extend the collisional model of Chapter 6 to three-dimensions. Testing this would be straightforward and would require only intruder trajectory data, as opposed to the microscopic particle data which was crucial to much of the analysis in this experiment. If the drag-coefficient scaling and rotations matched the predictions of the collisional model, this would be strong confirmation that the microscopic picture is similar in three dimensions.

2) In the regime where the force law is applicable, the particles are in adiabatic equilibrium with the intruder. The particle flow field is constant in shape, with an overall magnitude which scales with the intruder velocity. Thus, if the intruder speed were to be held constant in this regime, one would expect that the particle flow would remain the same. This is essentially the spirit of the "well developed flows" for which $\mu(I)$ rheology is used. Thus, it would be interesting to test whether the flow field is consistent with the $\mu(I)$ description.

3) The breakdown of the macroscopic force laws for increasing M' happens in a way which should be applicable to other granular flows. Additionally, the force law begins to break down long before the intruder is actually moving at speeds which are similar to a typical acoustic speed. For example, the macroscopic force law description had already begun to break down in Shore 80A particles, where intruders were moving between 1 and 5 m/s and force pulses typical moved at approximately 100 m/s. Thus, continuum-like descriptions, such as the force-law picture for granular impact or rheologies for relatively slow flows, may be valid in a lab setting, but the real-world systems which the experiments are modeling could easily be outside the regime where the continuum description is valid, even with a relatively moderate difference in the properties of the two systems.

4) Finally, the elastic-like limit in granular impacts is strongly reminiscent of impact driven solidification in dense suspensions, as studied by Waitukaitis and Jaeger (2012) and many others. The idea of two competing time scales may be useful to describe this effect, although the relevant time for particle-particle momentum transfer is much less clear in the case of, for example, wet corn starch particles immersed in water.

Bibliography

Albert, I., Sample, J. G., Morss, A. J., Rajagopalan, S., Barabási, A.-L., and Schiffer, P. (2001), "Granular drag on a discrete object: Shape effects on jamming," *Phys. Rev. E*, 64, 061303.

Allen, W. A., Mayfield, E. B., and Morrison, H. L. (1957), "Dynamics of a Projectile Penetrating Sand," *Journal of Applied Physics*, 28.

Ambroso, M. A., Santore, C. R., Abate, A. R., and Durian, D. J. (2005), "Penetration depth for shallow impact cratering," *Phys. Rev. E*, 71, 051305.

Bagnold, R. A. (1954), "Experiments on a Gravity-Free Dispersion of Large Solid Spheres in a Newtonian Fluid under Shear," *Proceedings of the Royal Society of London. Series A. Mathematical and Physical Sciences*, 225, 49–63.

Ballard, D. (1981), "Generalizing the Hough transform to detect arbitrary shapes," *Pattern Recognition*, 13, 111 – 122.

Bi, D., Zhang, J., Chakraborty, B., and Behringer, R. P. (2011), "Jamming by shear," *Nature*, 480, 355–358.

Brzinski, T. A., Mayor, P., and Durian, D. J. (2013), "Depth-Dependent Resistance of Granular Media to Vertical Penetration," *Phys. Rev. Lett.*, 111, 168002.

Campbell, C. S. (2002), "Granular shear flows at the elastic limit," *Journal of Fluid Mechanics*, 465, 261–291.

Clark, A. H. and Behringer, R. P. (2013), "Granular impact model as an energy-depth relation," *EPL (Europhysics Letters)*, 101, 64001.

Clark, A. H., Mort, P., and Behringer, R. P. (2012a), "Coarse graining for an impeller-driven mixer system," *Granular Matter*, 14, 283–288.

Clark, A. H., Kondic, L., and Behringer, R. P. (2012b), "Particle Scale Dynamics in Granular Impact," *Phys. Rev. Lett.*, 109, 238302.

Clark, A. H., Kondic, L., and Behringer, R. P. (2013), "Granular impact dynamics: Fluctuations at short time-scales," *AIP Conference Proceedings*, 1542.

Clark, A. H., Petersen, A. J., and Behringer, R. P. (2014), "Collisional model for granular impact dynamics," *Phys. Rev. E*, 89, 012201.

da Cruz, F., Emam, S., Prochnow, M., Roux, J.-N., and Chevoir, F. m. c. (2005), "Rheophysics of dense granular materials: Discrete simulation of plane shear flows," *Phys. Rev. E*, 72, 021309.

Daniels, K. E., Coppock, J. E., and Behringer, R. P. (2004), "Dynamics of meteor impacts," *Chaos: An Interdisciplinary Journal of Nonlinear Science*, 14.

de Bruyn, J. R. and Walsh, A. M. (2004), "Penetration of spheres into loose granular media," *Canadian Journal of Physics*, 82, 439–446.

Forrestal, M. and Luk, V. (1992), "Penetration into soil targets," *International Journal of Impact Engineering*, 12, 427 – 444.

Geng, J. and Behringer, R. P. (2005), "Slow drag in two-dimensional granular media," *Phys. Rev. E*, 71, 011302.

Goldhirsch, I. (2010), "Stress, stress asymmetry and couple stress: from discrete particles to continuous fields," *Granular Matter*, 12, 239–252.

Goldhirsch, I. and Goldenberg, C. (2002), "On the microscopic foundations of elasticity," *The European Physical Journal E*, 9, 245–251.

Goldhirsch, I. and Zanetti, G. (1993), "Clustering instability in dissipative gases," *Phys. Rev. Lett.*, 70, 1619–1622.

Goldman, D. I. and Umbanhowar, P. (2008), "Scaling and dynamics of sphere and disk impact into granular media," *Phys. Rev. E*, 77, 021308.

Goldsmith, J., Guo, H., Hunt, S. N., Tao, M., and Koehler, S. (2013), "Drag on intruders in granular beds: A boundary layer approach," *Phys. Rev. E*, 88, 030201.

Gómez, L. R., Turner, A. M., van Hecke, M., and Vitelli, V. (2012), "Shocks near Jamming," *Phys. Rev. Lett.*, 108, 058001.

Grant, I. (1997), "Particle image velocimetry: A review," *Proceedings of the Institution of Mechanical Engineers, Part C: Journal of Mechanical Engineering Science*, 211, 55–76.

Greenhow, M. and Yanbao, L. (1987), "Added masses for circular cylinders near or penetrating fluid boundariesreview, extension and application to water-entry, -exit and slamming," *Ocean Engineering*, 14, 325 – 348.

Jaeger, H. M., Nagel, S. R., and Behringer, R. P. (1996), "Granular solids, liquids, and gases," *Rev. Mod. Phys.*, 68, 1259–1273.

Jop, P., Forterre, Y., and Pouliquen, O. (2006), "A constitutive law for dense granular flows," *Nature*, 441, 727 – 730.

Kamrin, K. and Koval, G. (2012), "Nonlocal Constitutive Relation for Steady Granular Flow," *Phys. Rev. Lett.*, 108, 178301.

Katsuragi, H. and Durian, D. J. (2007), "Unified force law for granular impact cratering," 3, 420 – 423.

Liu, A. J. and Nagel, S. R. (2010), "The Jamming Transition and the Marginally Jammed Solid," *Annual Review of Condensed Matter Physics*, 1, 347–369.

Liu, C.-h. and Nagel, S. R. (1992), "Sound in sand," *Phys. Rev. Lett.*, 68, 2301–2304.

Majmudar, T. S., B. R. P. (2005), "Contact force measurements and stress-induced anisotropy in granular materials," *Nature*, 435, 1079–1082.

Makse, H. A., Gland, N., Johnson, D. L., and Schwartz, L. (2004), "Granular packings: Nonlinear elasticity, sound propagation, and collective relaxation dynamics," *Phys. Rev. E*, 70, 061302.

Miloh, T. (1991), "On the initial-stage slamming of a rigid sphere in a vertical water entry," *Applied Ocean Research*, 13, 43 – 48.

Mouchacca, A., Langberg, D., and Nilmani, M. (1996), "Characterization of phenomena associated with impacting of spheres into glycerol solutions," *Powder Technology*, 88, 95 – 99, Research of Powder Technology in Australia.

Nelson, E. L., Katsuragi, H., Mayor, P., and Durian, D. J. (2008), "Projectile Interactions in Granular Impact Cratering," *Phys. Rev. Lett.*, 101, 068001.

Newhall, K. A. and Durian, D. J. (2003), "Projectile-shape dependence of impact craters in loose granular media," *Phys. Rev. E*, 68, 060301.

O'Hern, C. S., Silbert, L. E., Liu, A. J., and Nagel, S. R. (2003), "Jamming at zero temperature and zero applied stress: The epitome of disorder," *Phys. Rev. E*, 68, 011306.

Pacheco-Vázquez, F., Caballero-Robledo, G. A., Solano-Altamirano, J. M., Altshuler, E., Batista-Leyva, A. J., and Ruiz-Suárez, J. C. (2011), "Infinite Penetration of a Projectile into a Granular Medium," *Phys. Rev. Lett.*, 106, 218001.

Pica Ciamarra, M., Lara, A. H., Lee, A. T., Goldman, D. I., Vishik, I., and Swinney, H. L. (2004), "Dynamics of Drag and Force Distributions for Projectile Impact in a Granular Medium," *Phys. Rev. Lett.*, 92, 194301.

Qi, H. J., Joyce, K., and Boyce, M. C. (2003), "Durometer hardness and the stress-strain behavior of elastomeric materials," *Rubber Chemistry and Technology*, 76, 419.

Ren, J., Dijksman, J. A., and Behringer, R. P. (2013), "Reynolds Pressure and Relaxation in a Sheared Granular System," *Phys. Rev. Lett.*, 110, 018302.

Seguin, A., Bertho, Y., Gondret, P., and Crassous, J. (2009), "Sphere penetration by impact in a granular medium: A collisional process," *EPL (Europhysics Letters)*, 88, 44002.

Seguin, A., Bertho, Y., Martinez, F., Crassous, J., and Gondret, P. (2013), "Experimental velocity fields and forces for a cylinder penetrating into a granular medium," *Phys. Rev. E*, 87, 012201.

Takehara, Y., Fujimoto, S., and Okumura, K. (2010), "High-velocity drag friction in dense granular media," *EPL (Europhysics Letters)*, 92, 44003.

Truscott, T. T., Epps, B. P., and Belden, J. (2014), "Water Entry of Projectiles," *Annual Review of Fluid Mechanics*, 46, 355–378.

Tsimring, L. and Volfson, D. (2005), "Modeling of impact cratering in granular media," *Powders and grains*, 2, 1215–1223.

Umbanhowar, P. and Goldman, D. I. (2010), "Granular impact and the critical packing state," *Phys. Rev. E*, 82, 010301.

van Hecke, M. (2010), "Jamming of soft particles: geometry, mechanics, scaling and isostaticity," *Journal of Physics: Condensed Matter*, 22, 033101.

Waitukaitis, S. R. and Jaeger, H. M. (2012), "Impact-activated solidification of dense suspensions via dynamic jamming fronts," *Nature*, 487, 205–209.

Walsh, A. M., Holloway, K. E., Habdas, P., and de Bruyn, J. R. (2003), "Morphology and Scaling of Impact Craters in Granular Media," *Phys. Rev. Lett.*, 91, 104301.

Biography

Abram Henry Clark IV was born on September 3, 1984 in Arlington, Texas. He graduated from James Martin High School in 2002 and attended Texas Tech University. There, he earned a Bachelor of Science degree in Electrical Engineering, graduating in 2006 as the Highest Ranking Graduate of the Texas Tech College of Engineering. He went on to earn a Master of Science degree in Electrical Engineering from Texas Tech in 2008. In the fall of 2008, he began work on a Doctor of Philosophy degree from Duke University Department of Physics. Along the way, he earned a Master of Arts degree in Physics in May of 2011. This dissertation marks the completion of his doctoral degree, under his advisor, Robert Behringer.

During his time at Duke, Abe has been honored with the Charles Townes / Perkin Elmer Fellowship, awarded by the Duke Physics Department for outstanding graduate students, and the Fritz London Fellowship, awarded by the Duke Physics Department for excellence in condensed matter research. Additionally, he was recognized as an Outstanding Teaching Assistant by the American Association of Physics Teachers. He has four publications on the subject of granular impact (Clark et al., 2012b; Clark and Behringer, 2013; Clark et al., 2013, 2014) and one on the subject of a model of an industrial granular mixer (Clark et al., 2012a).

He is married to Kim and has a daughter named Charlotte who was born in August of 2013.